

A Strength Prediction of Wire and Arc Additive Manufactured joints

by

Pohsun Wu

to obtain the degree of Master of Science in Civil Engineering
at the Delft University of Technology,
to be defended publicly on March 18, 2021

Student number: 4883918
Project duration: May 01, 2020 - March 18, 2021
Thesis supervisor: Ir. L.P.L van der Linden
Thesis committee: Prof. dr. ir. J.G. Rots
Dr. ir. M.A.N. Hendriks
PhD. J.L. Galán Argumedo

Preface

I believe that future construction should be more innovative and focus on enhancing production efficiency, material circularity, and automation. The idea of 3D printing houses has always been considered a solution. It always seems like a pie in the sky until I met Lennert (my thesis supervisor).

Lennert introduced me to his world of steel 3D printing technologies and showed me one of his Wire and Arc Additive Manufacturing (WAAM) printed joint (a similar joint in the same project in Fig.2.12 at p.16). Seeing the printed joint and feeling it reminds me of my old passion and makes me decide to join and explore new horizons of the 3D printing world with him.

My research works out my doubt of “why can’t 3D printing be realized in our world and what hinders its universal applicability?” In short, the lack of experimental results and verification methods. Building codes we have now are based on numerous numerical calculations and tens of thousands of lab experiments to prove it safe. But the development of 3D printing for structures is rather “too fresh”. No codified code is provided for the design, and not enough research to prove it safe. Therefore, ideas and strategies made to form a reliable analysis method have led me to my research topic: A Strength Prediction of Wire and Arc Additive Manufactured joints.

The pie is still in the sky, perhaps I can’t reach it for now, but I believe that all people on the planet can share a bite in the near future.

Acknowledgements

Throughout this thesis writing, I want to express my gratitude to all committee members for the support and assistance. I am thankful for Professor Rots's willingness to be the chair of the committee. Professor Max's guidance on my FEA knowledge and kindness throughout the whole process. My thesis supervisor Lennert is always very helpful, responsive, and surprising to me with great ideas. And material science expert Jose, who gave me abundant knowledge of material behavior and analysis suggestions.

I would also like to thank all my friends for the accompanying and support, typically Newman, who I always can ask favor from when I encounter any technical issues.

Finally, I would like to give my greatest thanks to my family, who are very supportive emotionally and economically.

Contents

Preface	i
Acknowledgements	ii
Summary	v
1 Introduction	1
1.1 Background and motivation	1
1.2 Problem statement	2
1.3 Research objective and main research question	3
1.4 Thesis structure and research methodology	3
1.5 Scope and limitations	6
2 Background knowledge	7
2.1 Background knowledge of metallic additive manufacturing	7
2.1.1 Additive Manufacturing (AM)	7
2.1.2 Types of AM for steel	8
2.1.3 Comparison of WAAM and SLM/DMLS on printing metallic structural components	11
2.1.4 Introduction of Wire and Arc Additive Manufacturing (WAAM)	13
2.1.5 Experimental research of AM (SLS and WAAM) in Architectural and Structural engineering discipline.	16
2.2 Types of shell analysis defined in Eurocode 3	17
2.3 The structural principle of moment resistant joint on gridshell	20
2.3.1 Types of moment resistant joints in gridshell structures	21
2.3.2 Joint classification	24
2.3.3 The FEA and lab experiment review of gridshell joints	27
2.4 Conclusions	31
3 Reviews of four WAAM mechanical lab tests	34
3.1 General knowledge	34
3.1.1 Printing material - 308LSi	34
3.1.2 The Ramberg Osgood and Rasmussen approximation	35
3.1.3 Conversion of engineering stress-strain curve to true stress-strain curve	36
3.1.4 Imperfections of circular WAAM product	36
3.2 Tensile test	39
3.2.1 Tensile test setup	39
3.2.2 Tensile test result	41
3.3 Compression test	41
3.3.1 Compression test setup	41
3.3.2 Compression test result	42
3.4 Bending test	42
3.4.1 Bending test setup	42
3.4.2 Bending test result	44
3.5 Buckling test	44
3.5.1 Buckling test setup	44
3.5.2 Buckling test result	45

3.6	Conclusions	46
4	Numerical simulation of four WAAM mechanical tests	48
4.1	Simulation preparations	48
4.1.1	Finite Element Analysis software - ABAQUS	49
4.1.2	Factors and types of analysis considered for simulation and strength analysis	49
4.1.3	Material non-linear input - The true stress-strain curve	49
4.1.4	Introducing WAAM imperfections in numerical simulations	50
4.2	Simulation of Tensile test	52
4.2.1	Tensile test settings	52
4.2.2	Tensile test process	54
4.2.3	Tensile test results	55
4.2.4	Tensile test analysis	57
4.2.5	Tensile test conclusions	57
4.3	Simulation of Compression test	58
4.3.1	Compression test settings	59
4.3.2	Compression test process	60
4.3.3	Compression test results	62
4.3.4	Compression test analysis	65
4.3.5	Compression test conclusions	66
4.4	Simulation of Bending test	68
4.4.1	Bending test settings	68
4.4.2	Bending test process	70
4.4.3	Bending test results	71
4.4.4	Bending test analysis	73
4.4.5	Bending test conclusions	73
4.5	Simulation of Buckling test	74
4.5.1	Buckling test settings	75
4.5.2	Buckling test process	77
4.5.3	Buckling test results	80
4.5.4	Buckling test analysis	82
4.5.5	Buckling test conclusions	85
4.6	Conclusions	86
5	Strength prediction of proposed WAAM joints	88
5.1	Joint design	88
5.2	Joint strength prediction	91
5.2.1	Analysis idea and setting list	91
5.2.2	Settings	92
5.2.3	The setup for acquiring moment rotation curve	94
5.2.4	Result and strength prediction	95
5.3	Conclusions	100
6	Conclusions and recommendations	102
6.1	Answer to the research question	102
6.2	Conclusions	102
6.2.1	Reliability of the simulation - Interpretations of lab test simulation results	102
6.2.2	Strength prediction of joints	104
6.3	Recommendations	104
6.4	Future outline and research	105
A	Appendices	110
A.1	Material properties of INERTFIL 308LSi.	111
A.2	Tensile test results in transverse printed direction.	112
A.3	Tensile test results in longitudinal printed direction.	113

Summary

Anticipating the benefits and potential of using Wire and Arc Additive Manufacturing (WAAM) in the construction field for structural connections to enhance automation, energy efficiency, and material utilization rate, the process to provide a reliable and efficient prediction for the strength of WAAM components is the focus of this thesis.

Finite Element Analysis (FEA) is proven reliable and can be used as a method for strength prediction. ABAQUS has been chosen as a simulation tool due to its automatic and adaptive ability for computation and the dominance in academic research. Current WAAM components research builds WAAM models with the heat source and printing path, which took an unacceptable time (could be several days) to simulate the behavior (distortion and residual stress) for meter-scale structural WAAM steel components. A semi-analytical model, which implicitly incorporated the behavior of the WAAM material by the direct use of components' mechanical test data as the FEA inputs, can speed up the strength prediction process.

This research is built with a feasible process with unique steps for predicting WAAM components' strength. First, WAAM components' lab tests from Van Bolderen [1] have been reviewed and numerically examined before being used for designing WAAM joints, which makes the data used more reliable. Four lab tests that have been reviewed and simulated are the tensile test, the compression test, the bending test, and the buckling test. Examined material non-linearity, anisotropy of the material, and the surface roughness have been applied to predict the strength of the joints. Five aims and five actions have been set and implemented in the design of WAAM printed gridshell joints. Moment-rotational curves for three joints are presented to acquire flexural stiffnesses and moment capacities. Second, the inclusion of the defined geometrical imperfections (the surface roughness and the lack of straightness) and material imperfections (anisotropy) to get better simulation results to yield closer results to lab experiments. The surface roughness is derived from the bending test, the lack of straightness is incorporated with the failure mode found from Linear Buckling Analysis (LBA), and the anisotropy is evaluated by building orthotropic material with the young's modulus from two WAAM printing directions (transverse and longitudinal) in the elastic range. Last, the codified guidance for WAAM printed components, which are defined as shell structures in EN 1993-1-6: Eurocode 3: Design of steel structures - Part 1-6: Strength and stability of shell structures, have been implemented.

From the numerical simulation of four lab experiments, the tensile test simulation results show only maximum 0.5% errors (while compared yield strength, ultimate strength, and young's modulus to the lab result). Therefore, the material non-linearity from the lab test has been correctly used in the numerical simulation. The compression test results indicate the material non-linearity used in the three-dimensional objects is valid since the compression stress-strain curve fits the tensile engineering stress-strain curve well before the yield point (0.41% of errors with the comparisons of yield strength and young's modulus). The bending test can not precisely infer the errors of derived effective thickness mainly due to the lack of friction coefficient. However, the inclusion of the effective thickness reduces the error from 22.0% to 16.8%, and limited to 16.8% when compared to the lab test results, despite the fact that the value is from assumptions. The buckling test shows large buckling load errors (35%) that might due to the hand measured lack of straightness is too less, the effective thickness derived are too thick, or the defined geometrical imperfections are too simple that can't reflect the real printed conditions, which has local geometrical imperfections and deviations. The high sensitivity of the geometrical imperfections to the buckling load has also been found out from the analysis of scale factors with buckling loads. Few fraction increase of lack of straightness (0.2% to 0.4%) leads to tens of percentage error drop (19.6%) of buckling load compared to the lab results.

Examined data that have been used in the analysis of joints are material non-linearity, the anisotropy

of the material (build-in orthotropic manners), and the surface roughness. The target values of the flexural stiffness and moment capacity are insensitive to the lack of straightness due to the fact that the instability of the joint does not come from the buckling effect, the WAAM printed parts are not in slender shape, and the lack of straightness is small ($L/791$).

Three WAAM printed joints have been designed, and the strength prediction have been carried out with the joint classification.

At the end of this thesis, the conclusion is that there is potential to provide reliable strength prediction of the designed WAAM joints with the use of EN 1993-1-6: Eurocode 3 as guidance for building semi-analytical models for WAAM components and joints with the lab test material data and defined imperfections for two reasons.

First, the simulation results yield closer values to the lab test results with the shell analysis process in EC3. In the compression test simulation, the inclusion of the possible geometrical imperfections shape found from LBA reduces the percentage errors decrease from 52.27% to 13.75%. In the bending test simulation, the inclusion of effective thickness leads to a closer value to the lab test (from 22% to around 16.8%). In the buckling test simulation, the implementation of effective thickness for surface roughness reduces around 10% to 15% error, and the inclusion of effective thickness combined with lack of straightness reduces roughly 40% of the error.

Second, the parameters are examined before being used in the strength analysis of designed WAAM joints. The material non-linearity data is proven valid in the FEA with 3D geometry in tensile test and compression test simulations. The orthotropic behavior shows a minor effect in all four numerical simulations. The surface roughness combined with the use of assumed friction coefficient and the assumed equipment properties in the bending test simulation show limited error (around 17%).

However, limited errors exist and undermine the strength prediction precision due to the assumptions of lacked lab test measurements and the simplification (parameterized) imperfections from WAAM components. Therefore, It is expected that more tests and works could be made to improve the strength prediction precision of WAAM components. Also, the FEA setup of the designed joints is referred to as the gridshell joints' lab experiments, therefore, providing a methodology for possible future examination of the strength of WAAM printing joints with lab experiments.

Chapter 1

Introduction

1.1 Background and motivation

The growth of the world population increases energy consumption, and at the same time, produces a larger carbon footprint. The Paris Agreement commitment and the United Nations (UN) Sustainable Developments Goals (SDGs) 12 [2], both indicate that we are now over extracting natural resources. Urgent actions to improve resource efficiency, reduce waste, and mainstream sustainability practices are needed. Buildings and construction sector is now accounted for around 36% of final energy consumption [3], and 11% of global greenhouse emission [4].

Apart from the environmental issue, more complex structural designs were carried out along with the development of advanced computational tools. For instance, parametric optimized grid shell canopy structures equipped with various multi-degree connections are coming into reality. A structural project example of Westend Gate Tower canopy (Fig.1.1, Left) in Frankfurt shows complex grid shell and column geometry after the structural optimization [5]. The demand for these highly irregular structural parts increases the difficulties of production.

Moreover, the conventional way of producing these steel components is environmentally harmful and laborious (Fig.1.1, Right). The lack of skilled construction workers in the EU and around the world [6] [7] [8] may make the use of steel for complex structural design even worse.



Figure 1.1: The Westend Gate Tower canopy [5]. Left: Structure overview. Right: The assembly and welding of grid shell canopy compartments.

3D printing has always been considered the next-generation technology for production [9]. A more advanced design and producing complex building components by implementing state-of-the-art 3D printing, the Wire and Arc Additive Manufacturing (WAAM), becomes one of the best solutions to these critical issues.

The early development of 3D printing steel is the powder-based 3D printing method, which heats the powder to become metal and layers them to form steel parts in a limited size machine, is now widely used in mechanical and aerospace engineering. However, this technique is not suitable for large building components due to the relatively high cost and limited printing scale [10].

The later emerging of cutting-edge 3D printing technology makes components produced by 3D printing becomes possible. Wire and Arc Additive Manufacturing (WAAM) is a process that builds 3D objects with metal wires as feedstock and heated up by electric arc. This technology can print components up to a meter scale with its robotic arm at a relatively low cost [11]. In general, WAAM addresses the aspects of energy and material efficiency, circularity, and automation.

In energy and material efficiency aspects, WAAM can print large complex steel components with barely any material waste. Conventionally, lots of steel waste, which needs to be remelted, were produced when specific shapes were cut out from the steel plate. Therefore, for some complex structural parts, the use of WAAM can reduce energy usage and the carbon footprint [12].

The circularity can be done if the whole structure is designed with the idea of BAMB (Building As Material Banks) [13] [14]. Take the Westend Gate Tower canopy case as an example. If all joints are printed and made detachable, the remaining straight components, which are considered the "asset" in the material bank, can then be reused. This concept can positively improve the circularity of the building material.

The automation of the WAAM process enables it to print structure automatically in a free-form shape and at the same time limit laborious work, such as cutting, machining, and welding steel parts [15].

In sum, the implementation of WAAM on printing complex building joints seems to be the most suitable and promising technology. However, the lack of lab test data and verification impedes the application. Therefore, a research for designing and predicting a WAAM printed joint through the study of lab test data is provided in this thesis.

1.2 Problem statement

Nowadays, the verification of these cutting-edge large-scale WAAM components relies mainly on lab testing. Unluckily, the lab testing for large-scale 3D printed objects is confined due to the fund limitation. The use of Finite Element Analysis (FEA) for strength verification of a WAAM printed model becomes an option.

FEA, which uses the numerical mathematic technique for simulation, is proven reliable in analyzing objects with complex geometry. Much research of WAAM specimens was conducted using sequentially coupled transient thermal-mechanical models, which consider the influence of molten pool and moving heat source, to find the relation between printed specimens and their stress distortion, mechanical properties, and corrosion [16].

Although this research can get reliable results, the computational time is quite long due to the material's transient and non-linearity. The consequence is that the targeted specimen usually is being analyzed on a tiny scale (component length shorter than half a meter) [17].

Improvements of the thermal-mechanical analysis efficiency were being made but still being unfeasible for analyzing building scale components. For the improvements regarding the thermal field task, one method is to use a 2D transient model to analyze the thermal field [18]. Another method is transforming the 3D transient model to a steady-state model, which builds the geometry at first with finite element mesh, then letting the material fill up the path according to the printing direction. Montevecchi et al. [16] improved the heat source model proposed by Goldak et al. [19] with the steady-state model and saves 99% of computational time. For mechanical analysis improvement, Ding et al. [17] simplified the mechanical model by applying peak temperature to the assigned effective plastic area and reduced 98% of computational time. The total computing time combining thermal and mechanical analysis of

a four-layer wall of WAAM GMAW-CMT (Gas metal arc welding with the cold metal transfer process) takes about 75hours. Each layer has 500mm length x 5mm width x 2mm (thickness).

In one of the latest research of thermal-mechanical analysis, Ahmad and et. compared the computation time between two different heat source models (Goldak's double-ellipsoid and rectangular) in GMAW (Gas metal arc welding) process [20]. The result shows the simple five layers printed wall, which has dimensions of 150mm (length) x 22.5mm (width) (three welds going back and forth) x 7.5mm (thickness), takes about 34.9 hours for the rectangular model, and 35.8 hours for Goldak's model to compute the distortions and residual stresses. The rectangular model's application is slightly better in computational time but is definitely not practical in analyzing structural component models normally at a meter scale level and usually have more complex shapes. Therefore, instead of analyzing the strength of WAAM components with the heat model, a different research method using a semi-analytical method, which implicitly incorporated the behavior of the WAAM material (distortions and residual stress) from the use of components' mechanical test studies and used it as the FEA inputs, is considered in the research.

Conventionally, with acceptable computational time, there are many experiences in using material data from mechanical lab tests as the input for analyzing conventional steel structures. Imperial College London takes the same idea to perform an initial verification of a WAAMed bridge printed by MX3D. The verification uses the material data from lab tests for computational analysis. Tensile coupon tests provide the data in material scale, compression tests offer the data in cross-sectional level, and full-scale bridge testing analyzes the structural level problem [21].

Nonetheless, the insufficient test data and validated procedure undermine the credibility of computation-based verification [22]. In order to enhance the simulation reliability and efficiency for larger WAAM components, a feasible process with unique steps has been covered in this research. First, the WAAM components' lab test data has been numerical examined before being used in the strength prediction of designed WAAM joints. Second, defined geometrical imperfections (the surface roughness and the lack of straightness) and the material imperfection (anisotropy) have been incorporated in numerical models to get better simulation results closer to lab results. Last, the use of the Eurocode 3 guidance for WAAM printed components, which are defined as shell structures in EN 1993-1-6: Eurocode 3: Design of steel structures - Part 1-6: Strength and stability of shell structures [23].

1.3 Research objective and main research question

The objective of the current study is to provide a reliable and efficient computational method to predict the strength of WAAM's printed joints with the use of lab test mechanical data.

So the main question is:

How can the strength analysis of designed WAAM joints be carried out using WAAM components' lab test data to provide a reliable strength prediction?

Sub-questions in each corresponding chapter are made (see Section 1.4) to fully cover the scope of this main question.

1.4 Thesis structure and research methodology

This thesis binds relative potential knowledge to manifest the prediction of WAAM joint strength. Fig.1.2 shows the report structure and methodologies. The context in the following section clearly illustrates the purpose of each chapter and the relations between them to show the steps for performing numerical analysis of the WAAM's lab experiments and conducting the analysis of proposed joints.

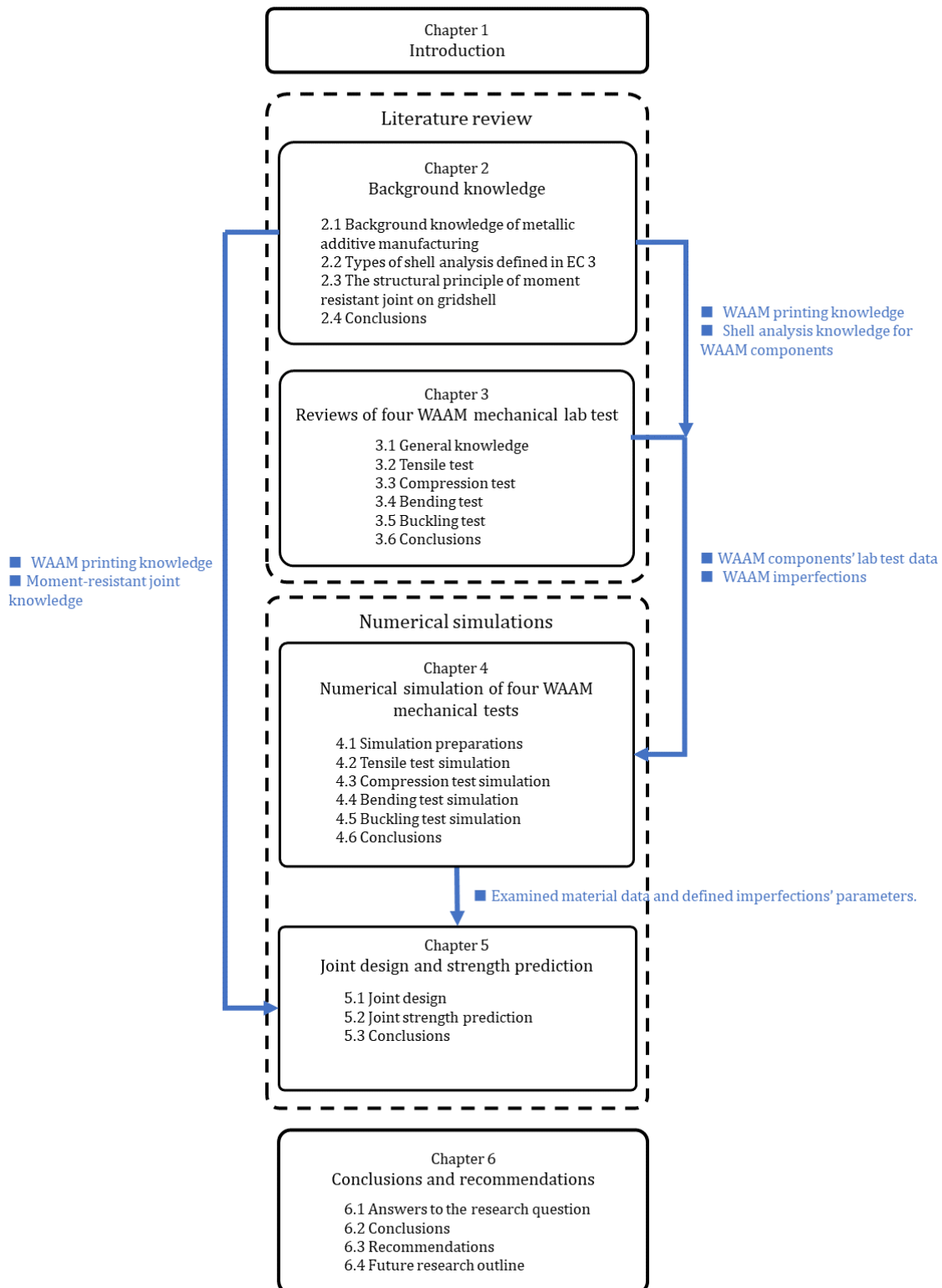


Figure 1.2: The overview of the thesis structure.

Chapter 2 - Background knowledge

The purpose of this chapter is to provide sufficient information for understanding Wire and Arc Additive Manufacturing (WAAM) as well as reviewing the method to design and analyze printed joints. The answers of the following questions will be provided.

- 1) What is the Wire and Arc Additive Manufacturing (WAAM), and what are its advantages compared to the powder-based method for producing large steel components?
- 2) What is the guidance in Eurocode 3 on analyzing the strength of WAAM printed components?
- 3) What are the design requirements of the moment-resistant gridshell joints.
- 4) How to estimate and classified the strength of a gridshell joint?

Chapter 3 - Reviews of four WAAM mechanical tests

This chapter provides a review study of WAAM mechanical lab tests specifically for continuous WAAM components from Van Bolderen's research [1]. This chapter's main purpose is to acquire material properties from each mechanical test for numerical simulation in Chapter 4. General knowledge for all the tests will be provided in Section. 3.1, and the following sections are four mechanical tests, the tensile test in Section. 3.2, the compression test in Section. 3.3, the bending test in Section. 3.4, and the buckling test in Section. 3.5.

Research questions in this chapter are:

- 1) What are the imperfections of WAAM components in the review of lab tests?
- 2) What is the setup for each mechanical test?
- 3) What lab test results are presented in each of the mechanical tests and are being used in numerical simulations in Ch4?

Chapter 4 - Numerical simulation of WAAM lab tests

This chapter uses numerical analysis (FEA) to simulate circular hollow WAAMed tubes from the lab test. This chapter's main goal is to examine the use of material data (material non-linearity) and the introduced imperfections of WAAMed hollow circular components to the FEA model with the use of the shell analysis method in EC3. The simulation results are discussed and compared with the lab test result to check the simulation's precision and validity.

Section.4.1 provides the knowledge and the data transformed from literature reviews to ideas and assumptions for numerical analyses. The following sections consist of lab test simulations, the tensile test simulations in Section.4.2, the compression test simulations in Section.4.3, the bending test simulations in Section.4.4, and the buckling test simulations in Section.4.5. The conclusions of the lab components' lab test simulation are in Section.4.6.

The examined data in this chapter can be further used for predicting the designed joint in Ch.5.

Research questions in this chapter are:

- 1) Do simulation results show the numerical simulation reliable?
- 2) How can the precision of simulations be improved? What parameters are lacking for performing the simulations?
- 3) What imperfections are included? And how can the imperfections be used to design the joint further and predict its strength?

Chapter 5 - Joint design and strength prediction

This chapter aims to use the advantage of WAAM to design joints for grid shell structures and provide its strength prediction regarding the joint stiffness and the moment capacity. The examined material data and defined imperfections from the components' lab test simulations (in Ch4) are used. Also, the design and the joint setup are planned in a way that the examination of the joint's strength reasonable and straightforward for future lab experiments (future work).

The following questions will be answered.

- 1) How do simulations of four lab experiments help with the strength prediction of the joint?
- 2) How does the designed joint performs in regards to the stiffness and the moment capacity?
- 3) How can the joint be improved?

Chapter 6 - Conclusions and recommendations

In final chapter, the results from all other chapters will be gathered to answer the research questions. Furthermore, conclusions, recommendations, and future research outline will be provided.

1.5 Scope and limitations

The strength prediction of the designed WAAM printed joint through the WAAM components' lab test data is a broad and complex topic. Lab test results must be reviewed first and then examined in numerical simulation before being applied to the designed joint. Therefore, some limitations were made to make the topic feasible.

- Only one type of material (308LSi) printed with the MX3D WAAM (GMAW) is considered.
- The research studies purely on elasto-plastic material behavior without the inclusion of creep or fracture.
- Several geometrical imperfections from WAAM printed components are observed in the analysis. However, only the surface roughness and lack of straightness are considered.
- Material imperfections from residual stress are not considered. Also, the distinction of inherit material heterogenities within each welding beam are excluded.
- The material's anisotropy is considered orthotropic in the numerical simualtions. The orthotropic behavior in this research is built from the young's modulus in two printed directions in the elastic scope and analyzed as shell elements.
- The designed joint is not printed out to perform lab tests due to the thesis scope limit. However, the joint strength prediction setup was designed referring to the lab tests.

Chapter 2

Background knowledge

This chapter is composed of three main parts. Section 2.1 shows the state of the art of additive manufacturing, typically with WAAM technologies. Section 2.2 presents the numerical analysis guidance from EN 1993-1-6: Eurocode 3: Design of steel structures - Part 1-6: Strength and stability of shell structures for analyzing WAAM components with shell elements. Section 2.3 discusses the requirements for designing moment-resistant gridshell joints. Section 2.4 answers the research questions in this section.

Research questions in this chapter are:

- 1) What is the Wire and Arc Additive Manufacturing (WAAM), and what are its advantages compared to the powder-based method for producing large steel components?
- 2) What is the guidance in Eurocode 3 on analyzing the strength of WAAM printed components?
- 3) What are the design requirements of the moment-resistant gridshell joints.
- 4) How to estimate and classified the strength of a gridshell joint?

2.1 Background knowledge of metallic additive manufacturing

This section starts with a general introduction of metallic additive manufacturing and introduces WAAM and its research applications to the reader.

2.1.1 Additive Manufacturing (AM)

Additive Manufacturing (AM), known as 3D printing, is a collective term for different technologies that produce objects by layering up successive material. By the use of this production process, the geometry of the printed object can be easily formed. A large variety of materials could be used in AM, such as polymers, plastics, ceramics, concrete, and the material considered in this research: steel.

The rising of AM in steel production

The idea of the AM was first patented by Baker in the year 1920 [24], who used electric arc to heat up metal and manually creating 3D object by depositing molten metal (Fig.2.1).

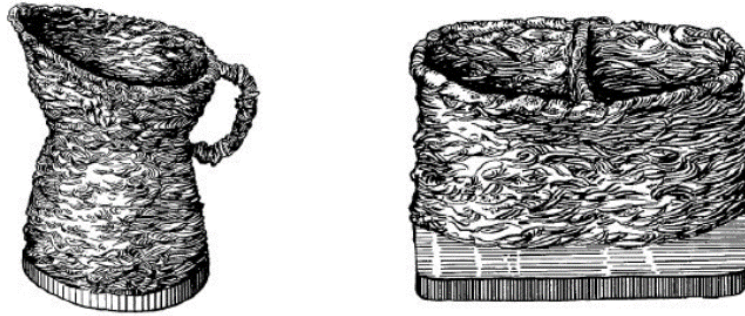


Figure 2.1: 3D metallic printed concept patented by Baker [24][Adapted].

In 1990, AM got more attention in manufacturing industries to reduce aerospace and automotive parts' cost. Rolls-Royce saw the potential of replacing traditional subtractive manufacturing with AM and developed the Shape metal deposition (SMD) technologies, which is similar to the current process of AM. Melted material are deposited layer by layer on a predefined path to form the object [25]. The benefit of AM is that it can produce customized parts with complex geometries that meet the demand of near-net-shape (NNS) fabrication, which requires fewer steps (time-saving; avoids cutting and welding processes that used to cut and joint the compartment together [26]) for producing products and consumes less raw materials (lightweight) [27].

2.1.2 Types of AM for steel

According to AM metal classifications for steel fabrication [28] and Standard Terminology for Additive Manufacturing Technologies in ASTM F2792 [29], AM technologies for metal are mainly classified into four categories, which are Powder-based fusion (PBF), Directed energy disposition (DED), Binder jetting, and Sheet lamination (see Table.2.1). Although each process varied in its classification group, the common concepts are similar.

Table 2.1: AM classification in steel production [28].

Categories	Technologies	Material	Power Source
Powder bed fusion (PBF)	Selective laser sintering (SLS) Direct metal laser sintering (DMLS) Selective laser melting (SLM) Electron beam melting (EBM)	Metal powder	Laser beam, Electron beam
Directed energy deposition (DED)	Electron beam freeform fabrication (EBF) Laser engineered net shaping (LENS) Laser consolidation (LC) Directed light fabrication (DLF) Wire and Arc Additive Manufacturing (WAAM)	Metal powder, Metal wire	Laser beam, Electric arc
Binder jetting	Powder bed and inkjet 3D printing (3DP)	Metal powder	Thermal energy
Sheet lamination	Laminated object manufacturing (LOM) Ultrasonic consolidation (UC)	Metal laminate, Metal foil	Laser beam

Two main AM categories, Powder Bed Fusion (PBF) and Directed Energy Deposition (DED), and each of their primary technologies, Selective laser sintering (SLS) and Wire and Arc Additive Manufacturing (WAAM), that are potentially suitable for printing steel structural components will be briefly introduced here.

Powder Bed fusion (PBF)

All Powder bed fusion (PBF) process have a similar set of functional parts:

- One or more thermal source to fuse powder particles.
- Powder adding and smoothing tools.
- Layer height controlling system for a constrained area, where the object is printed (powder bed).

Selective laser sintering (SLS) was developed the earliest in the PBF process. All other methods are the modification method for printing other materials or avoiding patented features [30]. The basic schematic of the SLS machine is shown in Fig.2.2. The laser heats up the powder in the powder bed layer by layer according to the desired shape. The build platform moves downward after a layer has been printed to make room for a new layer to form. The powder leveling roller evens up the powder supply from the feed cartridges while it moves up.

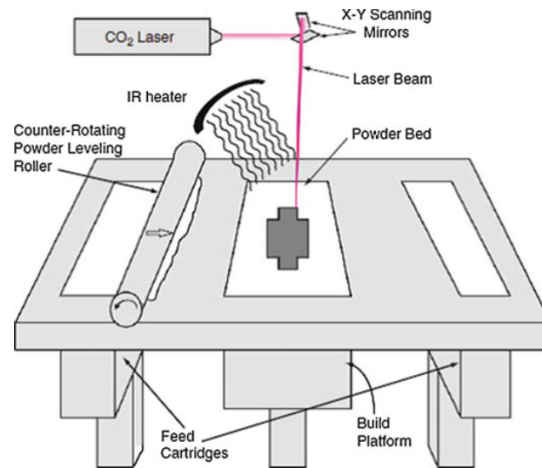


Figure 2.2: Schematic of the SLS process [30].

The most common heat source for PBF is lasers. Electronic beam and other thermal sources can also be used as the heat source but require different machine configuration.

Common powder bed fusion systems for metallic material are direct metal laser sintering (DMLS) and selective laser melting (SLM). The difference is that the DMLS builds the metallic part layer by layer by only sintering the metal powder's surface; particles are fused but not entirely melted. While SLM heats up the metal particles above the melting point by the use of a high-powered laser. Due to the larger heat inputs, SLM's printed objects are extraordinarily dense and robust; however, more considerable stresses and dislocations could compromise the product's strength.

Any metal suitable for welding is considered a good fit as PBF material, such as stainless steels, titanium, and alloys, nickel-based alloys, aluminum alloys, etc... Most powder bed process allows only one type of material printed at a time, as opposed to DED process. The main advantages of the PBF process are its high precision while producing parts and no printed supports needed during the production.

Until recently, metal powder bed fusion systems is still being expensive and complex, limiting their use to small quantities of high value or custom parts, such as aerospace components or medical devices.

Directed energy deposition (DED)

Directed energy deposition (DED) creates objects by depositing melted material at the defined path. The energy (heat source) is being directed into a narrow and focused location, where the material and substrate are been melted. Two types of material supply, metal powder and metal wire, are both the subcategories in the DED process. WAAM uses metal wire as the material and arc as the heat source.

- **Powder-feed (or Powder blown) process**

The DED processes that use metal powder as the supplied material are categorized as Powder-feed or powder-blown process. The schematic concept can be seen in Fig.2.3. Heat source (laser) were directed to the molten pool, where the small area of substrate were heated up and the metal powder is added or be "blown" to. Since the process all includes deposition, melting, and solidification of powder material, the printed objects has a high density and shares a similar microstructure as the one in PBF process.

Some DED powder-based technologies are, Laser engineered net shaping (LENS), Directed light fabrication (DLF), and Laser consolidation (LC).

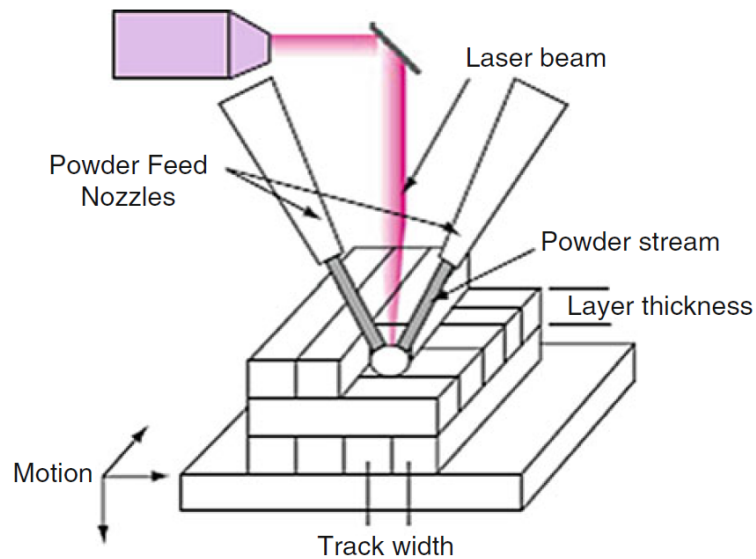


Figure 2.3: Schematic of the DED powder-feed process [31].

- **Wire-feed process**

The DED processes that use metal wire as the supplied material are categorized as the Wire-feed process. The schematic concept is in Fig.2.4. The heat source can be a laser beam, electron beam, or an arc. The printing process incorporating arc as the heat source is known as Wire and Arc Additive Manufacturing (WAAM). More details of WAAM is addressed in Section.2.1.4.

Some DED wire-feed process technologies are Electron beam freeform fabrication (EBF) and Wire and Arc Additive Manufacturing (WAAM).

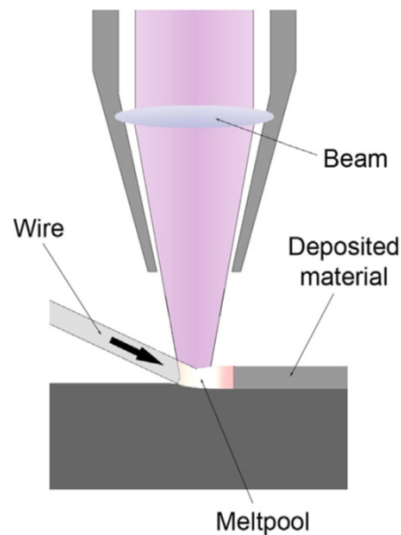


Figure 2.4: Schematic of the DED wire-based process [32][Adapted].

In contrast to the PBF process, which has the material (powder) pre-laid before heated up, the DED process's material is being melted and deposited simultaneously. One characteristic of the DED process that PBF doesn't have is the multi-material used simultaneously. DED process can incorporate different material layer by layer or within the layer.

2.1.3 Comparison of WAAM and SLM/DMLS on printing metallic structural components

The successful utilization of AM triggers the research interest of applying AM to produce complex metal structural components. The designed geometry, which is mostly linear, now becomes complex and could possess an organic characteristic.

Two main technologies, SLM and WAAM, used in the Architectural and Structural engineering discipline, are discussed and compared in this section.

Printed surface quality

The additive manufacturing of steel has been widely used in the aero and mechanical industries, mainly with SLM additive manufacturing. The advantage is that its printed products have smooth finished surfaces, unlike WAAM printed products, which generally have apparent surface roughness.

Printing angle limitation

Another advantage of SLM is that the printing of protrude parts needs no dedicated support. In contrast, for WAAM, any printed part that has an overhang angle (Fig. 2.5) larger than 45 degrees from the vertical direction does need support for printing [33]. However, current printing methods combined with a rotatory table could reduce an overhang's effect and provide more possibility for printing. Moreover, several techniques were under research and development, such as Multi-directional Additive Manufacturing or Multi-orientational Additive Manufacturing, which can manifest the overhang components' printing without any support.

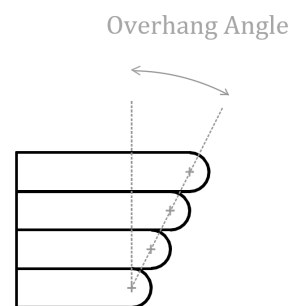


Figure 2.5: Overhang Angle

A multi-directional WAAM process control strategy [34] provides the method of printing horizontally, which considers the correlation of gravity and the printing process parameters (e.g., the wire feed speed (WFS), the torch travel speed (TS), the weld bead geometry, and torch angle). The result shows a potential of printing curved or cylinder objects horizontally on a curved surface with the use of Gas Metal Arc Welding (GMAW) (See Fig. 2.6). It can be expected that the future of WAAM printing is able to print free-form structures without the support, which could reduce more cost and enhance the efficiency of the productions.

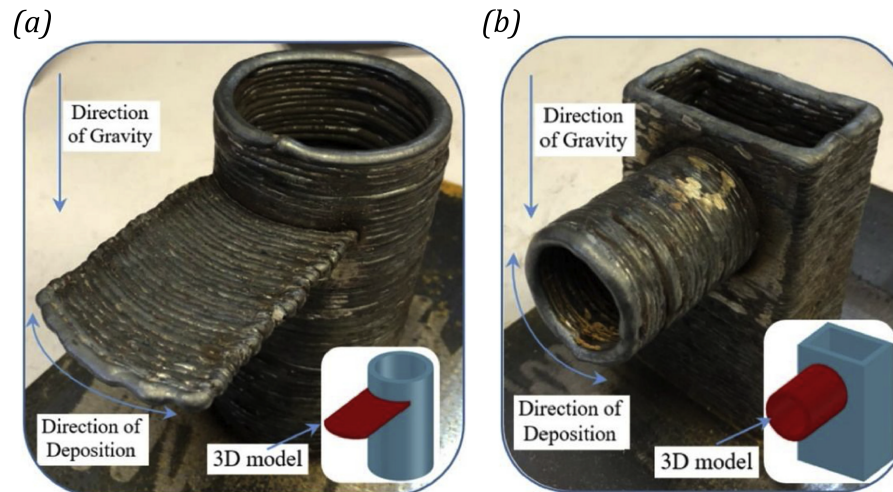


Figure 2.6: The horizontal WAAM printed objects [34]. (a) Curved thin layer printed on a curved WAAM printed surface. (b) A cylinder printed horizontally on a flat WAAM printed surface.

Limitation of the objects' printing size

SLM is also applied in the construction field but is limited to small build sizes because of its printed nature. All printed parts' scales are limited to the printer's powder bed size, which in general is below meter scale. Therefore, the WAAM technology, which has its heat source and wire-feed material supply mounted on the robotic arm, can print large components to several meters' spans [35].

Deposition rate (Production rate)

The advantage of WAAM in comparison to powder-based processes (SLM/DMLS) is the printing speed, which increase proportionately with the deposition rate [36]. SLM has a deposition rate of 0.1 kg/h, as for WAAM, the deposition rate is generally around 5-6 kg/h [37].

Residual stresses

The austenitic stainless steel used for WAAM shows better thermal expansion than carbon steels (50% greater). However, it has a comparatively low thermal conductivity coefficient (15 W/m°C); when combined with the effect of high heat input for greater deposition rate, steeper thermal gradients were created and caused high residual stresses and distortions during welding [37] [1].

Printing cost

The Laser powder-based additive manufacturing process are too expensive for printing large structural components. Two aspects are discussed, one is the power (KWh) used per kilogram, and the other is the cost of material per kilogram. Comparison can be seen in Fig.2.7 and Fig.2.8 [38].

The energy consumption of printing WAAM (5.18 kWh/kg) is much lower than the DMLS (62.9 kWh/kg) (Fig.2.7).

The feedstock material for WAAM is less pricey compared to the same material when the powder-based techniques (DMLS) is considered. For the stainless steel material, the DMLS process cost €926/kg and of which €79 is for the raw material, the cost largely comes from the machine cost. The average cost of WAAM process is €130/kg and of which €12 is for the raw material (Fig.2.7). This comparison exclude the post-processing cost.

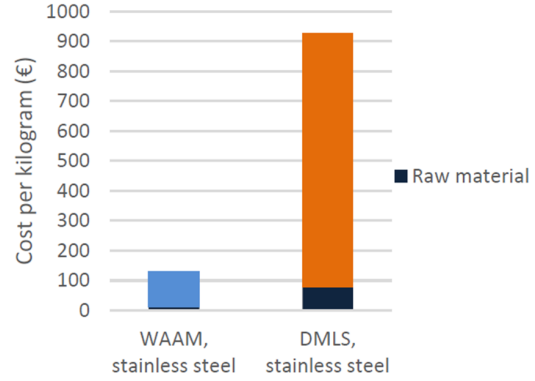
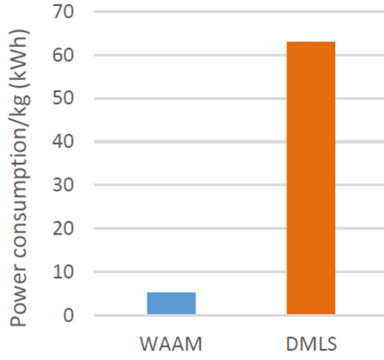


Figure 2.7: Power consumption of metal (KWh/kg) Figure 2.8: Cost estimation of metal (*euro*/kg) [38]. [38].

2.1.4 Introduction of Wire and Arc Additive Manufacturing (WAAM)

Wire and Arc Additive Manufacturing (WAAM), also known as “shape welding”, combines arc welding and wire feed-stock for printing 3D objects. While intergrated with computer aided planning, digitalisation design, and robotic production process. New possibility of producing large steel parts for construction field have been discovered.

Three main types of WAAM

WAAM shapes components by layering up the metal wire, which is heated up by an electric arc.

Three main types of WAAM are: Gas Metal Arc Welding (GMAW), Gas Tungsten Arc Welding (GTAW, also known as Tungsten inert gas (TIG) welding), and Plasma Arc Welding (PAW) [39] [36], their configurations can be seen in Figure.2.9).

GMAW is a welding process in which the electric arc forms between the feed wire and the workpiece metal plate, and the wire is typically perpendicular to the workpiece. GTAW and PAW use tungsten electrodes to produce the electric arc. PAW has additional plasma gas to form a plasma arc, which provides up to three times higher energy than GTAW welding. Unlike the GMAW, the wire feed of GTAW and PAW orientations varies [28].

Each WAAM process has different advantages. The GMAW offers higher disposition rates (see Table.2.2, which prints two to three times faster than other types of WAAM. The PAW has the highest quality welds with minimum distortion due to its highest density arc and narrower temperature zone [39].

The disposition rate directly influences the printing time and the printing cost. For a large object, such as a structural component, the use of GMAW is more suitable. Lab test specimens in Van Bolderen’s research are all produced by GMAW.

Table 2.2: Different types of WAAM technologies and their disposition rate [36].

WAAM	Energy Source	Disposition rate	
GMAW based	GMAW	Typically 3-4 kg/hr	High
	Cold metal transfer (CMT)	Typically 2-3 kg/hr	
	Tandem GMAW	Typically 6-8 kg/hr	
PAW based	Plasma	Typically 2-4 kg/hr	Mid
GTAW (TIG) based	GTAW	Typically 1-2 kg/hr	Low

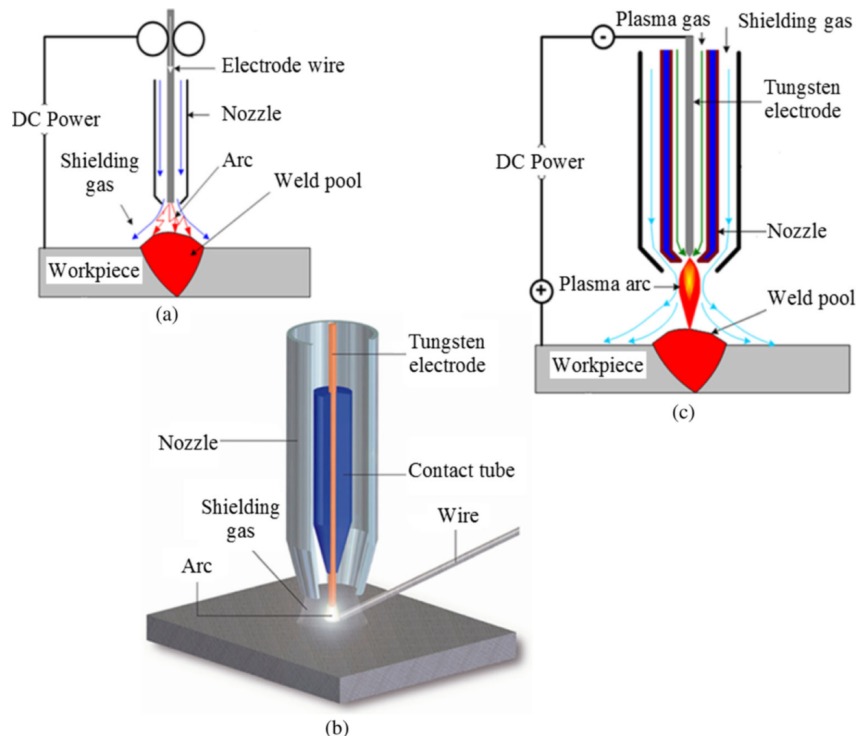


Figure 2.9: Different types of welding method. (a) GMAW, (b) GTAW, and (c) PAW [28].

Printing material of WAAM - Stainless steel

The predominant stable phase microstructure classifies stainless steel types for WAAM printing at room temperature after the alloy has been heated up to 1050°C for 30 minutes and then quenching in water for solidification. Five main types of stainless steel classified by the Schaeffler diagram (Fig.2.10) are ferritic, martensitic, austenitic, duplex, and precipitation hardenable [40] [41].

Ferritic stainless steel alloys contains 11%wt - 19%wt of chromium and small amount of nickel. Molybdenum are commonly alloyed with the stainless steel alloys that has little nickel in the content to enhance corrosion resistance. Martensitic stainless steel alloys contain a close amount of chromium and nickel as Ferritic stainless steel alloys. The difference is that Martensitic has higher carbon content, which solidifies from Austenitic alloy to Martensitic at high temperature and makes this material challenging to use for welding. Austenitic stainless steel alloys have a higher amount of nickel that retains the austenitic structure while cooling, giving an advantage of the mechanical properties unaffected by welding. The general composition of Austenitic stainless steels is 18wt% Cr-8wt% Ni. Small adjustments of the alloys are added to attain different mechanical behavior. Duplex Stainless steel has high strength and corrosion resistance from the dual content of around 50% ferritic structure and 50% austenitic structure. Precipitation Hardenable Stainless Steels allow carbide precipitation to affect the stainless steel alloys to attain high strength and toughness [40].

The material 308LSi used in this thesis research (marked green in Fig.2.10) is an austenitic type stainless steel that contains ferrite. It has both good weldability and corrosion resistance.

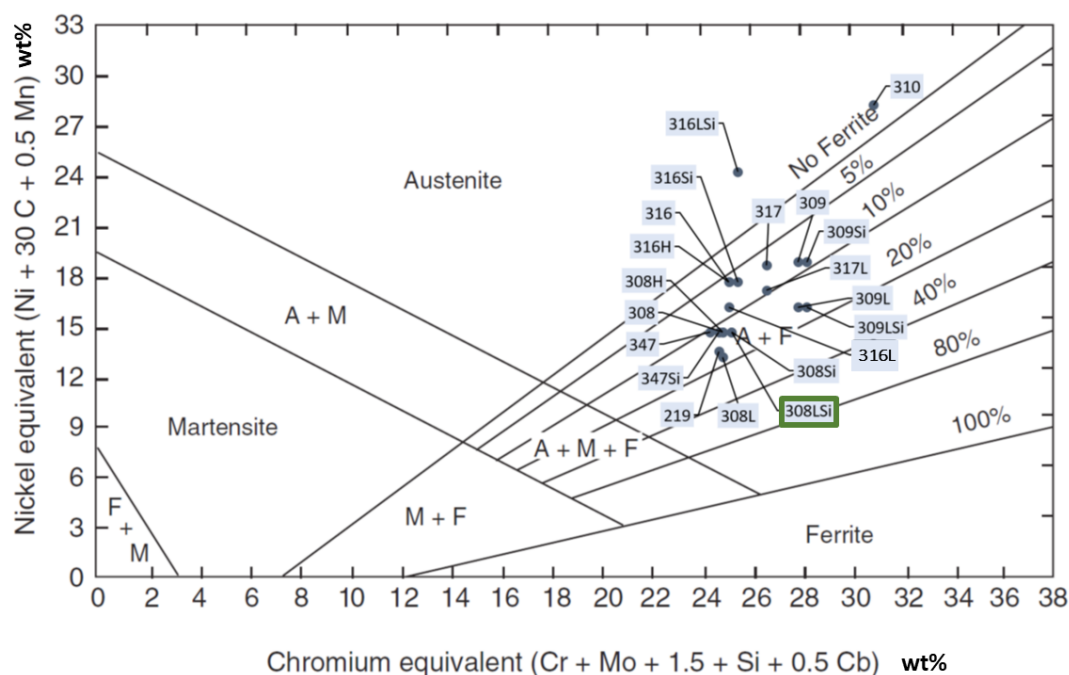


Figure 2.10: Schaeffler diagram to distinguish various types of stainless steel by their solidified phases [Adapted] [40].

WAAM components' mechanical properties

The mechanical behaviour of WAAM steel are very much unlike the conventional hot-rolled steel production. Two recent WAAM tensile test (printed in 308LSi stainless steel) [1] [42] were performed in both longitudinal and transverse directions. The result shows that, when compared the WAAM tubes to the hot-rolled S355 structural steel, the Yield strength (YS) or are in the same strength level, and the Ultimate tensile strength (UTS) are all slightly higher. The young's modulus (E) on both tests and printed direction is about 120 to 140 GPa, which are around 60 to 70 percent of conventional hot rolled steel product (E=210 GPa). The comparisons are in Table. 2.3.

Table 2.3: Material properties of WAAM and conventional steel

Material properties		E (GPa)	YS (MPa)	UTS (MPa)
Tensile test 1 [1]	Longitudinal	137	307	544
	Transverse	121	321	568
Tensile test 2 [42]	Longitudinal	129	356	553
	Transverse	105	352	513
Structural Steel S355 according to EN1993-1-1	Hot rolled products - Non-alloy structural steels according to EN10025-2 (nominal thickness $t \leq 40\text{mm}$)	210	355	490

Challenges and limitations of WAAM

WAAM has the ability to “shape-weld” large steel components with almost zero waste and is cheaper and more efficient compared to other types of AM. However, several challenges and limitations exists [1] [39]:

- Distortion and high residual stresses due to high heat input.
- Rough surface finish compared to powder-based AM and conventional steel production.
- Lack of integrated process monitoring and difficult at controlling deposition process.
- Anisotropic material properties.

- Limited printing angle due to the collapsing of the weld pool.

2.1.5 Experimental research of AM (SLS and WAAM) in Architectural and Structural engineering discipline.

Researches have been carried out to utilize the production freedom that AM has to bring new architectural and structural design ideas. Four examples are presented below.

First, an AM (Selective laser sintering) node case study conducted by ARUP simplified a node from tensegrity structure by using topology optimization method [43]. The process mimics the interaction of form, material, and structure from the observation of nature. The optimized shape (Fig.2.11) has been obtained from the iterations of the behavior of force, material, and boundary conditions that define the node. The optimized geometry shows a complex organic shape that could not be produced in a conventional way. The node's weight has been reduced to 25% but still has similar structural behavior.

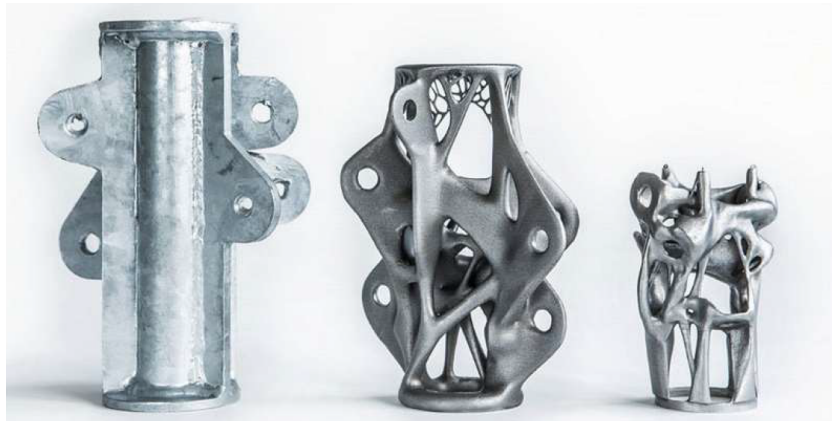


Figure 2.11: Advancement of a topology optimised tensegrity structure node. (Left: Traditional node - 20kg; Middle: AM node first generation - 14kg; Right: AM node second generation - 5kg.)

Second, a complex AM (Wire and Arc Additive Manufacturing) nodes research performed by Delft University of Technology (TU Delft) has been used in the structural optimized glass swing [26]. This project shows the practicality of printing unique nodes at tight angles on a non-planer object (the center conventional cast space frame node) with the help of a rotatory table.



Figure 2.12: TU Delft glass swing. Left: The overview of the glass swing; Middle: The most complicated node in the swing (the top node), and Right: The rotatory table for printing a node.

Third, a AM (WAAM) semi-size 2m diagrid column have been printed for supporting lightweight outdoor structure, i.e, a tree house (Fig.2.13) [35]. The project has been carried out to showcase the 3D metal printing possibility in "The Big 5-International Building and Construction 2018" exhibition. The shape of the diagrid column has been parametrically and topologically designed. This innovative AM process, from concept to fabrication, unlocks the potential of a new generation of novel shape structures.



Figure 2.13: AM diagrid column [35]. (Left: The manufacturing of AM diagrid column, Right: The application of the diagrid column as a tree-house support.)

Fourth, a 10.5m span, the world's first AM (WAAM) footbridge have been realized by MX3D. The elegant curvy bridge frame have been topology optimized and printed from a 6-axis ABB industrial robot. Simulation and initial verification have been made to assure the strength for disclosing it to the public exhibition [21].



Figure 2.14: MX3D AM (WAAM) bridge. (Left: Overview of the bridge; Right: The bridge under printing.)

2.2 Types of shell analysis defined in Eurocode 3

For the Finite Element Analysis (FEA), the WAAM printed components are considered to be shell structures and can apply Eurocode 3 (EN 1993-1-6): Design of steel structures - Part 1-6: Strength and stability of shell structures [23].

In total, seven shell analysis types are organized with the knowledge from this Code of Practice and annotated with explanations [44]. The comparisons of shell analysis types can be seen in Table.2.4.

LA – Linear analysis

Low stress performs on the model shows that there is no risk of yielding, and enough slenderness shows there is no risk of instability. This analysis is usually used to check whether the model or the load settings are correct or not.

- Below are the assumptions:
 - Analysis that predicts the behavior of a thin-walled shell structure
 - Based on a small deflection
 - Linear elastic material
 - Perfect geometry of the middle surface of the shell

LBA – Linear elastic bifurcation (eigenvalue) analysis (LBA)

This analysis is also called Linear Buckling analysis. It provides eigenvalue, which refers to a linear load multiplier that represents the critical load (ie. Euler's force of the compressed column).

- Below are the assumptions:
 - Analysis that evaluates the bifurcation eigenvalue of a thin-walled shell structure
 - Based on a small deflection
 - Linear elastic material
 - Perfect geometry of the middle surface of the shell
 - The eigenvalue does not relate to vibration modes

GNA – Geometrically non-linear elastic analysis

In this analysis, loads are divided into increments to increase the accuracy of the solution. The results of this analysis made the stability path, which shows the load at which the ideal elastic instability occurs and the form of the instability.

- Below are the assumptions:
 - Analysis based on principles of shell bending structures
 - Based on non-linear large deflection theory for displacement
 - Linear elastic material
 - Perfect geometry

MNA – Materially non-linear analysis

In this analysis, loads are divided into increments to increase the accuracy of the solution. The results of this analysis made the stability path, which shows the load at which the ideal elastic instability occurs and the form of the instability.

- Below are the assumptions:
 - Analysis based on principles of shell bending structures
 - Based on a small deflection
 - Non-linear elasto-elastic material
 - Perfect geometry

GMNA – Geometrically and materially non-linear analysis

This analysis shows the combination of two non-linearity. This analysis gives ideas about how material's elastic properties influence instability or how model yields after stability failure.

- Below are the assumptions:

- Analysis based on principles of shell bending structures
- Based on non-linear large deflection theory for displacement
- Non-linear elasto-elastic material
- Perfect geometry
- Bifurcation check at each load level

GNIA – Geometrically non-linear elastic analysis with imperfections included

On top of GNA, this analysis includes imperfections in the model that can greatly represent what the structure in the real world will be. The analysis uses elastic material.

- Below are the assumptions:
 - Analysis based on principles of shell bending structures
 - Based on non-linear large deflection theory for displacement
 - Linear elastic material
 - Imperfect geometry (Including the deviation from the ideal shape, imperfections in boundary conditions and residual stresses)
 - Bifurcation check at each load level

GMNIA – Geometrically and materially non-linear analysis with imperfections included

Adding up all the characteristics of GMNA, this analysis considers the imperfection. Among all the analysis types, this type is the most thoughtful in combining the most complete influences from the physical world. It is the most sophisticated analysis, and the outcome is closest to the genuine value.

- Below are the assumptions:
 - Analysis based on principles of shell bending structures
 - Based on non-linear large deflection theory for displacement
 - Non-linear elasto-elastic material
 - Imperfect geometry (Including the deviation from the ideal shape, imperfections in boundary conditions and residual stresses)
 - Bifurcation check at each load level

Table 2.4: Types of shell analysis [23]

Type of analysis	Shell theory	Material law	Shell geometry
Membrane theory of shells	membrane equilibrium	not applicable	perfect
Linear elastic shell analysis (LA)	linear bending and stretching	linear	perfect
Linear elastic bifurcation analysis (LBA)	linear bending and stretching	linear	perfect
Geometrically non-linear elastic analysis (GNA)	non-linear	linear	perfect
Materially non-linear analysis (MNA)	linear	non-linear	perfect
Geometrically and materially non-linear analysis (GMNA)	non-linear	non-linear	perfect
Geometrically non-linear elastic analysis with imperfections (GNIA)	non-linear	linear	imperfect
Geometrically and materially non-linear analysis with imperfections (GMNIA)	non-linear	non-linear	imperfect

2.3 The structural principle of moment resistant joint on gridshell

With more drastic structures have been designed to realize the architectural representation, the complex joints in the system have lead to complicated production scenarios and higher needs of skilled labor. Owing to computer-aided software development, structures become more free-formed and optimized, requiring large amounts of highly customized joints to construct. A typical type of this structure is the gridshell. One famous example is Złote Tarasy, a beautifully designed single layer wavy gridshell structure in Warsaw, Poland with 10150 joints and 7600 elements [45].

In the double-layered truss space frame, members are pinned to the joints and take the bending moments in the structure with tension and compression force in the axial direction. Unlike joints in the space frame, these 10150 joints in the single-layered gridshell have to take axial force and the bending moment transferred from the members to guarantee structural integrity.



Figure 2.15: The Złote Tarasy. [45]. Left: Exterior view of the wavy roof. Right: Interior view.

To understand the moment-resisting joint's design mechanisms and strength behavior in gridshell structure, joint type studies of gridshell structures are presented in Section.2.3.1, and the joint strength

classification is introduced in Section.2.3.2.

One important consideration of the joint proposed in Ch.5 is to provide a methodology with a simple and reasonable design joint for the future lab experiment to examine the joint strength (future work). Therefore, the research of gridshell joints' lab experiment is reviewed in 2.3.3.

2.3.1 Types of moment resistant joints in gridshell structures

Two types of conventional joints in gridshell structure prevails: Splice joint and End-face joint. These joint types can either be bolted, welded or both.

Splice joints (Fig.2.16) have a long contact surface between the node and connected members. At the connecting area, two parts are layering up to each other. The welds or bolts applied provide shear resistance. The horizontal and vertical angles can be adjusted. As for twist angle, little room is reserved for the adjustment.

End-face joints (Fig.2.17) have members connect to the node at their end-face. The contact surface is transverse to the longitudinal axis of the member. The bolts or welds take tension at the fixing. The vertical angle can be adjusted by slicing the node face. The room for the twist angle is limited.

The behavior and the applicability of the mentioned joint types are organized in Table.2.5. To summarize, unlike most splice joints, which require the free-form structure to be structurally and geometrically optimized, most end-face joints are more flexible to apply in the project and do not need structural and geometrical optimization. In general, for the same joint, welded connecting method has larger bending stiffness than the bolted method.

Gridshell projects that use the joints mentioned above in practice are listed in Table.2.6.

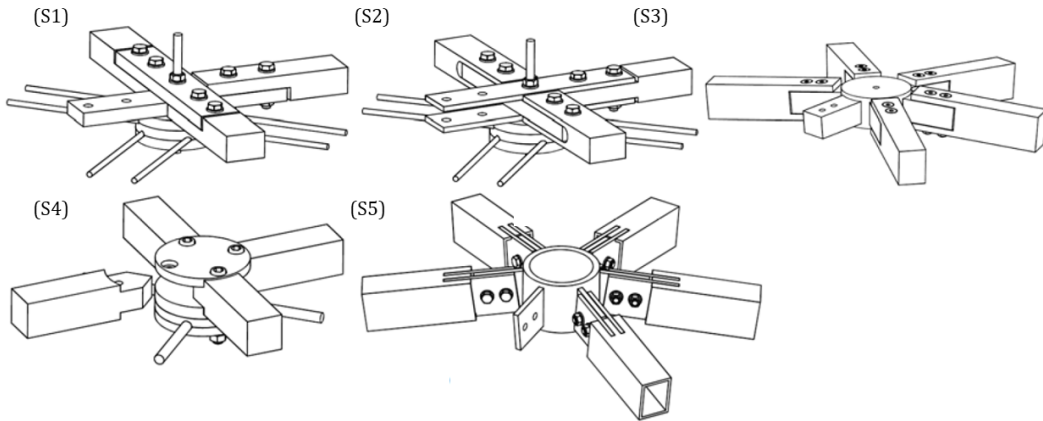


Figure 2.16: Splice joint types for gridshell structure. (S1) Splice joint SBP-1, (S2) Splice joint SBP-2, (S3) Splice joint SBP-3, (S4) Splice joint HEFI-1, and (S5) Splice joint POLO-1 [46].

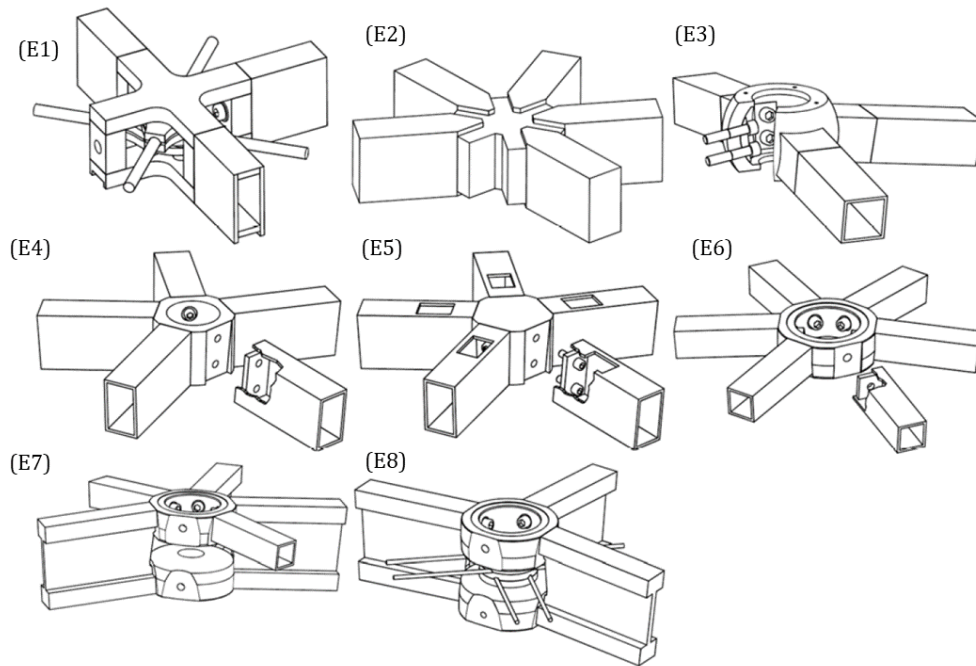


Figure 2.17: End-face joint types for gridshell structure. (E1) End-face connector SBP-4, (E2) End-face connector WABI-1, (E3) End-face connector OCTA-1, (E4) End-face connector MERO-1, (E5) End-face connector MERO-2, (E6) End-face connector MERO-3, (E7) End-face connector MERO-4, and (E8) End-face connector MERO-4-improved [46].

Table 2.5: Applicability of the joints for free-form gridshell structures [46].

Node Connector		Accommodation of Local Geometry			Transferability of Internal Forces		Applicability
Version	Connection	Horizontal Angle U_i	Vertical Angle V_i	Twist Angle W_i	Normal Forces	Bending Moments	Free-Form Structure Type
SBP-1	Bolted Splice	+	+	O	+	O	Geom. Optim., Struct. Optim.
SBP-2	Bolted Splice	+	+	O	++	+	Geom. Optim., Struct. Optim.
HEFI-1	Bolted Splice	++	+	+	++	++	Geom. Optim., Struct. Optim.
SBP-3	Bolted Splice	++	++	++	++	++	Geom. Non-Optim., Struct. Non-Optim.
POLO-1	Bolted Splice	++	++	++	++	++	Geom. Non-Optim., Struct. Non-Optim.
SBP-4	Welded End-Face	+	+	O	+++	+++	Geom. Optim., Struct. Non-Optim.
WABI-1	Welded End-Face	++	++	+	+++	+++	Geom. Non-Optim., Struct. Non-Optim.
OCTA-1	Bolted End-Face	++	+++	++	++	++	Geom. Non-Optim., Struct. Non-Optim.
MERO-1 (Cylinder)	Bolted End-Face	++	++	+	++	++	Geom. Optim., Struct. Non-Optim.
MERO-2 (Block)	Bolted End-Face	++	+++	++	++	++	Geom. Non-Optim., Struct. Non-Optim.
	Welded End-Face	++	+++	++	+++	+++	Geom. Non-Optim., Struct. Non-Optim.
MERO-3 (Dish)	Bolted End-Face	++	++	++	++	+	Geom. Non-Optim., Struct. Optim.
	Welded End-Face	++	+++	++	++	++	Geom. Non-Optim., Struct. Non-Optim.
MERO-4 (Double Dish)	Bolted End-Face	++	++	+	++	++	Geom. Non-Optim., Struct. Non-Optim.
	Welded End-Face	++	+++	++	+++	+++	Geom. Non-Optim., Struct. Non-Optim.
Notation		O Limited Suitability			Geom. Optim. Geometrically Optimized Surfaces		
		+ Adequate Suitability			Geom. Non-Optim. Geometrically Non-Optimized Surfaces		
		++ Good Suitability			Struct. Optim. Structurally Optimized Surfaces		
		+++ Excellent Suitability			Struct. Non-Optim. Structurally Non-Optimized Surfaces		

Table 2.6: Joints used in the real projects [46].

Types and name of joints	Project titles
(S1) Splice joint SBP-1	The courtyard roof of the City History Museum in Hamburg
(S2) Splice joint SBP-2	The railway station Berlin-Spandau
(S3) Splice joint SBP-3	The DZ-Bank in Berlin
(S5) Splice joint POLO-1	The railway station in Cologne
(E1) End-face connector SBP-4	The German Historical Museum in Berlin
(E2) End-face connector WABI-1	The British Museum in London
(E7) End-face connector MERO-4	The New Milan Trade Fair

2.3.2 Joint classification

Joint classification is based on the joint stiffness and the moment capacity. The stiffness of joints largely influences the mechanical performance of gridshell structures. The global stability and global buckling of the structure are also influenced by the joint stiffness. Therefore, knowing the stiffness and moment capacity of the joint for preliminary gridshell design is crucial.

The behavior of beam-to-column joints in steel frame has been studied comprehensively; however, little research has been focused on joints applied in gridshell structures. A joint classification method proposed by Fan et al. [47] effectively categorizes the joint by the stiffness (determination coefficient α) and the moment capacity (determination coefficient β).

Joint classification based on stiffness k - determination coefficient α

From the study of the joint stiffness, a two-member structure with rigid joint (Fig.2.18(a)) is compared with one with a flexible joint whose stiffness is k (Fig.2.18(b)).

The structure deformed when the load P is applied. The equilibrium state of the deformed flexible structure can be seen in Fig.2.18(c). The relation of the bending moment and the angle θ are given by Eq.2.1 and Eq.2.2. M_{zr} refers to the two-member structure with a rigid joint, and M_{zf} refers to the two-member structure with a flexible joint.

$$M_{zr} = \frac{4EI}{L_0} (\theta_0 - \theta) + \frac{6EI}{L_0} \cos \theta (\sin \theta_0 - \sin \theta) \quad (2.1)$$

$$M_{zf} = k \times 2 (\theta_0 - \theta) \quad (2.2)$$

In the formulas, L_0 is the length of the member, θ_0 is the initial angle of the member to the horizontal, θ is the deformed angle of the member to the horizontal, E is Young's modulus of the material, and I is the moment of inertia of the member.

When the stiffness of the flexible joint k increase to the extent that $M_{zf}=M_{zr}$, the stiffness of the k that reached rigid state can be derived:

$$k \times 2 (\theta_0 - \theta) = \frac{4EI}{L_0} (\theta_0 - \theta) + \frac{6EI}{L_0} \cos \theta (\sin \theta_0 - \sin \theta) \quad (2.3)$$

Rearranging the equation:

$$k = \frac{2EI}{L_0} + \frac{3EI (\sin \theta_0 - \sin \theta)}{L_0 (\theta_0 - \theta)} \cos \theta \quad (2.4)$$

Since the deformation taken into the consideration is very small, θ_0 and θ are very as well. Thus, $\sin \theta_0 \approx \theta_0$ and $\sin \theta \approx \theta$. Previous equation becomes:

$$k = \frac{2EI}{L_0} + \frac{3EI}{L_0} \cos \theta \quad (2.5)$$

Also, because $\theta \approx 0$, $\cos \theta \approx 1$. Therefore, previous equation can be further simplified into:

$$k = \frac{5EI}{L_0} \quad (2.6)$$

Until this step, the value of the stiffness k that indicates that the flexible structure acting like a rigid structure can be known, and the determination coefficient α comes into play:

$$\alpha = \frac{k}{EI/L_0} \quad (2.7)$$

Here, the EI/L_0 represents the stiffness of the members, which connects to the joint. Hence, α correlates with the joint stiffness.

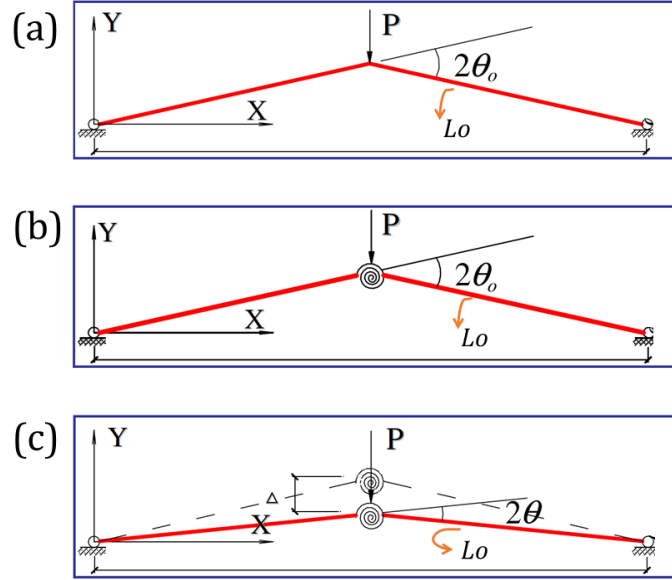


Figure 2.18: Two-member structure [47]. (a) The structure with rigid joint, (b) The structure with flexible joint, and (c) The equilibrium state of the deformed flexible structure.

Based on the concept of using determination coefficient α for categorizing joint stiffness, a parametric analysis has been carried out to look into the effect of joint stiffness. The result is shown on the left of Fig.2.19. The critical load does not have an apparent variation after the determination coefficient α reaches 5 or below 0.05. Therefore, the stiffness of joints have been categorized into Rigid, Semi-rigid, and Pinned (see Table.2.7).

Table 2.7: Categorization of gridshell structure by the stiffness.

Categories	Determination coefficient α
Rigid	$\alpha \geq 5$
Semi-rigid	$5 > \alpha > 0.05$
Pinned	$\alpha \leq 0.05$

Joint classification based on moment capacity - determination coefficient β

In addition to the stiffness of the joint, the moment capacity also influences the mechanical behavior of the joint. A determination coefficient β for classifying moment capacity is written down as:

$$\beta = \frac{M_{j,u}}{M_{e,u}} \quad (2.8)$$

In the equation, $M_{j,u}$ represents the moment capacity of joints, and $M_{e,u}$ means the moment capacity of the connected members.

Another parametric analysis has also been carried out to discover the moment capacity of joints. The result is shown on the right of Fig.2.19. The value of the critical load does not have an obvious change after the determination coefficient β reaches 0.5 or below 0.01. Therefore, the moment capacity of joints have been arranged into three categories: Rigid, Semi-rigid, and Pinned (see Table.2.8).

Table 2.8: Categorization of gridshell structure by the influence of moment capacity.

Categories	Determination coefficient β
Rigid	$\beta \geq 0.5$
Semi-rigid	$0.5 > \beta > 0.01$
Pinned	$\beta \leq 0.01$

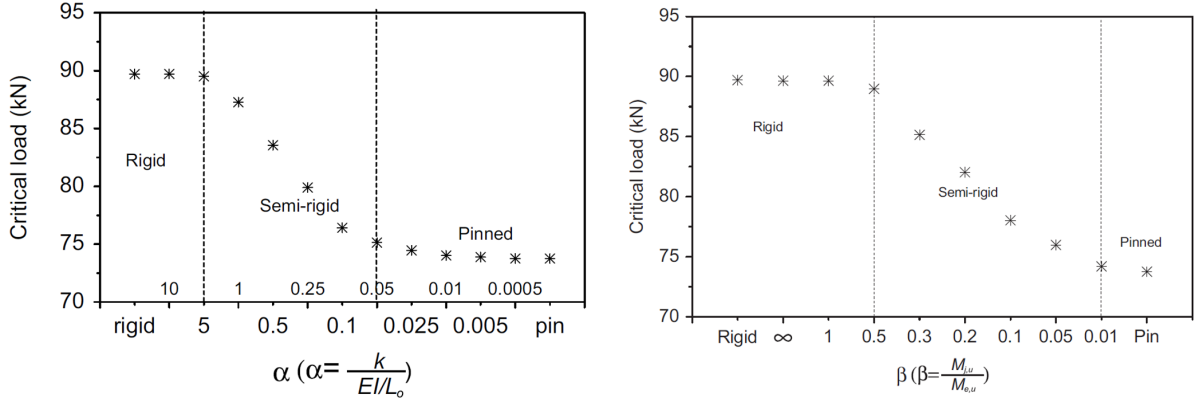


Figure 2.19: Critical load with different determination coefficients [47]. Left: Determination coefficient α , Right: Determination coefficient β .

Combined classification - determination coefficient α and β

The moment-rotation curve contains the information of both the stiffness and the moment capacity of the joint (see Fig.2.20(a)), which are acquired from the slope and the moment value at the end of the curve.

The reason for incorporating not only the stiffness but also the moment capacity in the joint classification is that two joints could have the same stiffness k but with different moment capacity ($M_{j,u,1}$, $M_{j,u,2}$) (see Fig.2.20(b)).

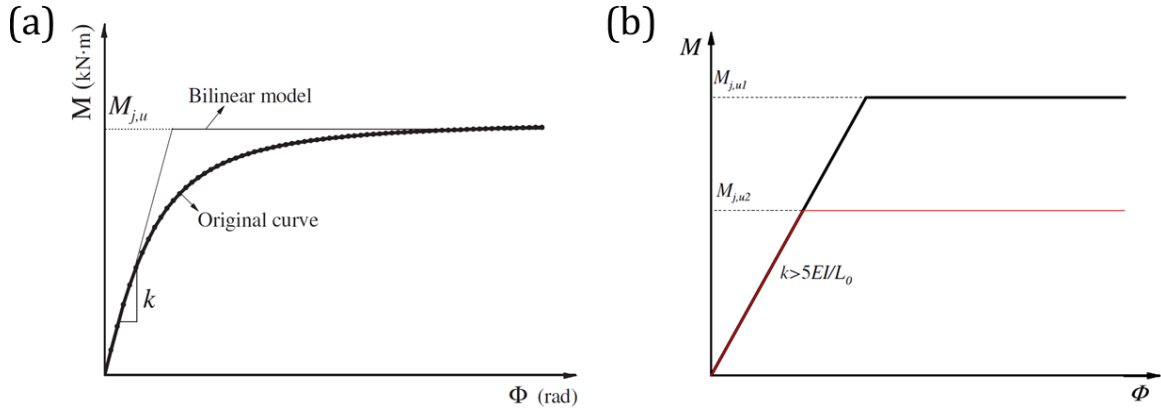


Figure 2.20: Moment-rotation curve [47]. (a) Acquiring flexural stiffness and moment capacity from the moment-rotation curve, (b) Two joints with the same stiffness but different moment capacity.

The combined classification, which incorporate the determination coefficient of α and β , is defined in Table.2.9. The interaction chart can be seen in Fig.2.21. It is noted that for designing a gridshell structure, using the joint with $\alpha=5$ and $\beta = 0.5$ has a similar mechanical behavior as the one with $\alpha \gg 5$ and $\beta \gg 0.5$. In this way, more material can be conserved, and the weight of the structure can be lighter [48].

Table 2.9: Categorization of gridshell structure by the influence of stiffness and moment capacity.

Categories	Determination coefficient α and β
Rigid	$\alpha \geq 5$ and $\beta \geq 0.5$
Semi-rigid	$\alpha > 0.05$ and $0.01 < \beta < 0.5$, or $\beta > 0.01$ and $0.05 < \alpha < 5$
Pinned	$\alpha \leq 0.05$ and $\beta \leq 0.01$

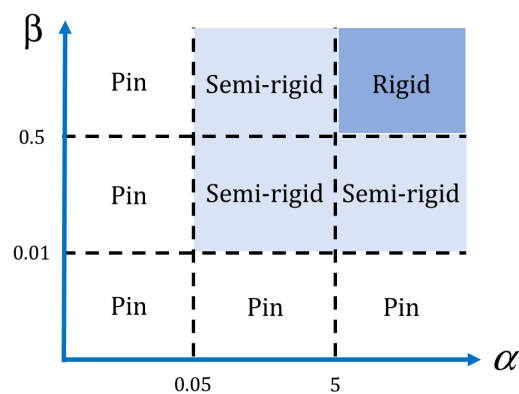


Figure 2.21: The interaction chart of combined classification of joints based on determination coefficient α and β .

2.3.3 The FEA and lab experiment review of gridshell joints

The rigidity of three welded moment resistant joint types has been proposed by Kim et al. [49]. This study shows the concept of the joint experiment setup and a methodology for analyzing the moment-resistant joints. This review is crucial for planning a moment-resisting joint experiment, designing and conducting FEA of the proposed joint in Ch.5. This review sections arrange the knowledge in blocks that answers the following questions:

1. What is the methodology for the gridshell joints test?
2. How can the experiment be set up to acquire moment-rotation curves?
3. What are the failure modes?
4. What are the findings from the research (experiment and FEA) that might provide the opportunity for WAAM to apply its advantage on improving the design of the moment-resisting joint?

A brief background information of the grid-shell joint experiment

Lab experiments and FEA of three types of joint, CJ, ALT1, and ALT2, have been carried out in this research. The main goal is to study the flexural performance out of these three types of joints. In addition, the influence of different design parameters of ALT2 is performed in lab experiments (this will not be further discussed in this thesis review section). Several parameters including the influence of gusset plate's thickness and inserted length; steel member's connecting angle to the node, and the influence of the existence of the slot at the gusset plate tip (specified components can be seen in Fig.2.22). CJ and ALT have only one type and are presented for comparison purposes. FEA is performed to compare the lab test results with numerical results.

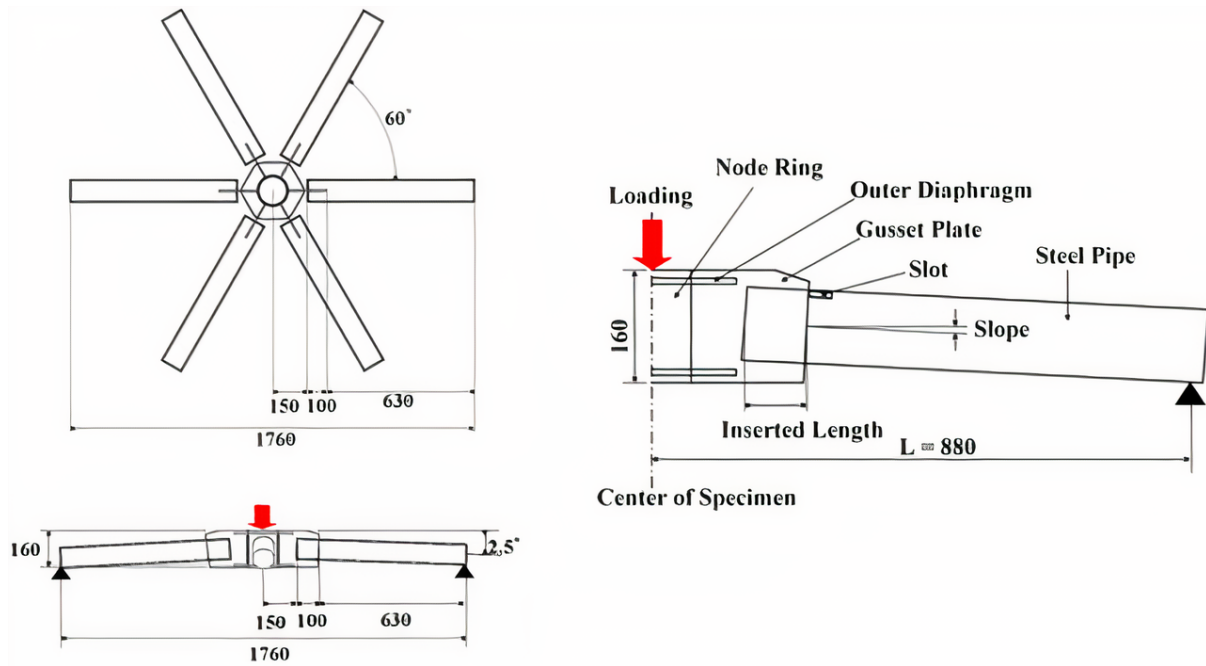


Figure 2.22: Test specimen ALT2 and parameter explanations. [49].

Three types of joint, CJ, ALT1, and ALT2 are shown in Fig.2.23. The differences between CJ and ALT1 are the node shape and the diaphragm. The node shape of CJ is circular (not sphere), and the ALT1 is hexagonal. Also, the diaphragm connects fully in the node CJ, unlike the one in ALT1. The moment resistance of CJ is expected to be higher. The differences between ALT1 and ALT2 are the length of the gusset plate and the connecting face of the node and six members. The gusset plate extends out of the node in ALT2. Compared to ALT1, the design increases the rigidity of six members' ends, which are closer to the node. For the connecting condition of ALT1, six members have circular contact with the node, whereas the six members of ALT2 only have linear contact to the node through the gusset plate.

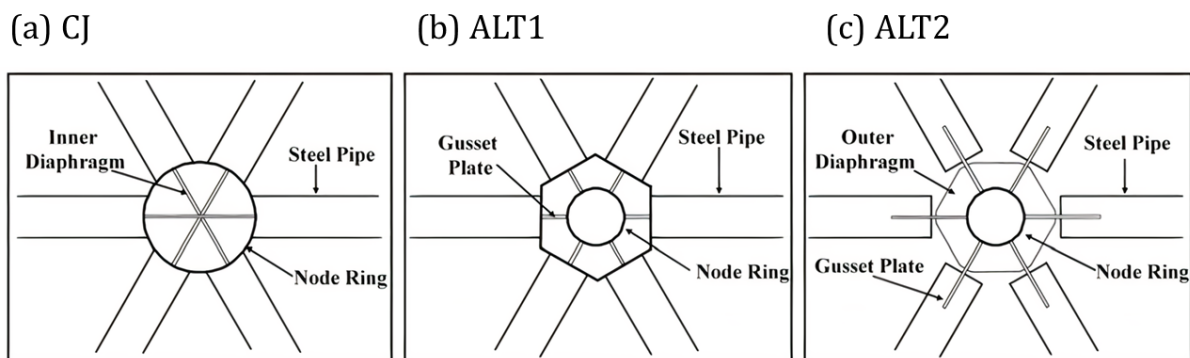


Figure 2.23: Three types of welded joint [49].

The lab experiment setup

For the lab experiment, six joint members of each node are simply supported on the hexagonal test bench. The supporting points are reinforced by crossed type stiffeners with two guide plates on the sides for safety (shown in Fig.2.24). Loads are applied at the center of the node with a 20mm circular plate to even the load distribution. The maximum oil jack load is 980KN, and the monotonic load was applied on the node with the speed of 0.05mm per second until the displacement of 100mm reached.

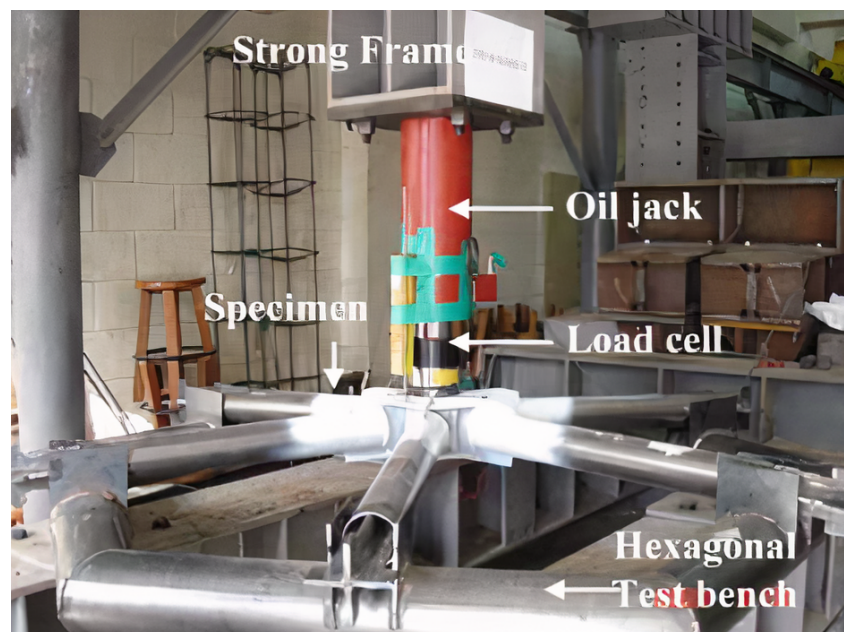


Figure 2.24: ALT2 lab setup [49].

The FEA model setup

For the FEA, joint's model are built in ANSYS (shown in Fig.2.25).

The finite element model has the setup as followed:

1. For the meshes, eight-node solid elements (SOLID 45 element) are used.
2. For the boundary conditions, the ends of the joint members (steel pipes) were simply supported. Also, the model has a displacement control of 100mm (0.113rad , the lengths from node center to members' end are the same for all joints.) at the node ring center.
3. For the material properties, isotropic non-linear material behavior has been considered.

Assumptions:

1. welding condition and residual stress are excluded

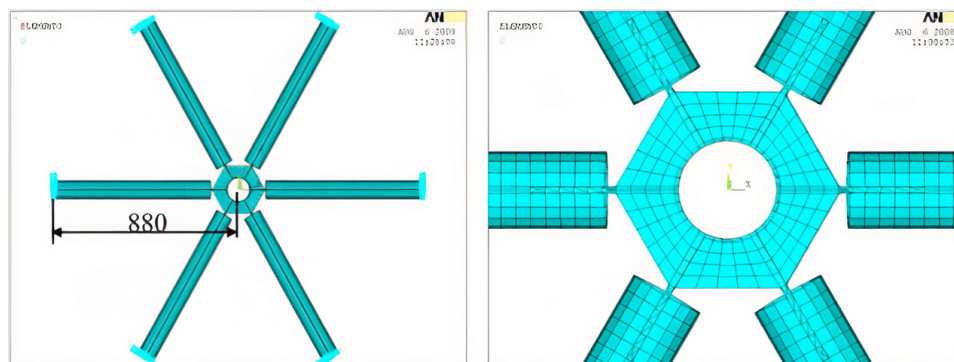


Figure 2.25: ALT2 finite element model [49].

Results of lab experiments

Moment-rotation curves are presented from the lab experiment in Fig.2.26 (Only the result of CJ, ALT1, and ALT2 are included in the review). The vertical axis expresses the moment at the node center. The horizontal axis is the rotation, which is calculated as the displacement at the node center divided by the length of the node center to the support. The failure modes of CJ, ALT1, and ALT2 are given in Fig.2.27. The ruptures occur at the bottom part (in tension) of the steel members, where they are welded to the node or gusset plate.

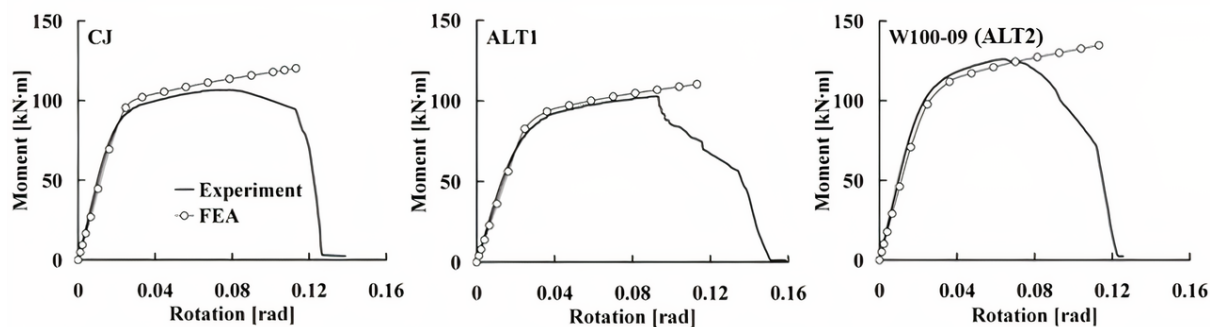


Figure 2.26: Moment-rotation curve from lab experiments and FEA. Left: CJ; Middle: ALT1; Right: ALT2 [49].



Figure 2.27: Failure modes of joints. (a). CJ, (b). ALT1, (c). ALT2 [49].

Results of the FEA

The results of flexural performance (moment-rotation curve in Fig.2.28) from FEA shows:

1. CJ has higher moment-capacity (strength) and stiffness (flexural rigidity) than ALT1. The effect comes from the complete diaphragm in joint CJ.
2. The ALT2 has slightly higher stiffness and larger moment-capacity than CJ.

The figure of Von Mises stress contour at the joint bottom side (Fig.2.29) tells:

1. Stress distributes evenly at six legs for each of the joints (six legs show the same pattern).
2. ALT1 and ALT2 has higher stress level at the node ring than CJ due to the lack of strong diaphragm.
3. CJ has a similar stress pattern as ALT1, in which the stress is concentrated at where the node and six members connect. Whereas ALT2 moves the stress concentration away from the node to the tips of extended gusset plates.
3. The strength strengthened by the outer diaphragm (ALT2) results in a higher rigidity than the diaphragm at the node (CJ).

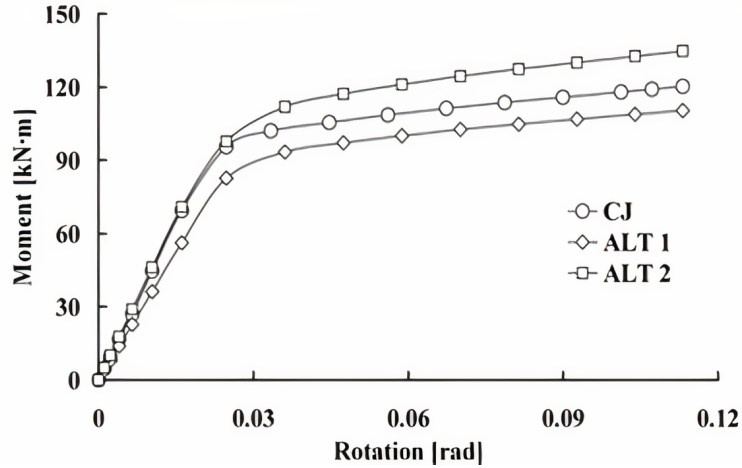


Figure 2.28: Moment-rotation curves from FEA. [49].

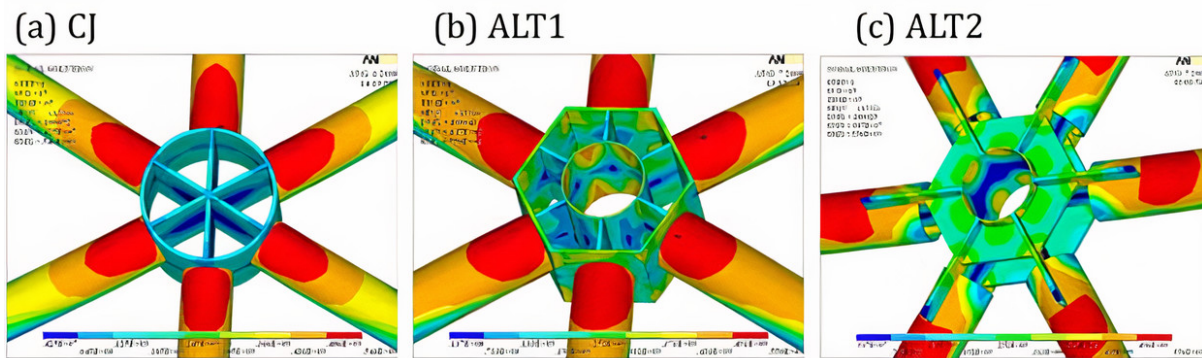


Figure 2.29: Von Mises stress at the bottom part of three joint types [49].

Result comparisons of Lab experiment and Numerical analysis

1. Moment-rotation curves of the lab result and the FEA are matching quite well (see Fig.2.26 at the elastic part and the beginning of the plastic part. (It is mentioned in the research that the FEA did not deal with fracture propagation).
2. ALT2 type shows the best in moment capacity and stiffness. The outer diaphragm plays a crucial role.
3. Rupture failures happened among these three joint types. The failure occurs at the bottom part of the steel members at the HAZ (heat-affected zone) and where the stress concentrates.

2.4 Conclusions

Three parts have been covered in the literature review of background knowledge to answer the research questions. The first part, Section 2.1 shows the state of the art of additive manufacturing, typically with WAAM technologies. The second part, Section 2.2, presents the numerical analysis guidance from EN 1993-1-6: Eurocode 3: Design of steel structures - Part 1-6: Strength and stability of shell structures for WAAM tubes. The last part, Section 2.3, discusses the requirements for designing moment-resistant gridshell joints.

Research questions in this chapter are:

- 1) What is the Wire and Arc Additive Manufacturing (WAAM), and what are its advantages compared to the powder-based method for producing large steel components?
- 2) What is the guidance in Eurocode 3 on analyzing the strength of WAAM printed components?

- 3) What are the design requirements of the moment-resistant gridshell joints.
- 4) How to estimate and classified the strength of a gridshell joint?

Benefits of using WAAM than using powder-based method (SLM/DMLS) for printing metallic structural components.

The technology of WAAM makes the production of large-scale steel structure technical possible, efficient, and cost applicable. Although the WAAM printed component has the disadvantage of residual stress and distortions, surface roughness, lower printing accuracy, and support are needed for printing. The ability to print on a large scale, significantly lower production cost (only 14% compared to powder-based printing (DMLS)), and printing time (deposition rate 50 to 60 times then powder-based printing (SLM)) still makes WAAM the preferable choice to produce 3D printed structural objects.

Hints from Eurocode 3 for analyzing WAAM printed component.

WAAM printed components are considered shell structures and can apply the Eurocode 3 (EN 1993-1-6): Design of steel structures - Part 1-6: Strength and stability of shell structures [23].

The contents of seven types of shell analysis are studied and are applied to the relevant numerical simulations in Ch.4.

First, for Linear behavior,

1. Linear analysis (LA), and
 2. Linear elastic bifurcation (eigenvalue) analysis or Linear buckling analysis (LBA)
- are considered.

Second, for non-linear behavior,

3. Geometrically non-linear analysis (GNA),
 4. Materially non-linear analysis (MNA), and
 5. Geometrically and materially non-linear analysis (GMNA),
- are integrated.

Last, for non-linear behavior including the imperfections,

6. Geometrically non-linear elastic analysis with imperfections included (GNIA), and
7. Geometrically and materially non-linear analysis with imperfections included (GMNIA) are implemented.

Design requirements of the moment-resistant gridshell joints

Five aims for designing the gridshell joint are:

1. *Moment resistant* and 2. *Flexibility*:

Joints should consider moment-resisting capability and be flexible enough to provide various angles for connecting members.

3. *Methodology wise*:

Joints should be designed in a simple and reasonable way for the future lab experiment to examine the joint's strength. The knowledge for setting up the experiment for gridshell joints is well covered in Sec.2.3.3.

4. *Apply the advantage of WAAM*:

The ability of WAAM is that it can print free-formed structures within its printing limit. The stress concentrations between the node and the members can be mitigated with the gradually increased printed diameter, making it a funnel-shaped member that prints to the node. Also, smoother printing geometry can probably avoid and reduce the fatigue of the joint.

5. *Manufacturable*:

After fulfilling all the ideas with the design of WAAM, joints must be printable. With the aid of a rotational table during the WAAM printing process, the limitation of printing angles can be reduced.

Moment rotation curves and joint classifications.

The strength of the joint can be acquired from the flexural experiment of gridshell joints (covered in Sec.2.3.3). The results of moment-rotation curves can be used to classify the joint's rigidity using flexural stiffness and moment capacity. Determination coefficient α and β indicates the joint to be rigid, semi-rigid or pinned (see Sec.2.3.2).

Chapter 3

Reviews of four WAAM mechanical lab tests

This review chapter is based on the research of WAAM printed tubes from Van Bolderen [1] and focusing on the continuous printed circular component parts.

Important information for understanding the process of the lab experiment as well as the results for further numerical simulation in Ch4 is presented and discussed in this chapter.

General knowledge for all the lab tests is provided in Section3.1. The review of the tensile test, the compression test, the four-points bending test, and the buckling test is presented in Section3.2, Section3.3, Section3.4, and Section3.5. Section3.6 answers the research questions in this section.

Research questions in this chapter are:

- 1) What are the imperfections of WAAM components in the review of lab tests?
- 2) What is the setup for each mechanical test?
- 3) What lab test results are presented in each of the mechanical tests and are being used in numerical simulations in Ch4?

3.1 General knowledge

This section presents the general knowledge of lab tests and samples, including printing material and the parameters used in Van Bolderen's thesis, knowledge for acquiring material data for the simulations' inputs, and the studies of imperfections of the WAAM tube. One thing should be noticed is that the specific printing process parameters were removed from Van Bolderen's thesis due to the request from MX3D.

3.1.1 Printing material - 308LSi

From Van Bolderen's lab test, stainless steel Oerlikon's 308LSi (Appendix.A.1) has been used in the compression test, the bending test, and the buckling test. As for the tensile test, the material used is Ugiveld 308LM stainless steel. The reason is that the tensile test is performed by a company called OCAS. Nonetheless, two materials comply with the same standard of strength for welding use from the datasheet provided.

The austenitic stainless steel has 300 series and 200 series. The 308, 308L, 308LSi, 316L all belong to the 300 series and are austenitic alloys. The difference between 308 and 308L is that 308L has a lower carbon percentage (max. 0.03%) than 308 (0.08%). Although lower carbon percentage leads to slightly lower yield strength, it is more suitable for welding. The other more advanced type of base material is 316L. In addition to more chromium and nickel, this type of alloy contains molybdenum (Mo, 2 to 3%), which has higher yield strength and more corrosion resistance at room temperature.

The 308L material is used for printing instead of 316L because it is up to 40% cheaper than 316L. Nevertheless, the durability of 308L is sufficient in the urban area [1]. The prescribed Si in 308LSi means extra silicon (0.4% extra) is added to enhance the oxidation resistance [1] (Table.3.1).

Table 3.1: General composition and mechanical properties for 308, 308L, 316L and 308LSi stainless steel

Chemical composition										Mechanical properties	
Chemical element (weight %)	C	Mn	Si	P	S	Cr	Mo	Ni	Fe	Tensile Strength (MPa)	Yield Strength (MPa)
308 L	0.02	1.8	0.45	≤ 0.025	≤ 0.02	20	0.2	10	5 – 10	≤ 520	≤ 350
316 L	0.02	1.4	0.45	≤ 0.025	≤ 0.02	19	2.6	12.5	5 – 10	≤ 510	≤ 350
308LSi	0.02	1.8	0.85	≤ 0.025	≤ 0.02	20	0.2	10	5 – 10	≤ 520	≤ 350

3.1.2 The Ramberg Osgood and Rasmussen approximation

Unlike carbon steels, which use the bi-linear stress-strain curve for the design, the Ramberg-Osgood curve (Eq.3.1) are often used for identifying stainless steel's behavior. The mathematical formula uses the parameter n to find the most fitting curve for materials stress-strain curve's. Since the Ramberg-Osgood equation appears to have significant errors for austenitic stainless steel after the strain exceeds 0.2%, researches have been conducted to modify the error. Rasmussen achieved to use the same parameters from Ramberg-Osgood equation ($E_0, \sigma_{0.2}, n$) to modify the curve after $\sigma_{0.2}$ (Eq.3.2) [1] [50].

$$\varepsilon = \frac{\sigma}{E_0} + 0.002 \left(\frac{\sigma}{\sigma_{0.2}} \right)^n \quad \text{for } \sigma \leq \sigma_{0.2} \quad (3.1)$$

$$\varepsilon = \frac{\sigma - \sigma_{0.2}}{E_{0.2}} + \varepsilon_u \left(\frac{\sigma - \sigma_{0.2}}{\sigma_u - \sigma_{0.2}} \right)^m + \varepsilon_{0.2} \quad \text{for } \sigma > \sigma_{0.2} \quad (3.2)$$

The $\sigma_{0.2}$ is the 0.2% proof stress often used in the industry practice for designing stainless steel [50] and σ_u is the ultimate stress. E_0 is the Young's modulus of the material, and $E_{0.2}$ represent the tangent modulus of the stress-strain curve at the $\sigma_{0.2}$ and it is defined in Eq.3.3. The ultimate strain ε_u can be approximated by using the Eq.3.4, and $\varepsilon_{0.2}$ is the strain at the point where $\sigma_{0.2}$ has reached. It has to be aware that $\varepsilon_{0.2} \neq \varepsilon = 0.2\%$ and can be acquired from Eq.3.5.

$$E_{0.2} = \frac{E_0}{1 + 0.002n \frac{E_0}{\sigma_{0.2}}} \quad (3.3)$$

$$\varepsilon_u = 1 - \frac{\sigma_{0.2}}{\sigma_u} \quad (3.4)$$

$$\varepsilon_{0.2} = \frac{\sigma_{0.2}}{E_0} + 0.002 \quad (3.5)$$

Two non-linear parameters for the Ramberg Osgood and Rasmussen approximation are n and m . The parameter n can be derived from Eq.3.6 and m can be derived from Eq.3.7.

$$n = \frac{\ln(20)}{\ln \left(\frac{\sigma_{0.2}}{\sigma_{0.01}} \right)} \quad (3.6)$$

$$m = 1 + 3.5 \frac{\sigma_{0.2}}{\sigma_u} \quad (3.7)$$

The research of WAAM tubular components [1] show the mean non-linear parameters in the longitudinal direction are $n=16$ and $m=1.7$, and the parameters in the transversal direction are $n=14$ and $m=1.6$

(Table.3.2) [1]. The material properties (the engineering stress-strain curves) and material input for the simulation (the true stress-strain curve) have been plotted and converted in Section.4.1.3 according to these value.

Table 3.2: Non-linear parameters for WAAM printed specimen [1]

	Non-linearity Parameter	Specimen (1)	Specimen (2)	Specimen (3)	Mean	St. dev. σ
Longitudinal	Ramberg Osgood n [-]	14	16	18	16.0	1.6
	Rasmussen m [-]	1.81	1.60	1.69	1.70	0.09
Transversal	Ramberg Osgood n [-]	12	14	16	14.0	1.6
	Rasmussen m [-]	1.79	1.60	1.41	1.60	0.16

3.1.3 Conversion of engineering stress-strain curve to true stress-strain curve

Tensile stress-strain curve conversion

For tensile coupon test, before inputting the material non-linearity from the experiment, the engineering stress-strain curve should be converted to the true stress-strain curve. This conversion considers the material's response in the change of cross-sectional area throughout the experiment. The conversion formulas are as followed. Eq. 3.8 shows how the engineering strain can be converted to true strain in the tensile stress-strain curve. Eq. 3.9. shows how the engineering stress can be converted to true stress in the tensile stress-strain curve.

$$\varepsilon_T = \text{Ln}(1 + \varepsilon_E) \quad (3.8)$$

$$\sigma_T = \frac{P}{A} = \frac{P}{A_0} \cdot \frac{L}{L_0} = \sigma_E (1 + \varepsilon_E) \quad (3.9)$$

The conversion holds true when specimens have no volume change [51]. Also, the equations are valid up to the ultimate tensile stress (UTS) point, where the strain at which necking begins [52]. Therefore, the use of this conversion after the necking is prohibited since the strain is nonuniform in the gauge length after the necking (conversion validity shown in Fig. 3.1).

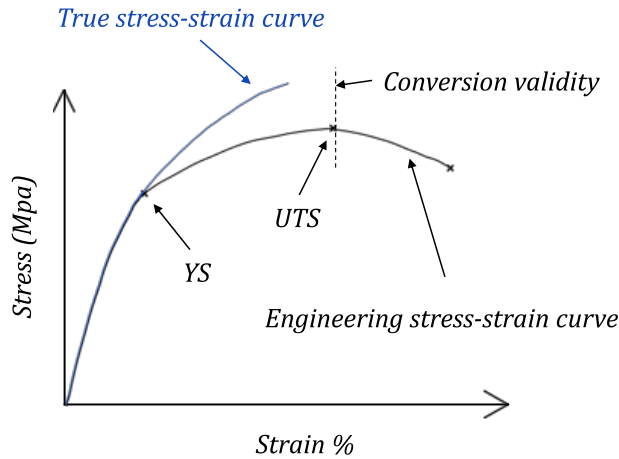


Figure 3.1: Engineering and True tensile stress-strain curves conversion validity

3.1.4 Imperfections of circular WAAM product

To print large structural components, the large deposition of material and high inputs of heat in WAAM process caused several printing inaccuracies.

WAAM imperfections (geometrically and materially) are presented in this Section. Besides Van Bolderen's research [1], Laghi et al [53] also provides detailed research of continuous WAAM printed circular members. The experimental result from Van Bolderen is the main focus for the simulation in Ch.4. The research from Laghi is also added in this review section as an extra reference. All related information are presented and discussed in this subsection.

Geometrical imperfections

Three main geometrical imperfections observed from the WAAM columns are out of roundness (or cross-sectional irregularities), lack of straightness, and surface roughness [53] (see Fig.3.2).

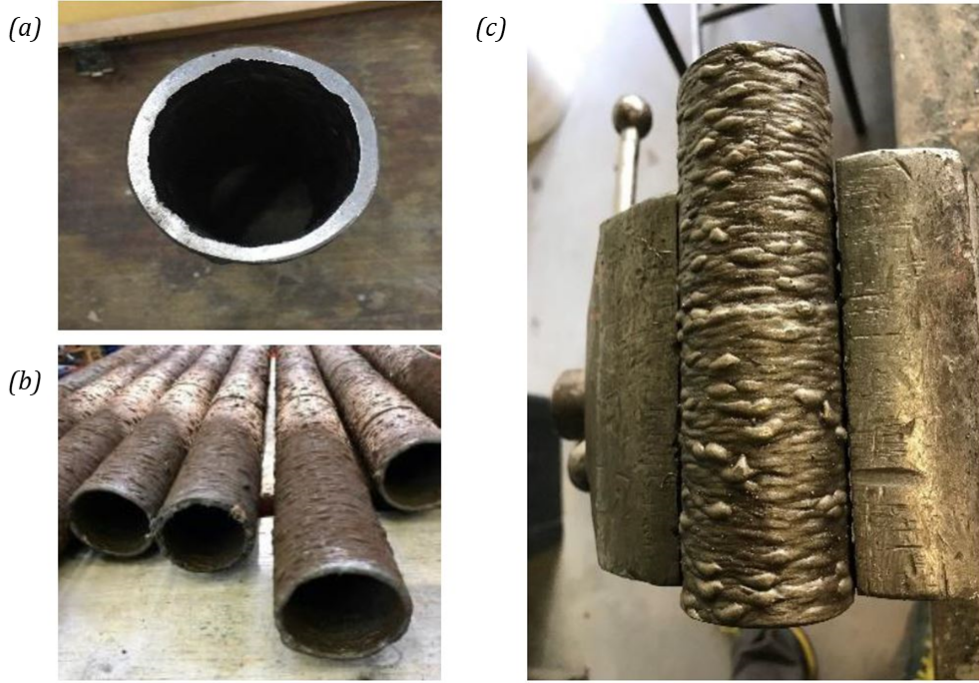


Figure 3.2: Geometrical imperfections observed from the WAAM columns [53]. (a) Out of roundness (Cross-sectional irregularities), (b) Lack of straightness, and (c) surface roughness.

Out of roundness (Cross-sectional irregularities)

The thesis from Van Bolderen does not perform the out of roundness measurement. As for Laghi, the out of roundness investigation was carried out with 40 3D scanned cross-sections of one printed tube (nominal diameter: 55mm, nominal thickness: 5mm, and nominal length: 850mm).

The out of roundness was computed by using the $O(\%)$ in Eq.3.10. D_n means the nominal diameter of the tube's cross-section, D_1 and D_2 represent the outer diameter of the real WAAM tube (shown in Fig.3.3). The mean value of the $O(\%)$ is 1.31%, and the maximum value is 3.2%. The standard for out of roundness tolerance for cold-form tubes is 2% according to EN 10219-2, and the maximum tolerance for tubular members in ISO 19902 of fixed offshore steel structure is 3% [53].

$$O(\%) = \frac{|D_2 - D_1|}{D_n} \cdot 100 \quad (3.10)$$

Lack of straightness

Lack of straightness is the eccentricity from the nominal center axis (Fig. 3.3 (a) and (b)). It is expressed by the ratio of eccentricity over the tube length. The average lack of straightness of three continuous tubes from Van Bolderen's thesis is $L/791$, with a standard deviation of $L/32$ [1]. As a reference, from Laghi's thesis, forty 3D scanned cross-sections of one printed tube (nominal diameter: 55mm, nominal thickness: 5mm, and nominal length: 850mm) were measured and the lack of straightness is around

$L/1000$, with the maximum value at around $L/300$ [53]. The straightness tolerance of conventional cold form welded tubular members is $L/500$ according to EN10219-2.

Surface roughness The surface roughness is namely the uneven surface on the printed objectives. The roughness evenness largely depends on the welding process and parameters; higher disposition rate causes larger surface roughness. The surface roughness cause the varying of cross-sectional area and thicknesses.

In Van Bolderen's thesis, the effective thickness (t_{eff}) is derived from the lab experiments to account for the influence of surface roughness on the WAAM members. The derivation is shown in 3.4.2. Laghi's research has provided 3D scanning data with 40 cross-sections from one printed tube (nominal diameter: $55mm$, nominal thickness: $5mm$, and nominal length: $850mm$). Each cross-section was measured with their four angles $\theta = 0^\circ, 90^\circ, 180^\circ$, and 360° (see Fig.3.3(d)). The nominal radius is $27.5mm$ and the average radius measured in four angles in 40 section is $26.74mm$ (relative error of 2.7%) [53].

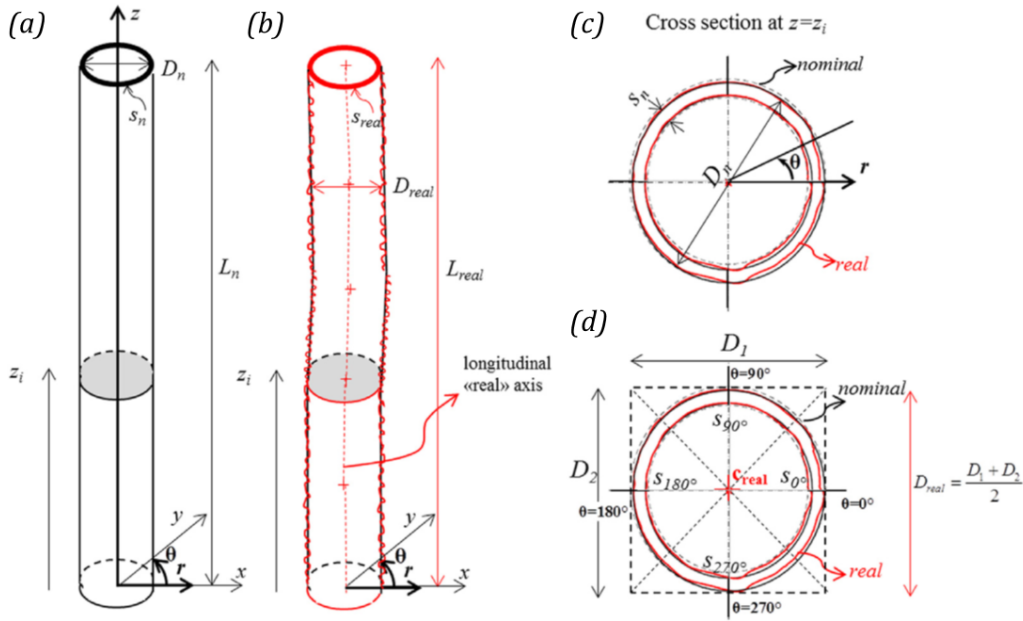


Figure 3.3: Geometrical imperfections explained in sketch. (a) Nominal tube. (b) WAAM printed tube. (c) Cross-section along nominal and WAAM printed tube. (d) The WAAM printed tube cross-section's measuring parameters [53].

Material imperfections

The continuously WAAM printed specimens have anisotropic mechanical behavior.

Anisotropic behavior

Microstructural studies of the printed specimens from Van Bolderen's research are provided below.

The thermal gradient of the weld pool and the combination of mechanics of weld solidification lead to the formation of large columnar grains, which form cross-bead grains along the horizontal successive printed layers. (see Fig.3.4 (a)).

The longitudinal metallographic section (see Fig.3.4 (b)) shows a more homogeneous material behavior.

To include the anisotropic mechanical behavior in the simulation in Ch4, the WAAM printed material is considered orthotropic. Young's modulus is built from the longitudinal and transverse direction in Section.4.1.4.

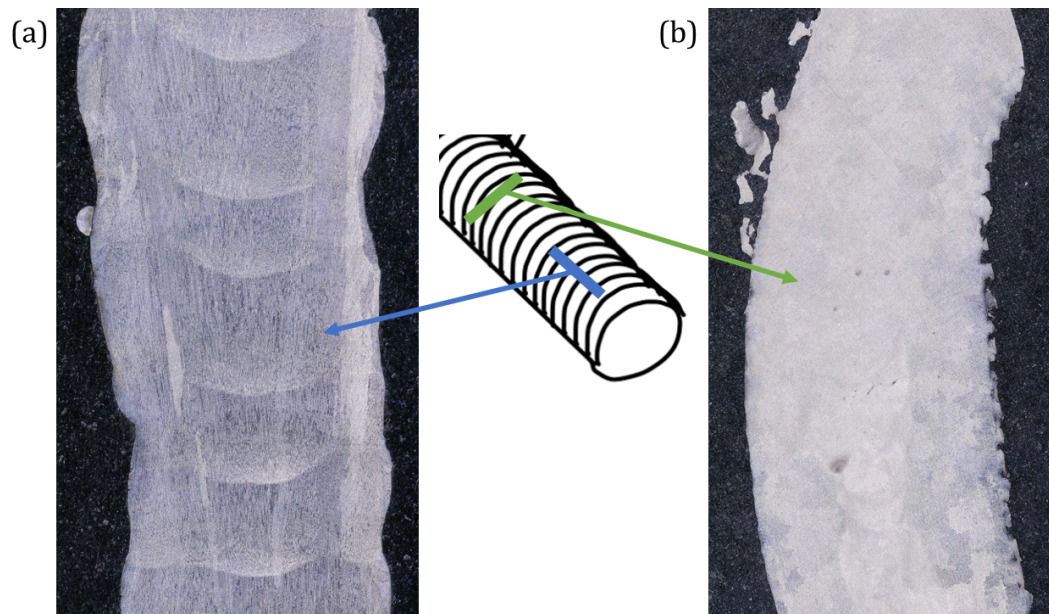


Figure 3.4: Longitudinal and transverse grain observations under a microscope. (a) Transverse direction, (b) Longitudinal direction [1].

3.2 Tensile test

This lab test aims to get the tensile stress-strain curve from both transverse and longitudinal printing directions. From the stress-strain curve, Yield strength (YS) (0.2% proof stress), Ultimate tensile strength (UTS), Young's modulus (E), Ultimate strain, and Fracture strain can be acquired.

3.2.1 Tensile test setup

Tensile test coupons were printed in two directions, transverse and longitudinal (see Fig.3.5). A total of six continuous printing specimens were tested (three for each printing direction). They were all extracted out from WAAMed thin printed wall (Fig.3.6) and milled to the dimension according to ISO 6892-1 (see Fig.3.5). Tensile coupons are clamped on two side (faces) and pulled by tensile test machine (see Fig.3.8). The forces and strain were recorded to plot Engineering stress-strain curve.

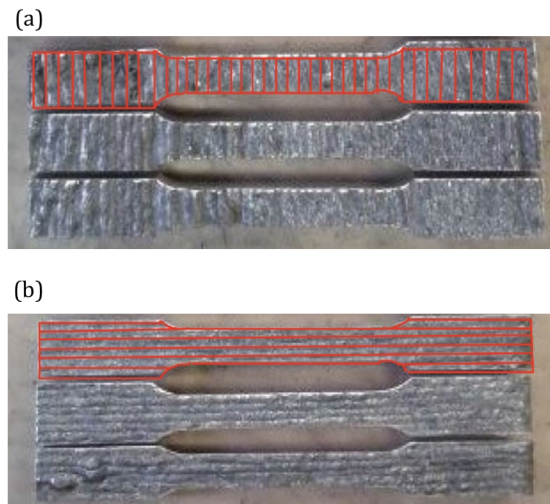


Figure 3.5: Tensile test material printed direction (milled). (a) Transverse printing direction, (b) Longitudinal printing direction.

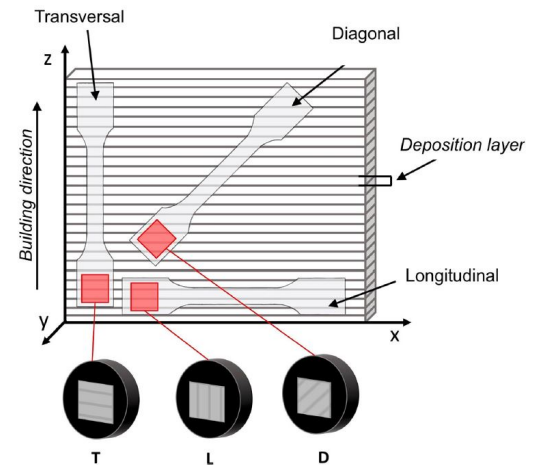


Figure 3.6: Ideas of tensile coupon cut out from thin WAAMed wall. T-Transverse direction; L-Longitudinal direction; D-diagonal direction (Not included in the reviewed lab test) [42].

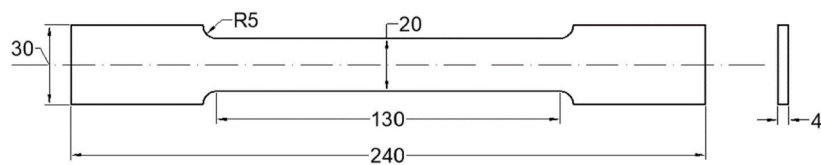


Figure 3.7: Tensile test specimen dimension according to ISO 6892-1 [42].



Figure 3.8: Tensile test setup (machine: Zwick/Roell Z250).

3.2.2 Tensile test result

Stress-strain curves from the six continuous printed coupons in transverse and longitudinal printed direction are shown in Appendix.A.2 and Appendix.A.3. It has to be aware that the curves are from the Ramberg Osgood and Rasmussen approximation (see Section.3.1.2), which means that the curves are made to be able to describe in mathematical formula and retain very close value with real test value.

The lab test finds the average Young's modulus in transverse direction ($E_{Transverse}$) = 121GPa and the average Young's modulus in longitudinal direction ($E_{Longitudinal}$) = 137GPa.

The result shows a rather low Young's modulus (E) compared to the material reference of steel in Eurocode 3 (reference value E_0 = 200GPa).

Table 3.3: Tensile test result.

	0.2% Proof Stress $\sigma_{0.2}$ [N/mm ²]	Ult. Tensile Strength σ_u [N/mm ²]	Young's Modulus E_0 [GPa]	Ultimate Strain ϵ_u [%]	Fracture Strain ϵ_f [%]
<i>Oerlikon - as welded 20°C</i>	>350	>520	-	>35	
<i>Ugiweld - as welded 20°C</i>	360	600	-	>35	
Longitudinal (print dir.)	307	544	137	21.2	22.0
<i>St. deviation σ</i>	5	28	6	3.5	3.8
Transversal	321	568	121	30.9	34.9
<i>St. deviation σ</i>	6	11	6	0.9	4.7

3.3 Compression test

The aim of the compression test is to get the Yield strength (YS) and Young's modulus (E) from the experiment.

3.3.1 Compression test setup

The compression test specimen were cut and milled in and out (see Fig.3.10). The milled sample has the thickness (t) = 2 mm, length (L) = 50mm, Moment of inertia (I) = 19444.8 mm⁴, and the sectional area (A) before compression is 182.8 mm² (see Fig.3.11). The sample was installed in the displacement-controlled test machine with steel plate bearings on two ends. In this test no strain gauges are used, only the displacement of the machine has been measured.



Figure 3.9: Compression test setup.



Figure 3.10: The compression test specimen.

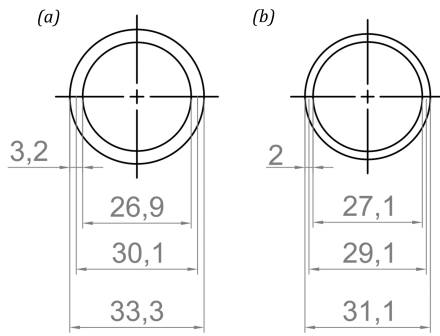


Figure 3.11: Specimens cross-sectional sizes. (a) Nominal cross-sectional sizes (use in the bending and the buckling test). (b) Milled sample's cross-sectional sizes (use in compression test). (unit: *mm*)

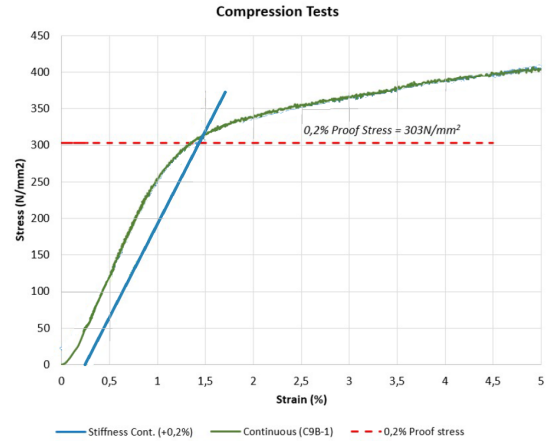


Figure 3.12: The compression stress-strain curve from lab test. [Adapted]

3.3.2 Compression test result

From the stress-strain relations of the continuous specimen, it shows the Yield strength (YS) (or being called as 0.2% proof stress) is 303N/mm^2 , and the compression resistance equals to 57KN (Fig.3.12).

Because of the lack of time and the budget limit for milling all the specimens, only one lab test data is provided.

The deformations of the specimen measured are higher than expected. From the observation, the compression sample was pressed into the bearing plates and left clear marks, which are results from the force concentration of high loads. To minimize the problem from strain measurement, strain gauges could be applied to the sample to get precise strain measurement. For convenience, the displacement in this lab test only measures directly from the machine displacement. Therefore, the Yield strength (YS) and Young's modulus (E) is provided by the tensile lab test.

For similar (hollow tube specimens with similar diameter:thickness ratio, both around 10:1 in Van Bolderen and Laghi's experiment) WAAM steel circular product of material 308 series, the use of elastic behavior in compression test is similar to the tensile test has been verified by Laghi (Ultimate stress are different due to possible buckling failure.) [53].

3.4 Bending test

The aim of the Four points bending test is to get the elastic bending stiffness (EI) in order to derive the effective thickness (t) from Moment of inertia (I) with the known value of Young's modulus (E) from the tensile test.

3.4.1 Bending test setup

Three continuous tubes with 650mm in length are performed in Four-points bending test, the nominal cross-section sizes is shown in Fig.3.12(a).

For the setup, both sides of the tube were laid on steel supports with lateral timber confinements (Fig.3.14). A hydraulic steel frame is being used to apply 2 load points at the tube (Fig. 3.15). Since tubes will be reused in the buckling test, total loads are set to $P=3\text{KN}$ to keep the tube bent in the elastic range. More detailed setup dimensions are shown in the test scheme in Fig.3.16. The displacements at the center were laser measured at the bottom face of the white box (Fig.3.13), which is created for measurement, at the middle length of the tube. Four sides of the deflection have been measured, therefore, after each measurement, the tube will be rotate in 90 degrees.

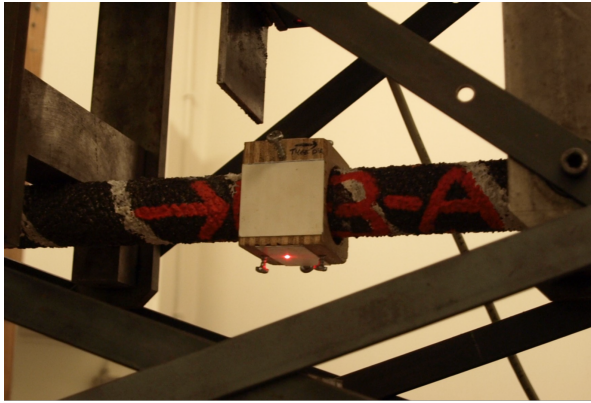


Figure 3.13: Laser deflection measuring at the bottom of the timber box, which is installed at the middle of tube.

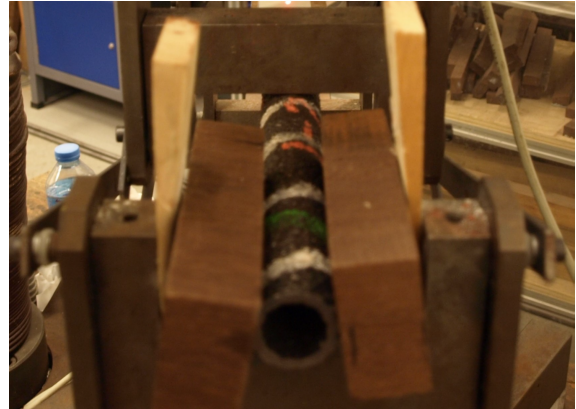


Figure 3.14: A side view of the experimental setup.

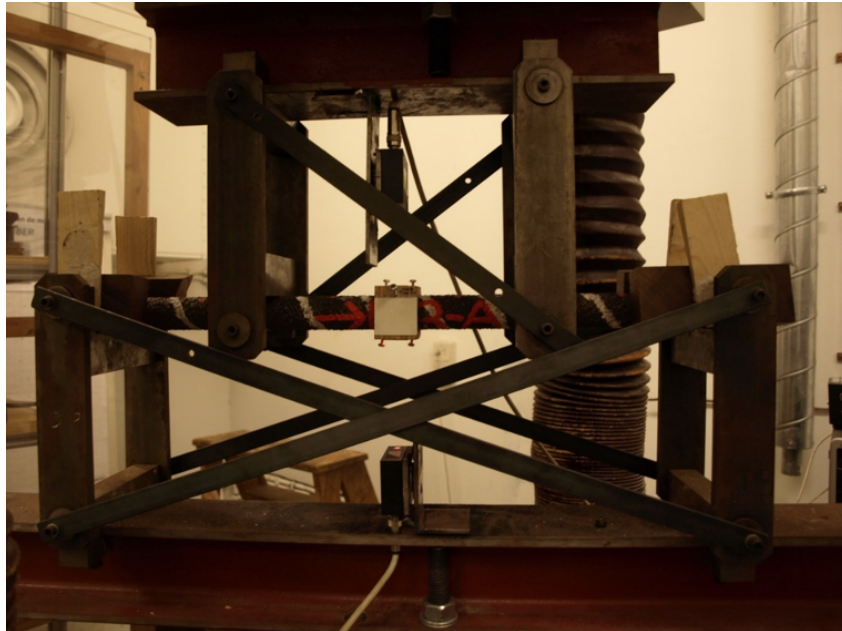


Figure 3.15: Four points bending test setup.

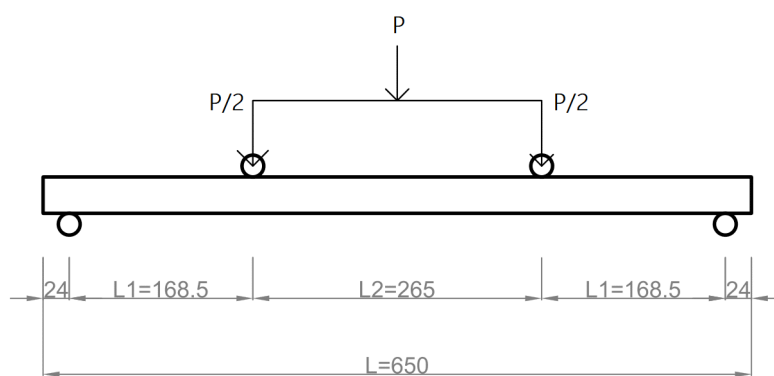


Figure 3.16: Four points bending test scheme (unit: mm , $P=3KN$).

3.4.2 Bending test result

The Four points bending test aim is to get the elastic bending stiffness (EI). The output of the test is the load-displacement curve. The deflection at the mid-span $w\left(\frac{L}{2}\right)$ can be given from Eq.3.11. The parameters L, L_1 , and P can be seen in Fig3.16.

$$w\left(\frac{L}{2}\right) = \frac{PL^2L_1\left(3 - 4\frac{L_1^2}{L^2}\right)}{48EI} \quad (3.11)$$

Since the deflection can be obtained from the experiment, the bending stiffness (EI) can be acquired from the formula in the other form (see Eq.3.12) .

$$EI = \frac{P}{w\left(\frac{L}{2}\right)} \frac{L^2L_1\left(3 - 4\frac{L_1^2}{L^2}\right)}{48} \quad (3.12)$$

From the result, the average elastic bending stiffness (EI) from four sides of the WAAM tube is $3.96 \cdot 10^9 \text{ Nmm}^2$ (see Table. 3.4), which is 43% less than the bending stiffness $EI = 6.93 \cdot 10^9 \text{ Nmm}^2$ of the austenitic steels material (one type of stainless steel). The reasons for different bending stiffness measured from the experiments could be: the geometrical imperfections of the WAAM printed tubes, the anisotropy of the printed material, and the errors coming from the placing of the tube and measuring of the deflections.

Two occasions might cause the low bending stiffness (EI). The first is the anisotropy of the material that caused Young's modulus (E) lower than the original material property. The second is that the surface roughness could lead to thicker or thinner thickness than expected. In order to estimate the effect of surface roughness, the effective thickness t_{eff} has been derived.

The Young's modulus in the transverse direction ($E_{transverse}$) is being used as Young's modulus in the calculation. Then the effective moment of inertia (I_{eff}) can be known by dividing the experimental EI with $E_{transverse}$. After acquiring the effective moment of inertia (I_{eff}), the t_{eff} is then being found. The end result shows the thickness has been reduced from $t=3.2\text{mm}$ to $t_{eff}=3.01\text{mm}$, which is a 5.9% reduction.

Table 3.4: Results of Bending stiffness from the Four points bending test.

Specimen/Side	Bending Stiffness EI [Nmm ²]				Mean	St.dev. σ (%)
	Side 1	Side 2	Side 3	Side 4		
B-1-B	$3.98 \cdot 10^9$	$3.94 \cdot 10^9$	$3.89 \cdot 10^9$	$4.00 \cdot 10^9$	$3.95 \cdot 10^9$	1.08
B-2-B	$4.00 \cdot 10^9$	$3.95 \cdot 10^9$	$4.03 \cdot 10^9$	$3.94 \cdot 10^9$	$3.98 \cdot 10^9$	0.93
B-3-B	$4.01 \cdot 10^9$	$3.87 \cdot 10^9$	$4.08 \cdot 10^9$	$3.82 \cdot 10^9$	$3.94 \cdot 10^9$	2.73
Mean					$3.96 \cdot 10^9$	
St.deviation σ (%)					0.39	

3.5 Buckling test

Flexural buckling with several slenderness ratios are performed in the lab test to acquire the buckling length. However, for continuous printed tubes, only one slenderness is presented. Therefore, the review and the numerical simulation will solely focus on simulating the only dimensions of the WAAM tube and compare the critical load values with it.

3.5.1 Buckling test setup

Three continuous WAAM tubes, the same tubes that performed the bending test, are reused in the buckling test. The bending test was performed in the elastic range. Therefore, tubes are considered to

be intact. The length of the tubes are 650mm , and the nominal cross-sectional area is shown in Fig.3.12 (a).

For the setup, tubes are hinged at both sides and being placed on a hydraulic jack (Fig.3.17 (a)). The ball bearing (model type: GE30AW) is used to simulate the effect of hinged connection (shown in Fig.3.17 (c)). To prevent the ball hinge from pushing into the column and make the tube end expand, a bolt is installed at the end of the tube (Fig.3.17 (b)).

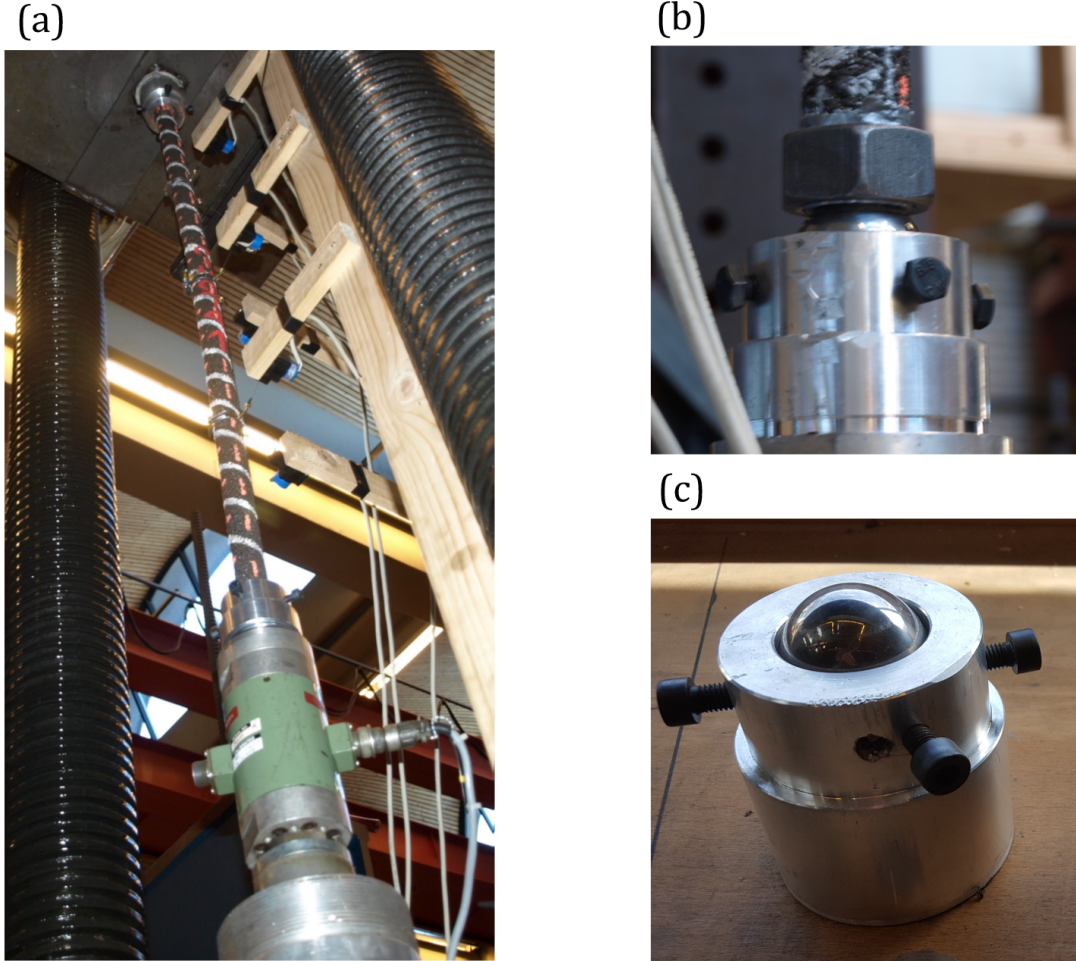


Figure 3.17: Buckling test setup. (a). The WAAM printed tube on a pressure jack, (b). Bolt at the tube end for strengthening purpose, (c). The ball bearing installed at the tube ends.

The original buckling length $L_{buc,ori}$ is equal to the center to the center of the ball bearings. However, ball bearings show signs of friction acting in the system. Therefore, several cold-drawn thick-walled steel tubes were added in the experiment to correct the original buckling length $L_{buc,ori}$ with the finding of new K value (K_{eff}). Therefore, the effective buckling length $L_{eff} = K_{eff} \cdot L_{buc,ori}$.

3.5.2 Buckling test result

Euler column theory (Eq.3.13) is used to describe the critical load (N_{cr}) of the column that is slender enough to fail before any points in the object has reached the elastic limit. The column is considered ideally straight, centric loaded, and pinned at both ends.

$$N_{cr} = \frac{\pi^2 EI}{L_{cr}} \quad (3.13)$$

The influence of the constraints at both sides of the column influence the buckling load (F_{buc}) (Eq.3.14). The effect of the constraints can be described as the effective length factor (K) in the formula. The

original length between two pinned support at two ends of the column is L , and the effective length (L_{cr}) = $K \cdot L$.

$$F_{buc} = \frac{\pi^2 EI}{KL} \quad (3.14)$$

The buckling load proposed in this section is based on the lab experiment. The mean buckling load F_{buc} is 52.74KN (Table.3.5). Both Young's modulus (E) and Moment of inertia (I) are from the tensile test results and the effective thickness.

The new effective buckling length was found while new K value ($K_{eff} = 0.72$) has been derived from buckling tests of cold-drawn thick-walled steel tubes, in which the mechanical and geometrical characteristics are known.

The geometrical imperfection of the continuous WAAM printing tube can be found from the initial curvature measurements in Table.3.6. Only the specimen type B-X-B is the continuous WAAM printing tube, which is targeted as this thesis's samples, and only the hand measurements have been done (the others are dot-by-dot printed tubes, which are not the targeted samples in this thesis). The average lack of straightness (e_0) = $L/791$. However, this imperfection will not be modeled in the geometry of the buckling test simulation in Ch4. For the inclusion of lack of straightness, the shape found from LBA is used (see Section. 4.1.4 for more information).

Table 3.5: Buckling test result for continuous printed columns.

Specimen	Buckling Length L_{eff} [mm]	Eff. Buckling length L_{eff} [mm]	Buckling load F_{buc} [kN]
B-1-B	687	495	52.38
B-2-B	691	498	51.97
B-3-B	691	498	53.87

$K=1$ $K_{eff}=0.72$ K correction from Cold-drawn thick-walled steel tubes.

avg $L_{eff} = 497\text{mm}$ avg $F_{buc} = 52.7\text{KN}$

Table 3.6: Initial curvature measurement from hand and 3D-scan of WAAM printed tubes.

Specimen	Hand Measurements		3D-Scans	
	e_0	St.dev. σ (%)	e_0	St.dev. σ (%)
A-125-X	L/593	L/25	L/588	L/12
A-85-X	L/604	L/97	L/623	L/19
B-X-A	L/707	L/43	L/688	L/7
B-X-B	L/791	L/32	-	-
Average	L/674	L/49	L633	L/13

3.6 Conclusions

This sections provides the answer to the following questions.

Research questions in this chapter are:

- 1) What are the imperfections of WAAM components in the review of lab tests?
- 2) What is the setup for each mechanical test?
- 3) What lab test results are presented in each of the mechanical tests and are being used in numerical simulations in Ch4?

Imperfections of WAAM components

In general, the material of WAAM is anisotropic and is considered as a material imperfection.

In WAAM printed hollow circular tubes, three main types of geometrical imperfections have been observed from the WAAM columns, which are out of roundness (or cross-sectional irregularities), lack of straightness, and surface roughness [53]. More details can be seen in Sec.3.1.4.

Setup for each mechanical test

Each lab test setup has been studied in this chapter to get a better picture of building FEA models and realize their boundary conditions. Detailed information is presented in each of the setup sections for each lab test.

Lab test results provided by each mechanical test

The following summarized results from the lab tests have been implemented in the numerical simulations in Ch4.

Tensile test

Six milled coupons (three from transverse printed direction and three from longitudinal printed direction) are provided.

In the transverse direction, the average Young's modulus ($E_{Transverse}$) is 121GPa, the average yield stress is 321MPa, and the average ultimate tensile strength is 568MPa.

In the longitudinal printed direction, the average Young's modulus ($E_{Longitudinal}$) = 137GPa, the average yield stress is 307MPa, and the average ultimate tensile strength is 544MPa.

The material non-linearity data is derived from the Ramberg Osgood and Rasmussen approximation formulas in Section.3.1.2 with the n, m value provided from the tensile test lab experiment results in Section.3.2.2. The curves are plotted in sec.4.1.3 for the numerical simulation preparation.

Compression test

Only one milled sample is provided and performed in the lab test.

From the stress-strain relations of the continuous specimen, the Yield strength (YS) is $303N/mm^2$, and the compression resistance equals to $57KN$.

Bending test

Three samples were used to test the bending stiffness.

The average bending stiffness is $EI = 6.93 \cdot 10^9 Nmm^2$ and the average deflection at the mid-span, which is $2.589mm$ can be calculated from Eq.3.11.

The effective thickness for incorporating surface roughness has lead to the thickness reduction from $t=3.2mm$ to $t_{eff}=3.01mm$.

Buckling test

Three printed tubes were taken to perform the buckling lab test.

The average buckling load is $52.7KN$, the average effective buckling length is 497mm, and the average hand-measured lack of straightness of the tube is $L/791$.

Chapter 4

Numerical simulation of four WAAM mechanical tests

It is crucial to examine parameters, settings, material non-linearity data, and introduced imperfections numerically in this simulation chapter to ensure the validity before it has been used for the joint strength prediction in Ch.5.

The main goals of this chapter are:

- Verify the parameters and material data from the components' lab test.
- Introducing imperfections observed from WAAM components to the analysis and discuss the suitability of the use of defined parameters.

To fulfill this chapter's goal, actions using the shell analysis method and FEA software to simulate the lab experiments will be taken numerically.

Research questions in this chapter are:

- 1) Do simulation results show the numerical simulation reliable?
- 2) How can the precision of simulations be improved? What parameters are lacking for performing the simulations?
- 3) What imperfections are included? And how can the imperfections be used to design the joint further and predict its strength?

In this chapter, simulation preparation, including the method of introducing the material imperfection and geometrical imperfections from the WAAM lab test and observations to FEA, is shown in Section.4.1. The first simulation, which is the tensile test, is shown in Section.4.2. The second simulation is the compression test simulation, which is provided in Section.4.3. The third simulation is the bending test in Section.4.4. The last simulation is the buckling test simulations in Section.4.5. In each lab test simulation, the simulation settings, process, results, analysis, and conclusions for four lab test simulations are provided. The conclusion for the whole numerical simulation is provided in Section.4.6.

4.1 Simulation preparations

This section transforms the knowledge and the data from literature reviews to ideas and assumptions for numerical analyses, including:

- The plan out of the shell analysis procedure and its link to the imperfection factors considered in the simulations (Section.4.1.2);
- The material non-linearity inputs for the simulations (Section.4.1.3);
- The introduction of WAAM tubes' geometrical imperfection and material imperfections to the FEA models (Section.4.1.4);

4.1.1 Finite Element Analysis software - ABAQUS

ABAQUS has been used for Finite Element Analysis for both linear and non-linear stress analysis. It has an automatic and adaptive ability of time incrementation for computation. The benefit is that it could compute efficiently and give uniform accuracy throughout the simulation time history [54]. Also, ABAQUS has been widely used in academic research and industries, making it more convincing to use as this thesis's numerical calculation method.

4.1.2 Factors and types of analysis considered for simulation and strength analysis

For conducting lab simulation (Ch4) and joint strength analysis (Ch5), different types of analysis for shells with different combinations of the factors are taken into account. The relations of considered factors and types of shell analysis are shown in Fig.4.1 as the suggestions for developing FEA models for components' lab test simulations. Three crucial aspects are the Linearity of the analysis, Geometrical imperfections, and Material imperfections (Orthotropicity). More details regards to types of shell analysis and inclusion of imperfections to the model can be found in Section.2.2 and Section.3.1.4.

The relevant analysis type for each lab test simulation will be used and mentioned in each simulation section.

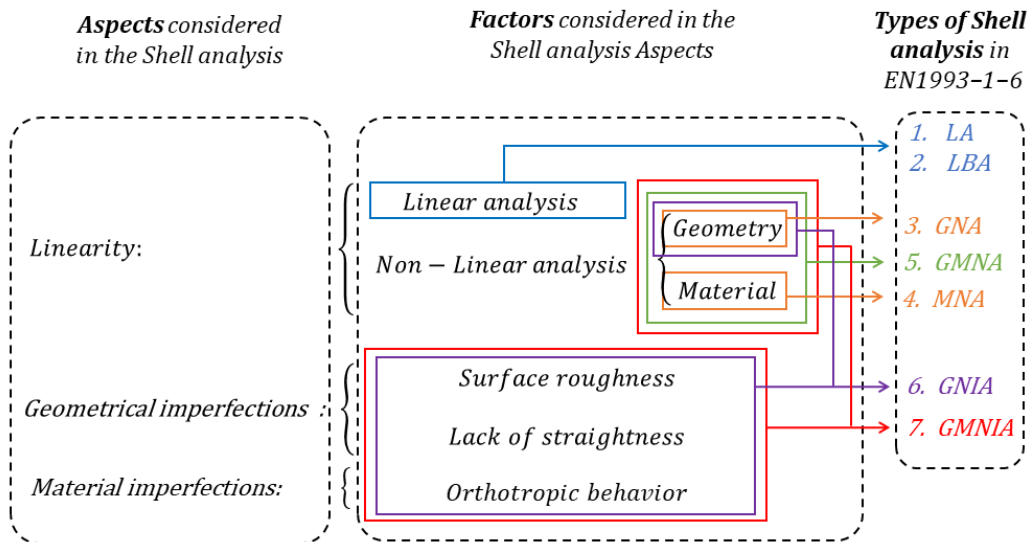


Figure 4.1: Factors and their relations to different types of shell analysis.

4.1.3 Material non-linear input - The true stress-strain curve

The engineering stress-strain curve (in blue) shown in Fig.4.2. is derived from the formulas in Section.3.1.2 with the n, m value provided from the tensile test lab experiment results in Section.3.2.2

For the material non-linearity input in the simulation, the true stress-strain curve should be used as the input instead of the Engineering stress-strain curve. The Engineering tensile test stress-strain curve were convert to true tensile test stress-strain curve (in orange) shown in Fig.4.2. The theory behind the conversion is mentioned in Section 3.1.3.

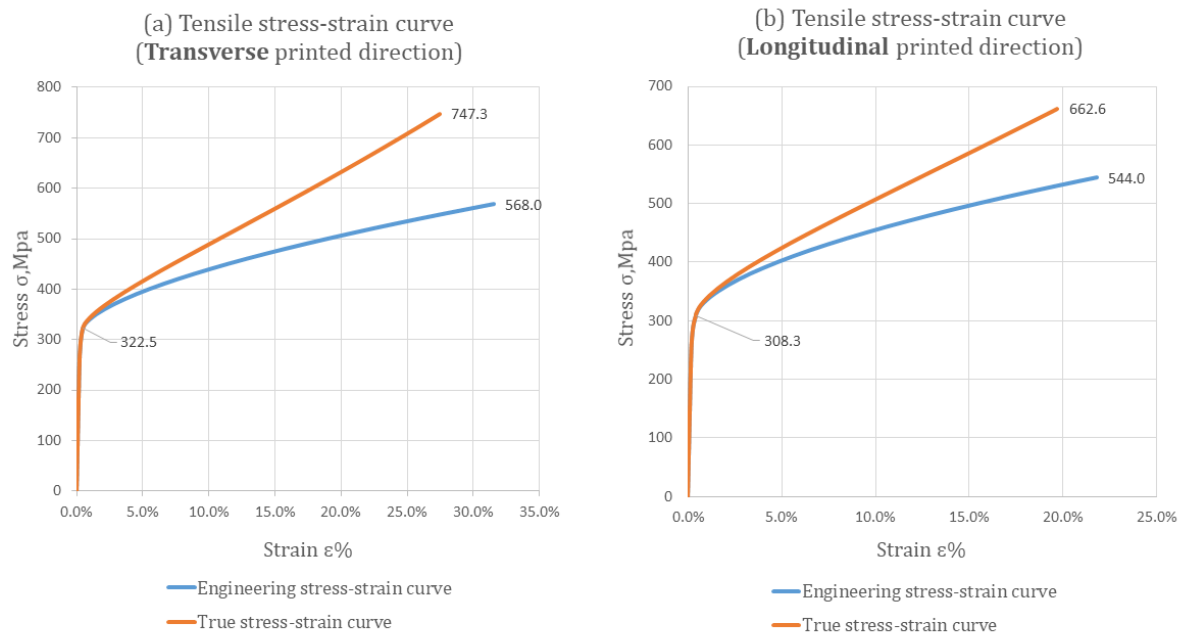


Figure 4.2: Engineering and True tensile stress-strain curves. (a) Transverse printed direction, and (b) Longitudinal printed direction.

4.1.4 Introducing WAAM imperfections in numerical simulations

Methods for accounting WAAM imperfections for simulations are discussed in this section.

Geometrical imperfections

Three types of geometrical imperfections are discussed in the literature review of continuous WAAM printed tubes in Section.3.1.4. The action for incorporating the imperfections in the numerical simulation are listed below and relevant figures for better understanding can be seen in Fig.4.3.

Out of roundness

The thesis from Van Bolderen does not perform the out of roundness measurement. As a reference, the studies from Langhi in Section.3.1.4 shows that the out of roundness behavior of 40 WAAM printed samples has the mean value of $O(\%) = 1.31\%$ and the maximum value of $O(\%) = 3.2\%$. The tolerance for the production of cold-form tubes according to EN 10219-2 is (2%), and the maximum tolerance of fixed offshore steel structure is (3%). Since the out of roundness is negligible enough to be accepted by relevant code, it is not considered in the simulation.

Lack of straightness

Lack of straightness influence the strength of a structure, typically for slender structures. Both the bending test and the buckling test use slender tubes as samples. However, only the lack of straightness in the buckling test (Section.4.5) is considered.

The reason is that the bending test performs the experiment with four sides of the beam (turn 90 degrees for the next measurement), and the average value taken ruled out the lack of straightness from the bending test.

The buckling test includes the lack of straightness of $L/791$ by using the scale factor to adjust deviations from the center axis of the model, which is found from the possible shape (mode) found from the linear buckling analysis (LBA). Instead of modeling it directly onto the model.

To be more specific, both the LBA shape found and the original lack of straightness imperfection has the same "Bow-like" failure shape. Therefore, the numerical simulation use certain scale factor to match the original lack of straightness ($L/791$) of the tube.

Surface roughness

The Surface roughness is considered by using the deduced thickness (effective thickness, t_{eff}) from Van Bolderen's method, which is derived in Section.3.4.2.

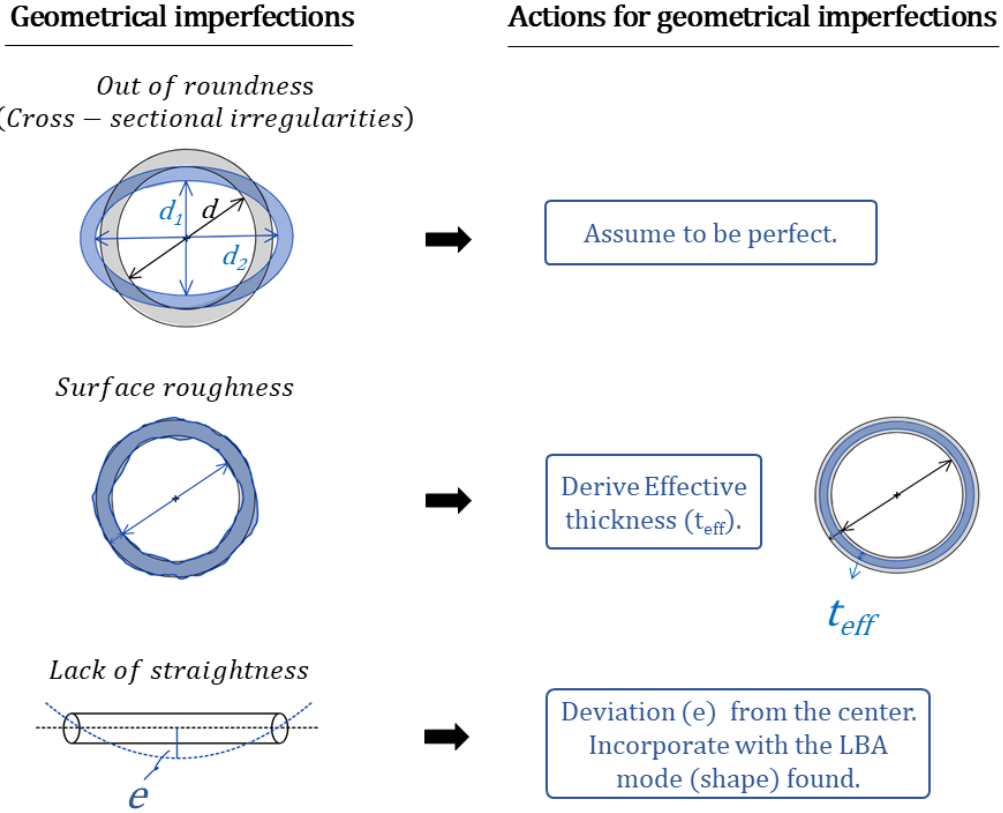


Figure 4.3: Parameters for Geometrical imperfections.

Material imperfection - Orthotropic behavior of material

The material's orthotropic behavior in this research is built from the young's modulus (E) in two printed directions and limited to the elastic scope. The orthotropic setting in ABAQUS has two options. One is the "Orthotropic" for the general solid object, and the other is the "Lamina" for in-plane stress [55] i.e., Shell structures. "Lamina" setting" has been used for all WAAM components' simulations as they are considered as shell structure in this thesis.

To simulate the "Lamina" orthotropic behavior, five parameters ($E_1, E_2, \nu_{12}, G_{12}, G_{13}, G_{23}$) have to be defined (listed in Table.4.1). The coordinate of the cylinder that shows the assigned material direction 1, 2 is shown in Fig.4.4. Unknown parameters are assumed in the analysis. E is the Young's Modulus, ν is the Poisson's ratio. The Shear modulus (G), which is calculated from Eq.4.1, is valid for isotropic materials, but being used as an assumption for building up orthotropic material's behavior because each direction of the material is being considered as isotropic with the young's modulus from its printed directions.

$$G = \frac{E}{2(1 + \nu)} \quad (4.1)$$

Table 4.1: Orthotropic settings in Transverse and Longitudinal direction.

Transverse	Longitudinal
$E_1=121$ GPa	$E_1=137$ GPa
$E_2=137$ GPa	$E_2=121$ GPa
$\nu_{12}=0.3$ (assumed)	$\nu_{12}=0.3$ (assumed)
$G_{12}=46538.5$ MPa	$G_{12}=52692.3$ MPa
$G_{13}=46538.5$ MPa (assume $\nu_{13}=0.3$)	$G_{13}=52692.3$ MPa (assume $\nu_{13}=0.3$)
$G_{23}=46538.5$ MPa (assume $\nu_{23}=0.3$)	$G_{23}=52692.3$ MPa (assume $\nu_{23}=0.3$)

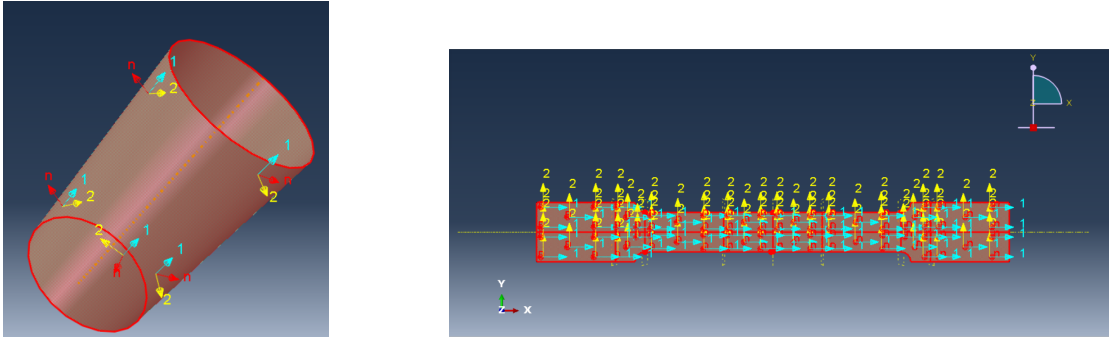


Figure 4.4: Coordinate of assigned material direction. Left: On a Cylinder. Right: On a tensile test coupon.

4.2 Simulation of Tensile test

The tensile test simulation aims to show FEA's feasibility to simulate the experiment and ensure the material non-linearity data is working correctly in ABAQUS. The compatibility between the acquired Engineering stress-strain curve from the simulation and the Engineering stress-strain curve from the lab test then can be validated. The overview of the tensile test simulation methodology can be seen in Fig.4.5.

The aims of the tensile test simulation are:

- Verify the correctness of using true tensile stress-strain curve (which is converted from engineering stress-strain curve) as material non-linearity input.
- Investigate the influence of material orthotropic behavior in tensile transverse and longitudinal directions.

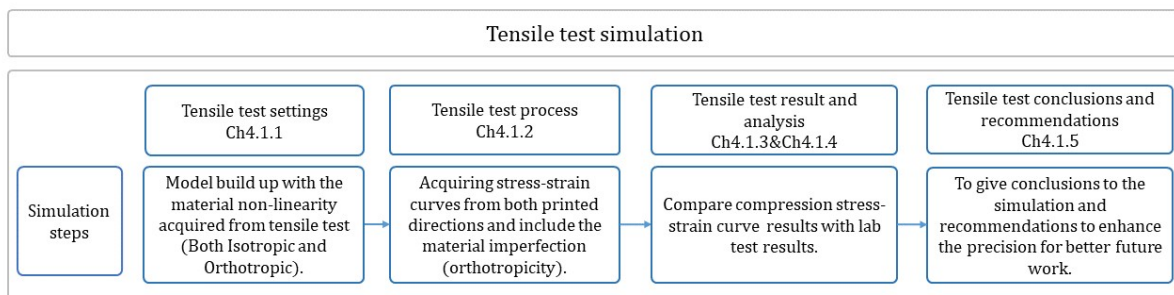


Figure 4.5: The overview of the Tensile test simulation methodology.

4.2.1 Tensile test settings

In this section, parameters in settings were presented. The overview of the Tensile test settings is shown in Fig.4.6.

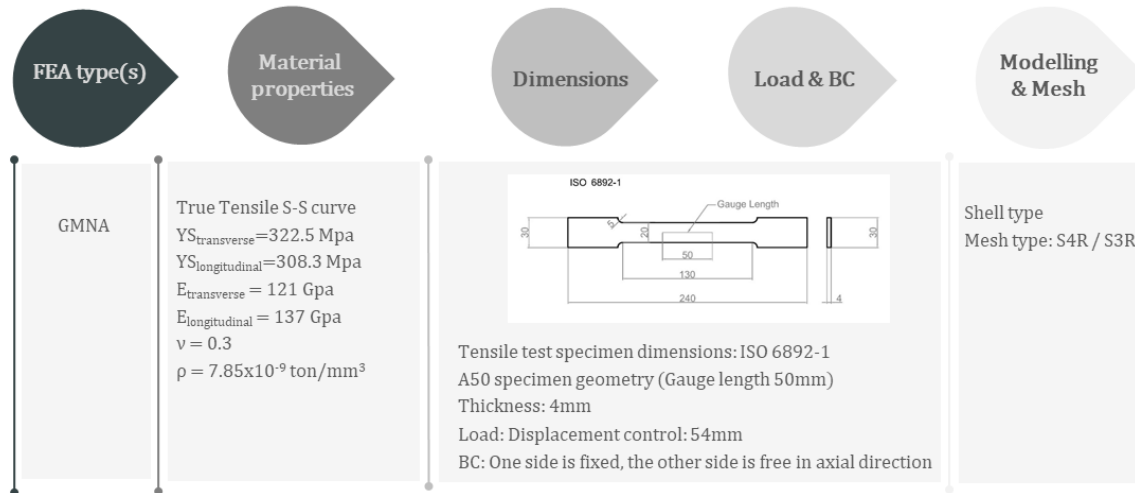


Figure 4.6: Tensile test settings in ABAQUS.

- FEA type(s):

GMNA was chosen to include the material non-linearity and the geometrical shrinkage during the process of the pulling. Since the tensile coupons were cut and milled, the geometrical imperfections were not included. Orthotropic behavior is considered for material imperfections.

- Material properties:

The true stress-strain curve in both transversal and longitudinal directions were considered as the material non-linearity. Poisson's ratio (ν) is 0.3. The density (ρ) of the material is $\rho = 7.85 \cdot 10^{-9} \text{ ton/mm}^3$. The Yield stress (YS) in the transverse direction is 322.5 MPa and in the longitudinal direction is 308.3 MPa. Young's modulus (E) in the transverse direction is 121 GPa and in the longitudinal direction is 137 GPa.

- Dimensions:

Tensile chip specimens were cut and milled according to ISO6892-1 with 50mm strain gauge and 4mm thickness (see Fig.4.7).

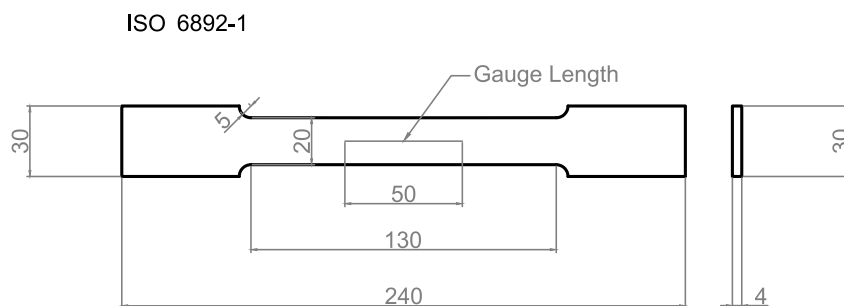


Figure 4.7: Dimensions of the tensile coupon according to ISO6892-1. (unit:mm)

- Load & BC:

In ABAQUS settings, The reaction force in the axial direction was gathered from the pulling side of the grip area to get the axial reaction force in relation to the displacement. A coupon has two clamping areas (grip faces). Both have a depth of 40mm from two ends. One end was fixed, and the other end can move freely in the axial direction. The load-displacement of 54mm was set at the boundaries. The number 54mm was set to acquire enough strain for reaching failure point (see Fig. 4.8).

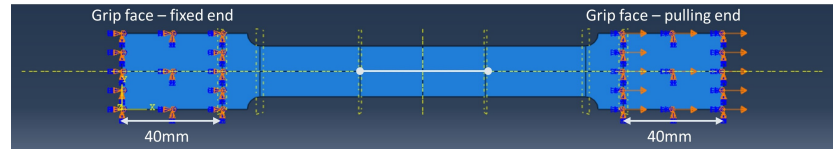


Figure 4.8: Tensile test boundary condition settings in ABAQUS.

- Modelling & Mesh:

The model is a shell type structure with 4 mm thickness. Meshes were built with 2 mm block (for Setting 1) and 1 mm block (for Setting 2 to Setting 6) type S4R (4-node general-purpose shell, reduced integration with hourglass control, finite membrane strains) and S3R (3-node triangular general-purpose shell, finite membrane strains).

Model modification of the coupon has been done with an enforced one percent area reduction at the middle (Fig. 4.9) (applied in Setting 3 to Setting 6). It is made to control the necking location. It can be seen that in setting 1 and setting 2, the failure point(s) of the coupon appears to be out of the gauge length (Fig.4.11).

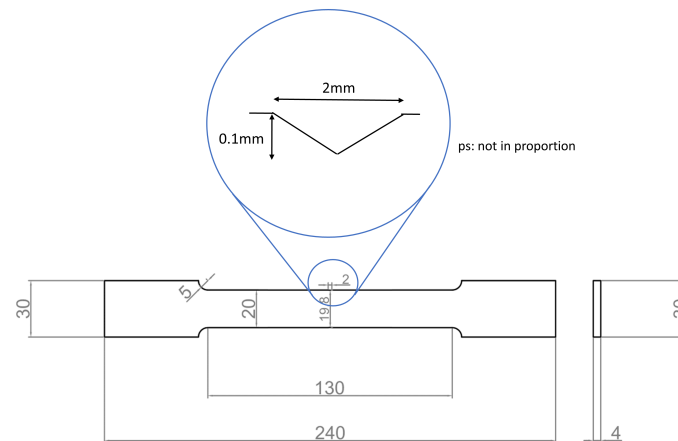


Figure 4.9: The one percent area reduction at the middle of the coupon for tensile test setting 3. (Unit: mm)

4.2.2 Tensile test process

Tensile test process in Fig.4.10 shows the steps to acquire correct inputs of the simulation through different settings. Setting 1 to 3 was the process that controls the failure point position from out of the gauge length to the center of the coupon to ensure that there is only one necking point. Setting 3 and 5 consider the isotropic and orthotropic behavior of the material in the transverse direction. Setting 4 and 6 consider the isotropic and orthotropic behavior of the material in the longitudinal direction.

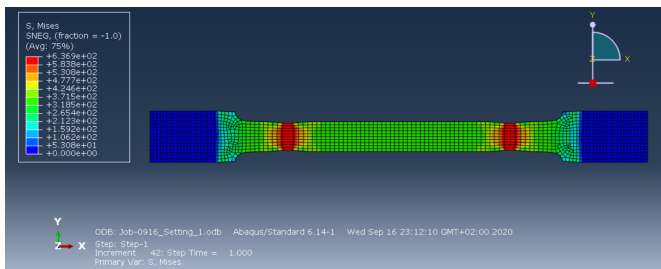
Process	Tensile test Settings	Material behavior and coupon printed direction	Failure (necking) point(s) and the location(s)	Mesh size	Actions / methods used for improving the simulation test
	1	Isotropic - Transverse	2 (out of the gauge length)	2mm	The material property was originally set to transverse direction since it fits the tensile test pulling direction
	2		1 (out of the gauge length)	1mm	Improving the mesh size from 2mm to 1mm
	3		1 (within the gauge length)		Controlled the necking point to the middle by decreasing 1% of the sectional area in the middle of the coupon
	4	Isotropic - Longitudinal			Material property set to Longitudinal but still is isotropic
	5	Orthotropic - Transverse			Material property set to Transverse orthotropic direction
	6	Orthotropic -Longitudinal			Material property set to Longitudinal orthotropic direction

Figure 4.10: Tensile test process and simulation improvement actions.

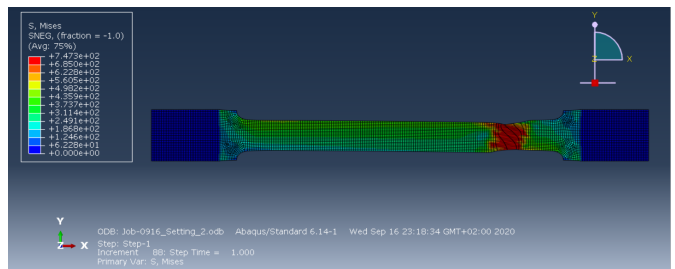
4.2.3 Tensile test results

Tensile test simulation result figures:

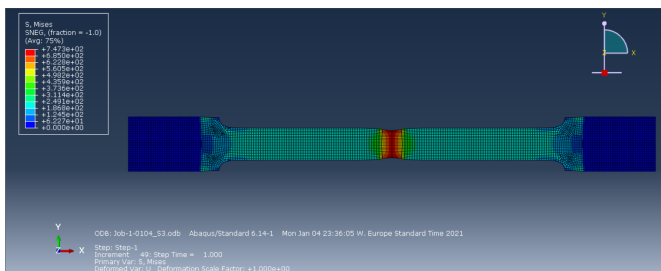
The simulation results of the tensile coupon in ABAQUS are in Fig.4.11. All settings have a load-displacement of 54mm at the pulling end. The red part(s) are the necking area. Setting 1 to Setting 2 shows that the refining of meshes (mesh block size from 2mm to 1mm) reduces the necking points from 2 to 1. Setting 2 to Setting 3 shows the successful control of the necking point, which falls in the gauge length. Setting 3 and 5 have both the material modeled in transverse printed direction (isotropic and orthotropic). Setting 4 and 6 have both the material modeled in longitudinal printed direction (isotropic and orthotropic).



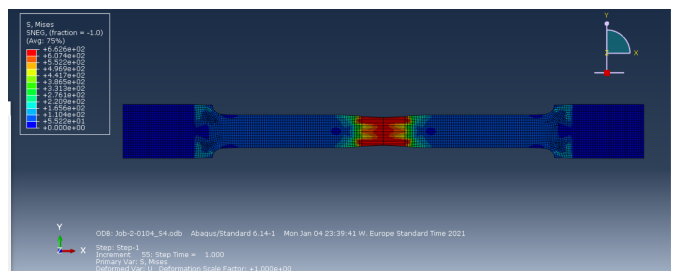
(a) Setting 1.



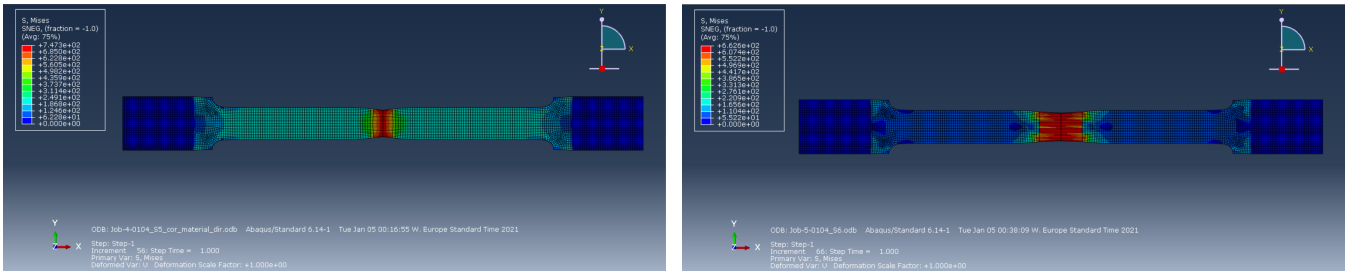
(b) Setting 2.



(c) Setting 3.



(d) Setting 4.



(e) Setting 5.

(f) Setting 6.

Figure 4.11: Tensile test result figures of Setting 1 to Setting 6.

Tensile test simulation stress-strain curves:

The outputs of the simulation are the engineering stress-strain curves acquired from the tensile test. Yield stresses and ultimate tensile stresses (UTS) are observed and compared to the experimental lab value, which is also the material non-linearity inputs.

The figure on the left side of Fig.4.12 shows the stress-strain curves under the failure point control process. These three curves from Setting 1 to Setting 3 were plotted with transverse isotropic material non-linearity. All curves match quite well before the ultimate tensile stress points have reached. After the ultimate tensile stress is reached, the strain of setting 1 and 2 curves go backward. In contrast, the stress-strain curve of the Setting 3 extends further. The difference comes from where the necking point occurred. The strain extends further if the necking point has appeared in the strain gauge.

The figure on the right side of Fig.4.12 shows the stress-strain curves with different combinations of material printed directions and material behavior (isotropic or orthotropic). Two printed directions have been analyzed, and the build-up of orthotropic material has been performed.

Setting 3 and Setting 5 consider the material printed in the transverse direction. The former has material with isotropic behavior, and the latter includes the material imperfection (orthotropicity); Setting 4 and Setting 6 consider the material printed in the longitudinal direction. The former has material with isotropic behavior, and the latter includes material imperfection (orthotropicity). Both show the orthotropicity in the transverse and longitudinal printed direction until the first digit below the decimal point with the unit is in MPa. (E for S3: 120551.44MPa; E for S4: 136557.22MPa; E for S5: 120551.16MPa ; E for S6: 136557.35MPa)

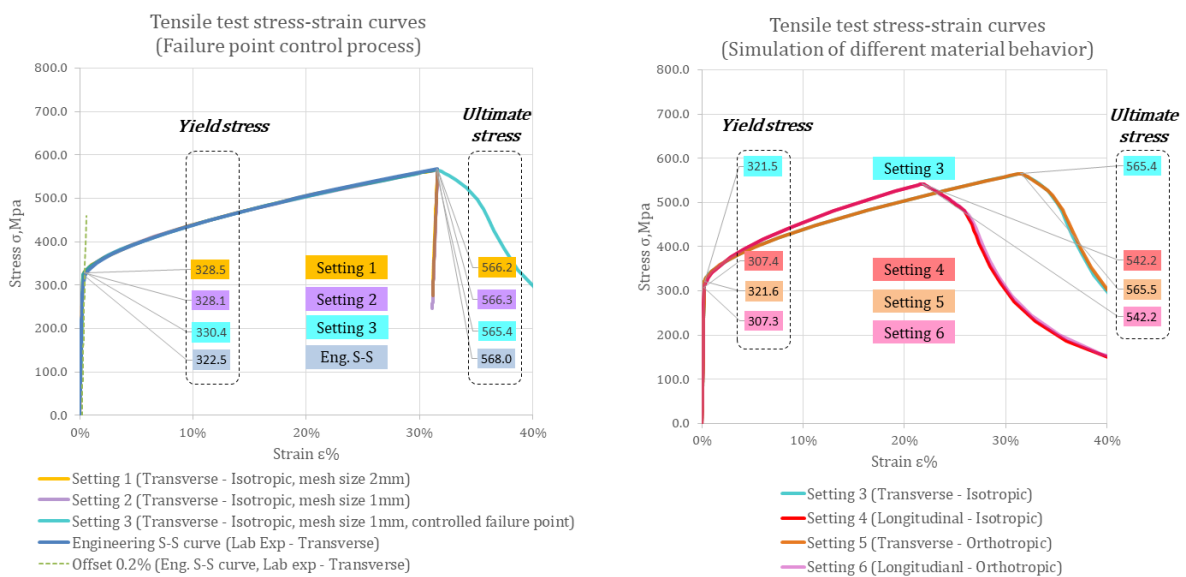


Figure 4.12: Tensile stress-strain curve results. Left: Failure point control process (Setting 1 to Setting 3); Right: Simulation of different material behavior (Setting 3 to Setting 6).

4.2.4 Tensile test analysis

By comparing the simulation result with the lab experiment, the validity of using non-linear material data in the tensile test can be verified. The comparison shows that the stress-strain curves from the simulations fit the material input (true stress-strain curve) quite well.

All curves from transverse printed direction are shown in the left part in Fig.4.13. It shows that:

- The yield stress of the curves of Setting 3 (321.5MPa) and Setting 5 (321.6MPa) have only 0.31% and 0.46% difference while compared with the material input (322.5MPa).
- The ultimate stress of the curves of Setting 3 (565.4MPa) and Setting 5 (565.5MPa) have only 0.46% and 0.44% difference while compared with the material input (568.0MPa).
- Both Setting 3 and Setting 5 have the same Young's modulus (120.6GPa) and have only 0.36% of difference compared to the material input (121GPa).

All curves from longitudinal printed direction are shown in the right part in Fig.4.13. It shows that:

- The yield stress of the curves of Setting 4 (307.4MPa) and Setting 6 (307.3MPa) have only 0.32% and 0.33% difference while compared with the material input (308.3MPa).
- The ultimate stress of the curves of Setting 4 and Setting 6 are the same (542.2MPa), which has only 0.33% difference while compared with the material input.
- Both Setting 4 and Setting 6 have the same Young's modulus (136.6GPa) and have only 0.29% of difference compared to the material input (137GPa).

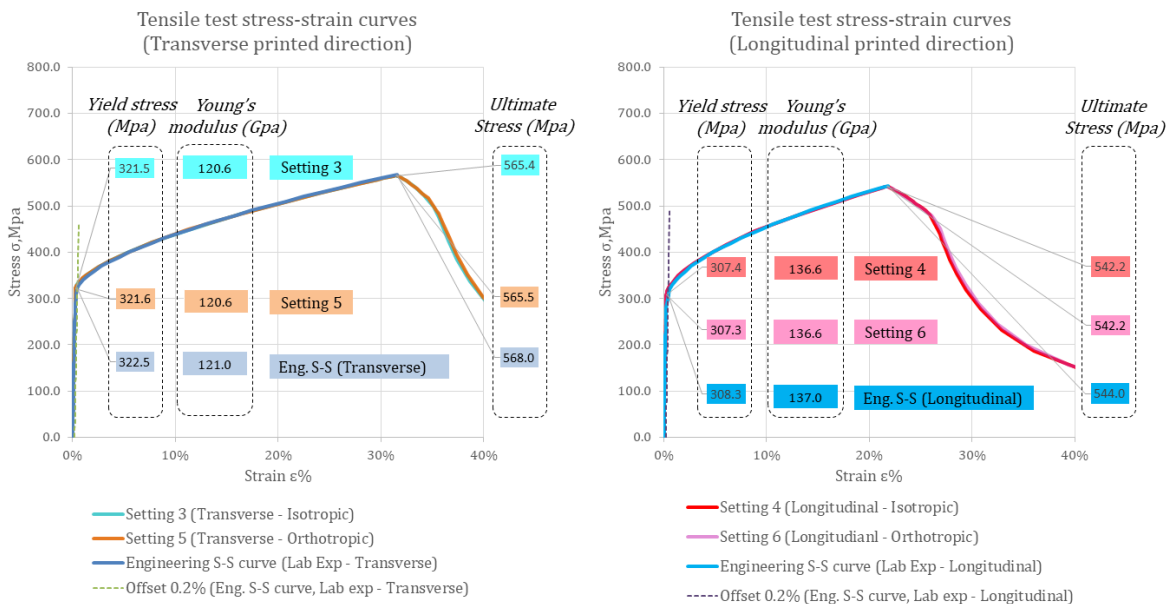


Figure 4.13: Tensile stress-strain curve results. Left: Transverse printed direction; Right: Longitudinal printed direction.

4.2.5 Tensile test conclusions

The aims in the beginning of this section are:

- Verify the correctness of using true tensile stress-strain curve (which is converted from engineering stress-strain curve) as material non-linearity input.
- Investigate the influence of material orthotropic behavior in transverse and longitudinal directions.

Findings of the aims, conclusions, and recommendations are listed below:

1. The input material non-linear data is the true stress-strain curve data, which is transferred from the engineering stress-strain curve. The analysis shows the simulation uses the material non-linearity data correctly. The results from the simulation (stress-strain curves) match the lab test result (engineering stress-strain curve) well before the ultimate stress point. The maximum error of Young's modulus in transverse and longitudinal printed direction are 0.36% and 0.29%; The maximum error of yield stress in transverse and longitudinal printed direction are 0.46% and 0.33%; The maximum error of ultimate stress in transverse and longitudinal printed direction are 0.46% and 0.33%. Therefore, the simulation using the material non-linearity input (the true stress-strain curve) is valid.
2. The orthotropic behavior has barely any influence in the tensile test simulation. The yield stress increase 0.03% from Setting 3 (321.5MPa) to Setting 5 (321.6MPa), and decrease 0.03% from Setting 4 (307.4MPa) to Setting 6 (307.3MPa). The ultimate stress increase 0.02% from Setting 3 (565.4MPa) to Setting 5 (565.5MPa), and the same in Setting 4 and Setting 6 (542.2MPa). The young's modulus is the same from Setting 3 to Setting 5 and Setting 4 to Setting 6.
3. The failure point(s) outside of the gauge length have been observed. By implementing finer meshes and prescribing a 1% reduction of cross-sectional area at the middle of the tensile coupon, the failure point falls into the gauge length. No significant change of yield stresses and ultimate stresses have been observed; only the stress-strain curves after the ultimate stresses reached went differently. The strain continues to increase for those with the failure point within the gauge length. Others have reduced strains be recorded.
4. Due to the lack of data, the orthotropic material buildup assume the shear modulus G_{23} to be 46538.5 MPa and Poisson ratio $\nu_{23}=0.3$. These parameters should be acquired from the material test to make the simulation more accurate.

4.3 Simulation of Compression test

In the compression test simulation, the aims are:

- Verifying whether the use of tensile material non-linearity in compression test is suitable or not.
- Find out the influence of orthotropic material behavior in compression test simulation.
- Finding the suitable failure mode from LBA modes.
- Check whether the analysis type, which includes the most factors in the analysis (in this section: Setting 5), acquires the closest value to the lab test.

The overview of the compression test simulation can be seen in Fig.4.14. The settings is presented in Ch4.3.1, the simulation process is shown in Ch4.3.2. This step includes a finding of similar buckle modes that correlate with the compression failure in the lab test. The result and analysis are delivered in Ch4.3.3 and Ch4.3.4. In Ch.4.3.5, conclusions and recommendations will be given.

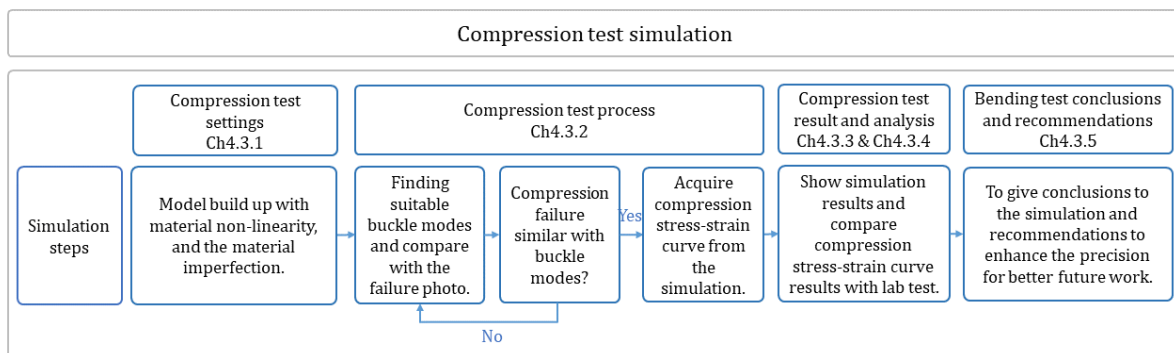


Figure 4.14: The overview of the compression test simulation methodology.

4.3.1 Compression test settings

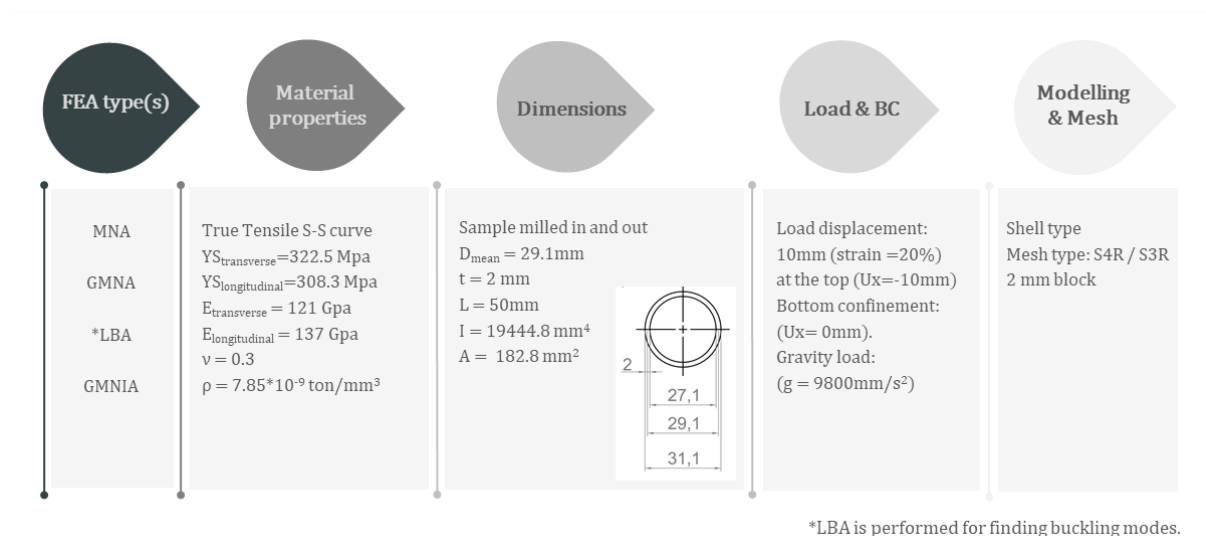


Figure 4.15: Compression test settings in ABAQUS.

- FEA type(s):

The process incorporates three analysis type. MNA, GMNA, and GMNIA. MNA is first presented to get the primary setting and result from the material non-linearity. Then, GMNA was chosen to include the geometrical non-linearity. Last, GMNIA. For material imperfection, orthotropic behavior is considered. For geometrical imperfections, since the sample was cut and milled, the geometrical imperfections from the WAAM process were not considered. Instead, the milled sample's geometrical imperfections are considered by incorporating the possible deformed shapes (modes) found from the LBA (Linear elastic bifurcation analysis or Linear buckling analysis) to give a better and more accurate insight on how the sample could deform. The finite element simulation practice typically takes a few percent of the shell thickness as the scale factor for incorporating imperfection to the numerical model [55], and for this simulation, 10% is used. Therefore, the scale factor is set to 0.2 from the 10% of the 2mm shell thickness.

- Material properties:

The true stress-strain curve in the transverse direction is considered the main direction due to the tube's printing direction. The longitudinal printed directions was used in building up the orthotropic material in the linear part. The Yield stress (YS) in the transverse direction is 322.5 MPa and in the longitudinal direction is 308.3 MPa. Young's modulus (E) in the transverse direction is 121 GPa and in the longitudinal direction is 137 GPa. Poisson's ratio (ν) is 0.3. The density (ρ) of the material is $\rho = 7.85 \cdot 10^{-9} \text{ ton/mm}^3$.

- Dimensions:

Compression test specimen were cut and milled in and out (see Fig.4.16). The milled sample has the thickness (t) = 2 mm, length (L) = 50mm, Moment of inertia (I) = 19444.8 mm⁴, and the sectional area (A) before compression is 182.8 mm².

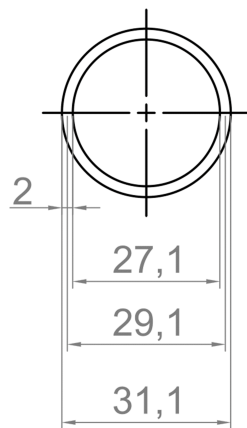


Figure 4.16: Milled sample's cross-sectional sizes. (unit: mm)

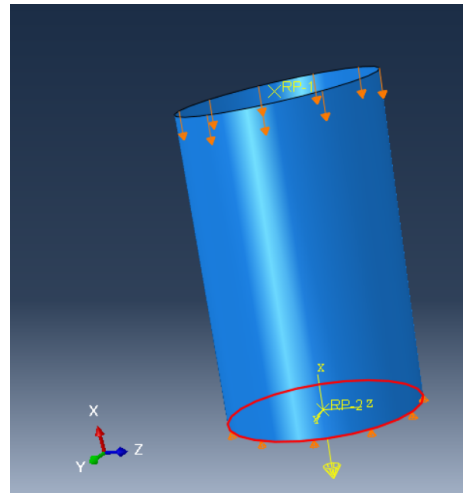


Figure 4.17: Compression test boundary condition settings in ABAQUS.

- Load & BC:

The sample in ABAQUS is compressed for $10mm$ (20% of the total length; total length = $50mm$). In the setting, the displacement at the sample top is set to $15mm$ ($U_x = -10mm$) and the confinement at the sample bottom (highlighted in red in Fig.4.17) is $0mm$ ($U_x = 0mm$). Gravity load with $g = 9800mm/s^2$ is also added to the simulation.

- Modelling & Mesh:

The model is a shell type structure with $2mm$ thickness. Meshes were built with $1mm$ blocks type S4R (4-node general-purpose shell, reduced integration with hourglass control, finite membrane strains) and S3R (3-node triangular general-purpose shell, finite membrane strains).

4.3.2 Compression test process

Settings with different analysis types and imperfections are listed in Fig.4.18. The transverse printed direction was chosen because it is the direction that matches the printing direction of this tube.

Compression test simulation setting list	Analysis type	Geometrical imperfection	Material imperfection
Setting 1 (S1)	MNA	No	No: Isotropic
Setting 2 (S2)	GMNA	No	No: Isotropic
Setting 3 (S3)	GMNIA (Material imperfection only)	No	Yes: Orthotropic
Setting 4 (S4)	GMNIA (Geometrical imperfection only)	Yes: Possible deformed shapes (modes) found from LBA	No: Isotropic
Setting 5 (S5)	GMNIA (Material imperfection + Geometrical imperfection)	Yes: Possible deformed shapes (modes) found from LBA	Yes: Orthotropic

Figure 4.18: The Compression test simulation setting list.

In between the simulation process, the LBA was performed to find the more realistic failure (shapes) modes for the compression test.

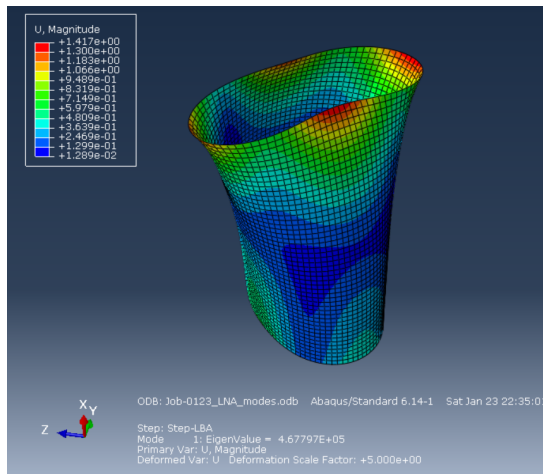
The reason for conducting this step is that the failure shape in Setting 2, which doesn't consider the geometrical imperfection, shows an unrealistic shape (see Fig.4.21(b)) compared to the compression lab test failure (see Fig.4.20), and the LBA shows possible deformed shapes with different modes.

The top 6 possible modes are shown in 4.19. Mode 2 is actually the same as mode 1 but with a shift in angle. Therefore they have the same linear buckle load. Mode 4 is also identical to mode 3. Mode 5 is also identical to mode 6, and it is the least possible to happened because the linear buckle load is the highest in LBA.

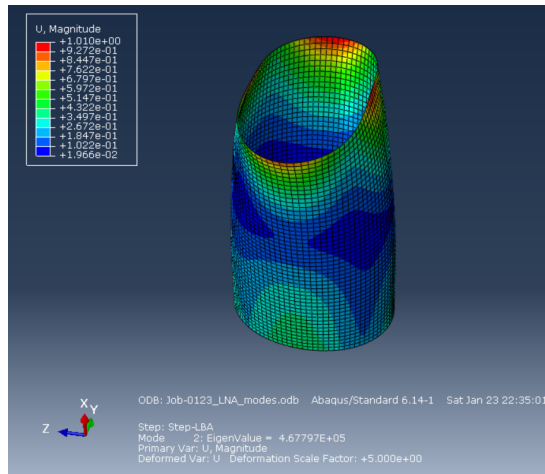
The simulation in Setting 3 and 4 (shown in Fig.4.21(c) and (d)) use the first mode in LBA, the scale factor of the geometrical imperfections is 0.2 (1/10 of the shell thickness 2mm).

The first mode not only has the lowest linear buckling load but possess the shape that shows the closest to the experimental failure shown in Fig.4.20.

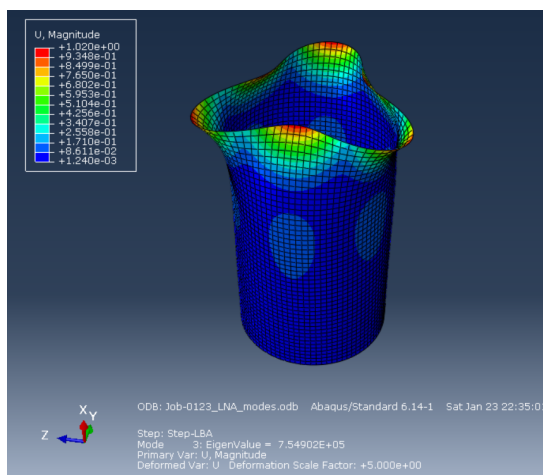
One thing to mention here is that the linear buckling load from LBA is far away from the true value because LBA is a linear calculation that normally overestimates the strength. Therefore, this analysis informs only the buckling modes (deformed shapes) used as the geometrical input in the compression test instead of the true buckling load.



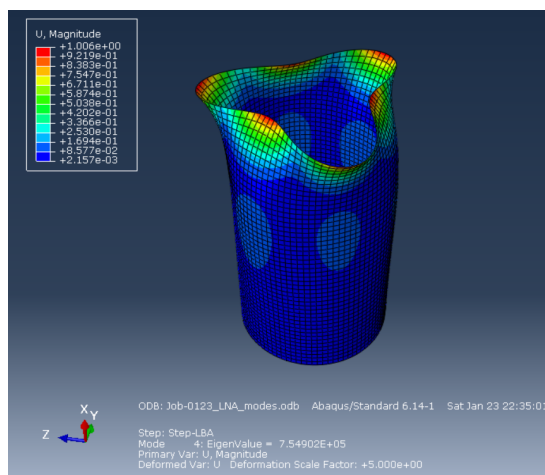
(a) LBA mode 1. (Buckle load = 467.8KN)



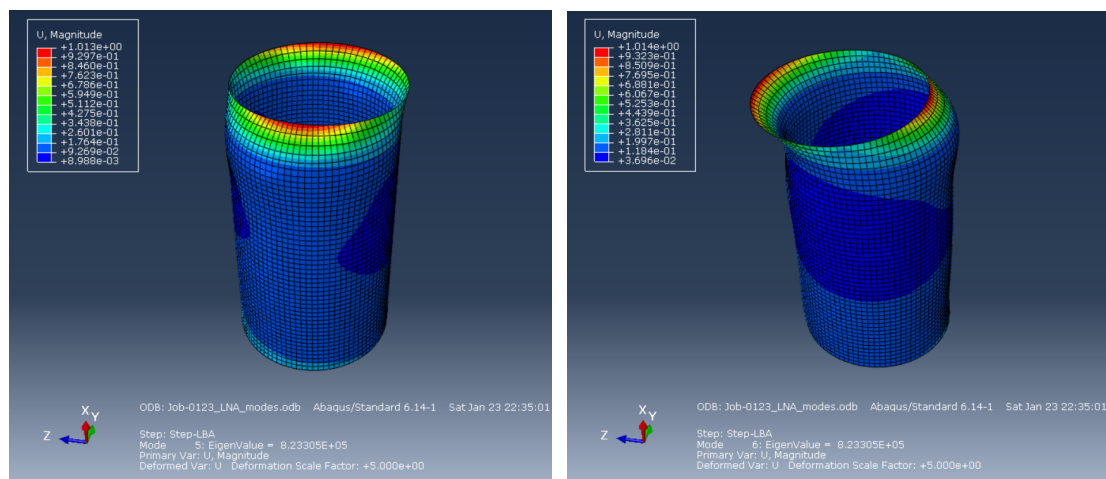
(b) LBA mode 2. (Buckle load = 467.8KN)



(c) LBA mode 3. (Buckle load = 754.9KN)



(d) LBA mode 4. (Buckle load = 754.9KN)



(e) LBA mode 5. (Buckle load = 823.3KN) (d) LBA mode 6. (Buckle load = 823.3KN)

Figure 4.19: Possible compression failure modes found in LBA. (a) to (f): mode 1 to mode 6.



Figure 4.20: The Compression lab test failure.

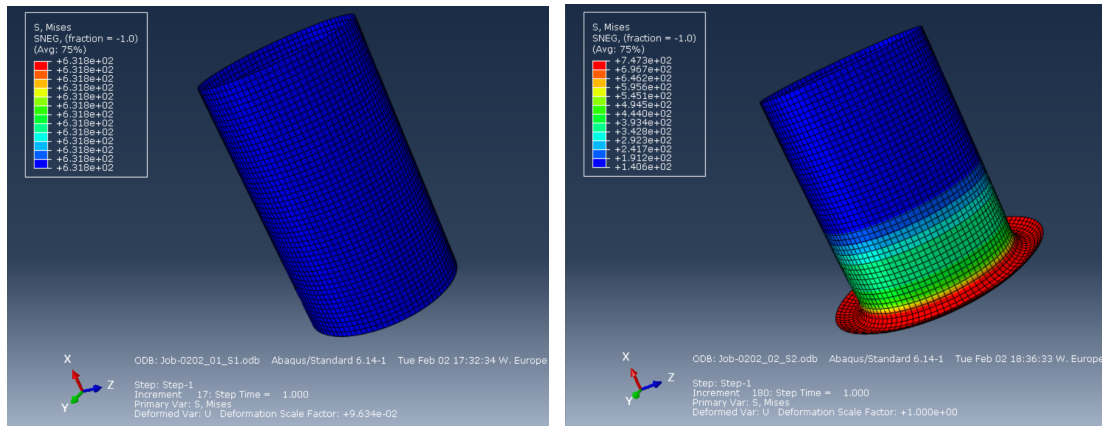
4.3.3 Compression test results

Compression test simulation result figures:

Compression simulation result figures in ABAQUS are shown in Fig.4.21. The compression test has a load displacement setting of 10mm (strain = 20%). All of the Settings reached strain = 20% except for Setting 3, which converged at strain = 11%.

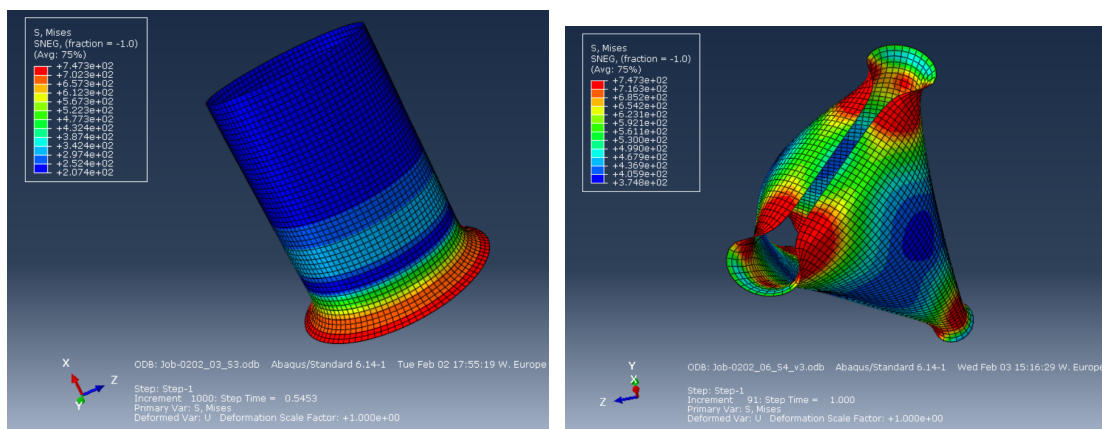
Observations of deformed shapes are listed:

- With only material non-linearity included (GMNA), Setting 1 deformed only in the axial direction (getting shorter).
- With geometrical non-linearity and additional material imperfections (orthotropicity) (GMNIA) take part in Setting 2 and Setting 3, both deformed outward in a “perfectly” way (symmetry along the tube axis). It is reasonable since the geometrical imperfections are not included
- The inclusion of the geometrical imperfection found from LBA (model 1) yields the most similar results to the lab test failures in Setting 4 and Setting 5.



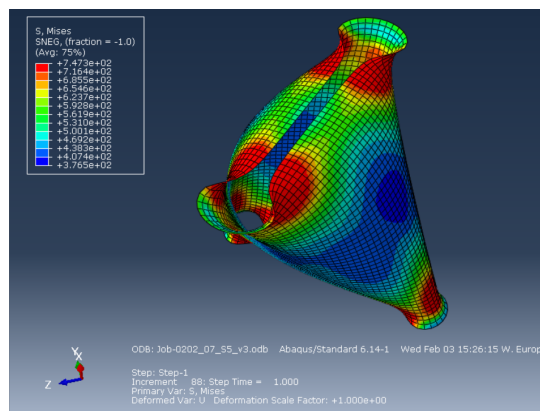
(a) Setting 1. (strain = 20%)

(b) Setting 2. (strain = 20%)



(c) Setting 3. (strain = 11%)

(d) Setting 4. (strain = 20%)



(e) Setting 5. (strain = 20%)

Figure 4.21: Compression test result figures with strain denoted.

Compression test simulation stress-strain curves:

The aiming result (output) of the compression simulations is the compression stress-strain curves (S1 to S5). To plot the uniaxial stress-strain curve, the reaction force in the axial direction was gathered from the cross-sectional area of the tube and correlate with the strain. All curves are shown in Fig.4.22. Setting 1, Setting 2, Setting 4, Setting 5 reach the original strain target of 20%. Setting 3 converge

earlier at 11%. However, this doesn't affect the findings of critical points (yield stress and ultimate stress points) in this simulation.

Several findings from compression stress-strain curve results are addressed below:

For Yield stress:

- In general, the yield stress does not affect much by the increasing complexity of the analysis (All yield stresses have less than 2.2% difference when compared to Setting 5).
- The influence of the material imperfection (Orthotropicity) is minimal. From Setting 4 to Setting 5, the inclusion of orthotropicity makes no difference for the yield strength. From Setting 2 to Setting 3, the yield strength decrease from 323.7MPa to 321.2MPa, which is 0.78% drop.
- Higher yield stresses in Setting 4 and Setting 5 may come from the different deformed shape, which caused by the inclusion of the geometrical imperfection from LBA.

For Young's modulus:

- Young's modulus of all curves are around the material non-linearity input of the transverse printed direction (121GPa). The young's modulus of Setting 2 and Setting 3 are both 121.5GPa, and the young's modulus of Setting 4 and Setting 5 are 121.2 GPa.
- The influence of the material imperfection (Orthotropicity) on the young's modulus is also minimal. The inclusion of effective thickness reduce the value of young's modulus from 121.5GPa (Setting 2 and Setting 3) to 121.2GPa (Setting 4 and Setting 5), which is a decrease of 0.25%.

For Ultimate stress:

- In general, the Ultimate compression stress decreases when the setting of the analysis becomes more complex as more realistic conditions are applied to the simulation (Setting 1 to Setting 5).
- Setting 1 shows no sign of ultimate compression stress even when 20% of the compression strain reached.
- Ultimate stress decreases prominently when geometrical imperfection was taken into consideration (can be seen from Setting 3 to Setting 5 as well as Setting 2 to Setting 4).
- Ultimate stress point of Setting 5 indicate the simulated buckling load. The buckling load can be calculated by multiplying the ultimate stress of Setting 5 (354.7MPa) to the cross-sectional area ($182.8mm^2$) of the tube. Therefore, the buckling load from the simulation is $354.7MPa * 182.8mm^2 = 64839.16N = 64.8KN$.

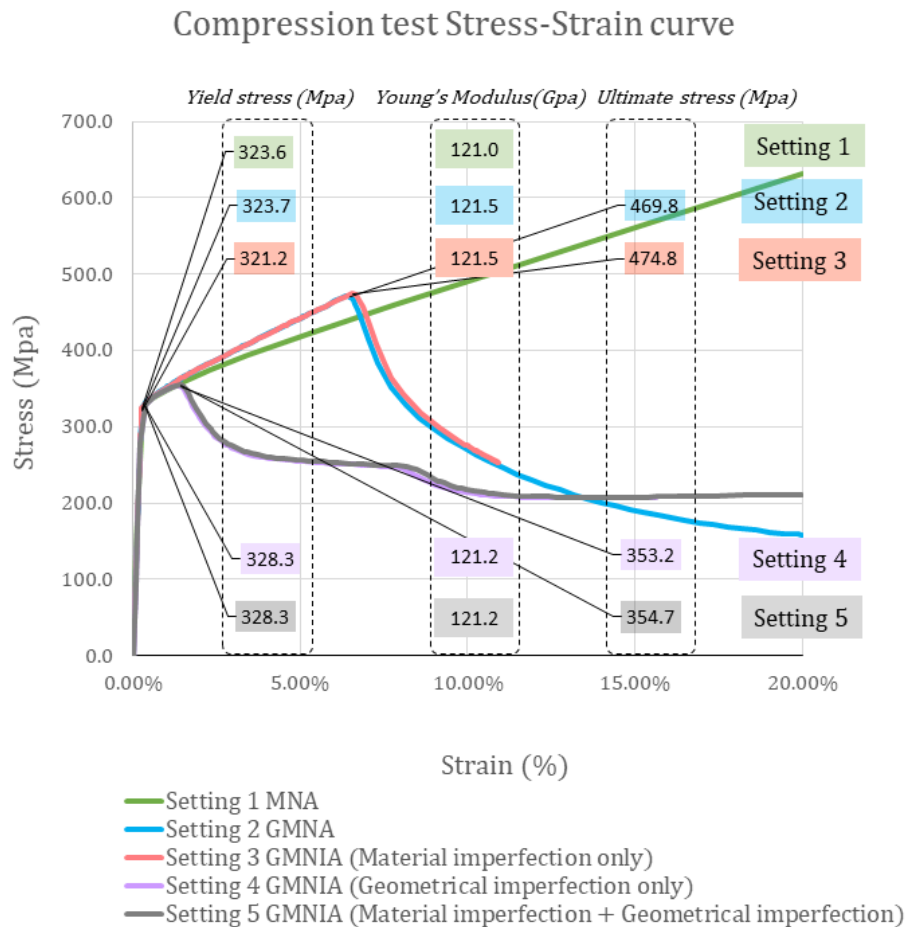


Figure 4.22: The Compression test results.

4.3.4 Compression test analysis

In this section, the result from the compression lab test is compared to the numerical simulation in Fig.4.23. Only the graph with strain below 5% from the components' lab experiment is provided. Although not shown in the graph, the compression sample's failure load from the lab test is 57 kN. The analysis is shown in Table.4.2.

Several discussions are addressed below:

- Yield stress reached before the buckling occurred. It proves the validity of the compression test.
- The simulated result shows a promising result when yield stress is compared with the lab test. The maximum error between all numerical simulation results and lab result has around 8.4% difference in Setting 5 (see Table.4.2).
- Higher yield stresses in Setting 4 and Setting 5 were not expected (2.21% increase from Setting 3 to Setting 5 and 1.42% increase from Setting 2 to Setting 4). The reason comes from the inclusion of the geometrical imperfection from LBA, which may slightly increase the strength before the deformation starts.
- The Young's modulus (slope in Fig.4.23) of the lab result is significantly larger than the simulation result. It can be seen that the strain of the Yield points in lab results have 1% strain difference (0.5mm) to the simulation results. The discussions of the error are presented in Section.4.3.5.
- Stress-strain curves from Setting 2 to Setting 5 reach ultimate stress at the lower strain than the lab experiment. A further comparison of the ultimate stress point couldn't be made due to the lack of the complete stress-strain curve provided by the lab test.

- Failure loads from the simulation show a closer result to the lab result when the settings include more factors in the analysis (see Section.4.2). From Setting 2 to Setting 5, the percentage errors decrease from +52.27% to +13.75%.

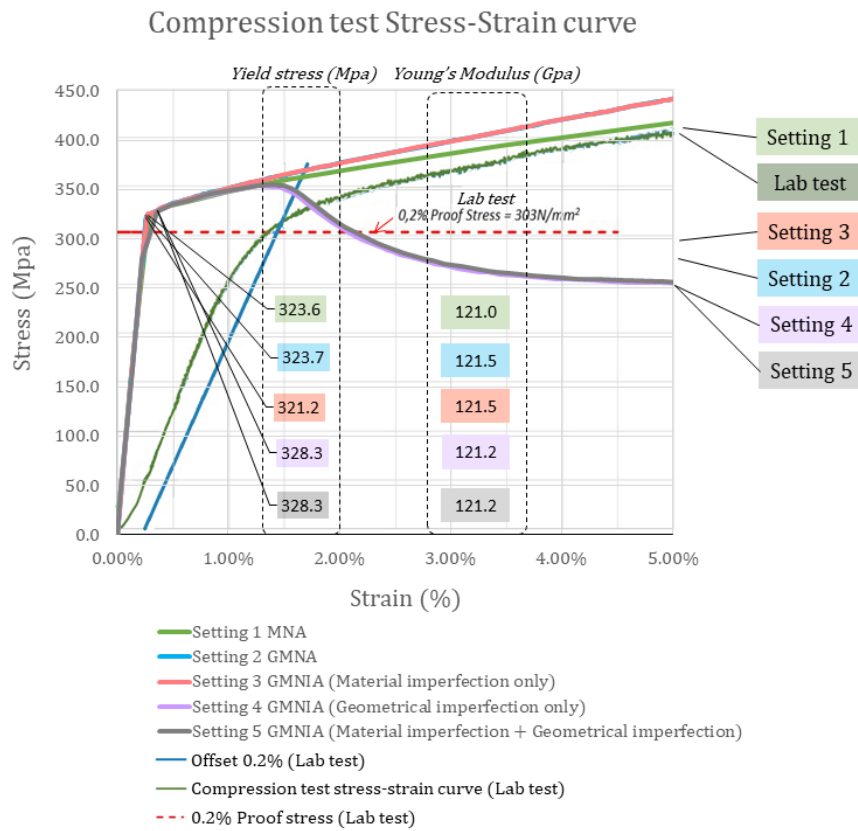


Figure 4.23: The comparison of compression test result and the lab result at strain below 5% [Adapted] [1].

Table 4.2: The Compression test simulation analysis.

Compression test simulation setting	Result: Yield stress (Mpa)	Yield stress percentage error (compare to lab exp)	Result: Ultimate stress (Mpa)	Result: Failure load (ultimate stress*cross-sectional area)	Failure load percentage error (compare to lab exp)
Lab test	303.0	-	-	57.0	-
Setting 1 (S1)	323.6	6.80%	-	-	-
Setting 2 (S2)	323.7	6.83%	469.8	85.9	50.67%
Setting 3 (S3)	321.2	6.01%	474.8	86.8	52.27%
Setting 4 (S4)	328.3	8.35%	353.2	64.6	13.27%
Setting 5 (S5)	328.3	8.35%	354.7	64.8	13.75%

4.3.5 Compression test conclusions

This section answers the questions from the beginning of this compression test simulation section and gives conclusions and recommendations.

The aims in the beginning of this chapter are:

- Verifying whether the use of tensile material non-linearity in compression test is suitable or not.

- Find out the influence of orthotropic material behavior.
- Finding the suitable failure mode from LBA modes.
- Check whether the analysis type, which includes the most factors in the analysis (in this section: Setting 5), acquires the closest value to the lab test.

Findings of the aims, conclusions, and recommendations are listed below:

1. The use of Van Bolderen's compression test result fails to verify the first aim (whether the use of tensile material non-linearity in compression test is suitable or not) because the lab experiment contains possible errors. The most obvious errors from the lab experiment is that Young's modulus (slope in Fig.4.23) of the specimen is too less (more details in Section.4.3.4).

However, a similar lab experiment performed by Laghi [53] (discussed in Section.3.3.2) shows the experimental results of compression stress-strain curve is nearly the same as the experimental results of tensile stress-strain curve before the yield point. Therefore, the FEA's compression stress-strain curve is more reasonable and accurate than the lab test curve from Van Bolderen.

When compare the numerical result (Setting 5) to the transverse tensile stress-strain curve (322.5 MPa; 121GPa) until the yield point, the yield stress in the simulation only has 1.8% error, and young's modulus only has 0.41% errors.

2. The error in Van Bolderen's plot mostly comes from 1% strain difference (0.5mm) between the lab test result and simulation results at where the yielding happened. Van Bolderen's thesis mentioned possible errors in the lab experiment measurement. The displacements of the machine were measured directly instead of a strain gauge on the sample, which can deliver a more precise result. Also, circular dents on the sample's bearing plate, which occurred due to the concentrated force at the sample's top and bottom boundaries, have been observed. This means more strains have been measured.

Therefore, it is recommended to use strain gauges in compression lab test to deliver a more precise result.

3. It is expected to have more precise simulation results (values closer to the results from the lab test) when more factors were included in the analysis (Setting 5).

However, for the yield stress of Setting 5, it does not possess the closest value to the lab test. The possible reason might come from the excessive strain measured. If the strain measured at the yield stress point is correct (smaller), then young's modulus measured will become larger. The accurate measurement could lead to slightly larger yield stress measured. Another reason may be that there is only one sample in the lab test, and the reliability might cause some concerns.

4. Mode one has been chosen as the possible failure shape in the analysis. The LBA shape's inclusion helped to get a closer failure load compared with lab results from Van Bolderen's result (the percentage errors decrease from +52.27% to +13.75%). However, The failure mode found from LBA acquires a similar but not identical failure shape. This difference may cause the findings of buckling load varies. The other thing is that the LBA settings' scale factor is only an assumption for the milled sample. The larger scale factor being used will lead to a more prominent imperfection, which will decrease the failure load. More findings of the relation between the buckling load and the scale factors are not presented in this chapter because the main focus is the results until the yield stress point (yield stress and the young's modulus). The method of finding the relation between the buckling load and the scale factors will be used in the simulation of the buckling test in Section.4.5 because the buckling load of the slender structure is more prone to geometrical imperfections.

5. The orthotropicity of the material has a minimal effect on the yield stress and young's modulus. The yield stress, from Setting 4 to Setting 5, have the same value. From Setting 2 to Setting 3, the yield strength decrease from 323.7MPa to 321.2MPa, which is a 0.78% drop. As for the young's modulus, Setting 2 and Setting 3 are both 121.5GPa, and Setting 4 and Setting 5 are both 121.2 GPa.

6. Only one compression test performed from Van Bolderen's test might cause some concerns of the compared data.

4.4 Simulation of Bending test

In the bending test simulation, the aims is to

- Investigate the validity of using derived effective thickness ($t_{eff}=3.01mm$) for incorporating surface roughness.
- See how the orthotropic behavior will influence the simulation.
- Check whether the analysis type, which includes the most factors in the analysis (in this section: Setting 5), acquires the closest value to the lab test.

The overview of bending test simulation can be seen in Fig.4.24. The settings is presented in Section4.4.1, the simulation process is shown in Ch4.4.2. This step acquire deflections from the center of the tube. In Ch4.4.3 and Ch4.4.4, simulation results will be organized and compared with lab test result. The deflection comparison of the simulate bending stiffness and the bending stiffness in the lab experiment can indicate the validity of the assumption. In Ch.4.4.5, conclusions and recommendations will be given.

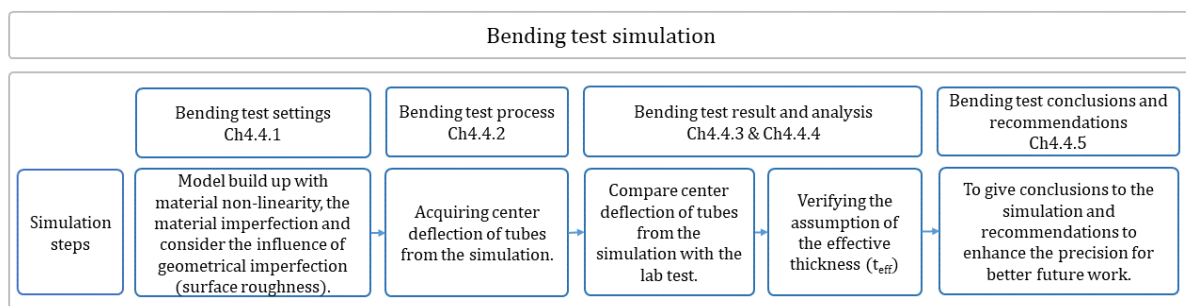
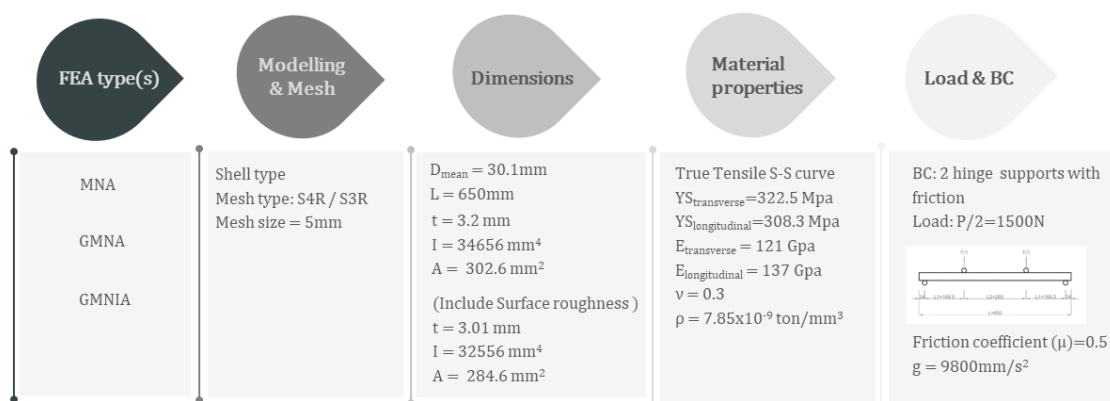


Figure 4.24: The overview of Bending test simulation methodology.

4.4.1 Bending test settings

The overview of the Four-points bending test setting is shown in Fig. 4.25.



ps: For properties and dimensions for bearing and supports, please see the discription in the paragraph.

Figure 4.25: Four points bending test settings.

- FEA type(s):

Although lab test is designed to perform in the elastic range, the material non-linearity is considered since concentrated stress may lead to local non-linear deformation and influence the deflections found at the tube center.

The analysis first starts with material non-linear analysis (MNA). Secondly, the geometrically and materially nonlinear analysis (GMNA), which considered geometrical non-linear behavior. Last, the geometrically and materially non-linear analysis with imperfections (GMNIA). It should be noticed that the only geometrical imperfection taken into consideration from WAAM is the surface roughness. Lack of straightness has been ruled out since the lab test's deflection data are the average value measured from four sides of the tube.

- Modelling & Mesh:

The model of the tube is a shell type structure. As for bearings and supports, those are built with solid type. All components' meshes are in $5mm$ block type S4R (4-node general-purpose shell, reduced integration with hourglass control, finite membrane strains) and S3R (3-node triangular general-purpose shell, finite membrane strains).

- Dimensions:

For the four-points bending test and buckling test, the nominal diameter and wall thickness are $30.1mm$ and $3.2mm$. The surface roughness has been considered by using the effective thickness of $3.01mm$ (see Section 3.4.2 for the derivation). The length of the tube is $650mm$. More detailed dimensions is shown in Fig.4.26.

The cross-sections of supports and load bearings have the same diameter of $26mm$. The supports have the length of $100mm$; the bearings have the length of $50mm$ but cut in half.

- Material properties:

The true stress-strain curve in the transverse direction is considered as the main direction because it reflects the printing direction of the tube. The longitudinal properties were used for building up the orthotropic material behavior in the elastic part. The Yield stress (YS) in the transverse direction is 322.5 MPa and in the longitudinal direction is 308.3 MPa. Young's modulus (E) in the transverse direction is 121 GPa and in the longitudinal direction is 137 GPa. Poisson's ratio (ν) is 0.3 . The density (ρ) of the material is $\rho=7.85 \cdot 10^{-9} ton/mm^3$.

The supports and load bearings have young's modulus of $210GPa$ and Poisson's ratio $\nu = 0.3$. All are assumed to be solid metal and no yielding throughout the simulation process.

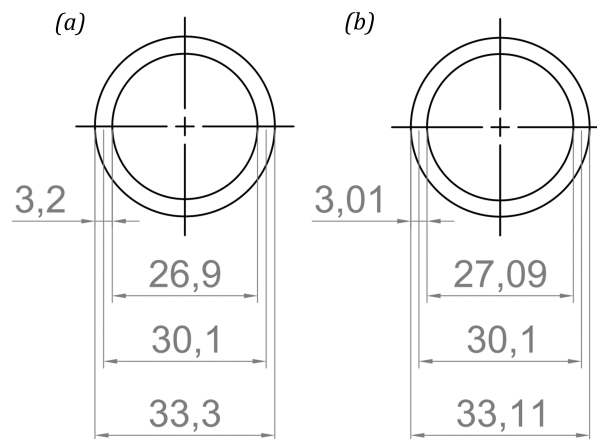


Figure 4.26: Specimen cross-sectional sizes of four points bending test . (a) Nominal cross-sectional sizes with $3.2mm$ thickness. (b) Effective cross-sectional sizes considering the influence of surface roughness with $3.01mm$ effective thickness (unit in mm).

- Load & BC:

Overview of the Four-point bending test boundary condition and Load settings can be seen in Fig.4.27. The setup scheme with detailed dimensions is presented in Fig.4.28.

The boundary conditions have been set to simulate the lab experiment. For two circular supports at the bottom (shown in Fig.4.27(a) in orange), both ends are fixed. For two load bearings at

the top (shown in Fig.4.27(b) in green), all movements, except for translational movement in y -direction, are fixed ($U_x=0$, $U_y \neq 0$, $U_z=0$, $U_{R_x}=0$, $U_{R_y}=0$, $U_{R_z}=0$). For the WAAM tube, two side confinements at two ends are used to prevent the rolling of the tube (shown in Fig.4.27(c) in red) ($U_x \neq 0$, $U_y \neq 0$, $U_z=0$, $U_{R_x} \neq 0$, $U_{R_y} \neq 0$, $U_{R_z} \neq 0$). The sliding friction coefficient of dry steels is around 0.42 to 0.62 [56]. Hence, the friction coefficient assumption of $\mu=0.5$ is assumed.

Two 1500N (each $P/2=1500\text{N}$) forces are added onto the load-bearing tops as the distributed load form (shown in Fig.4.27(d)).

The Gravity, with the value $g = 9800\text{mm}/s^2$, is included in the simulation for the WAAM tube, but the load bearings and supports are excluded. They are linked to the machine in the lab experiment, and their self-weight is not acting on the WAAM tube.

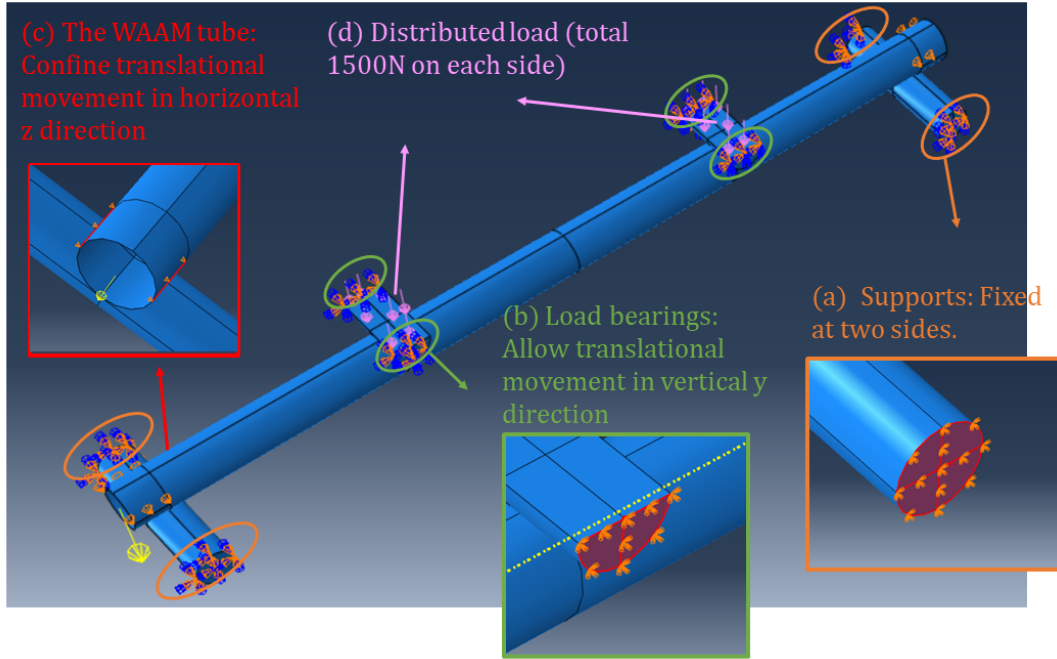


Figure 4.27: Four points bending test BC and Load setting.

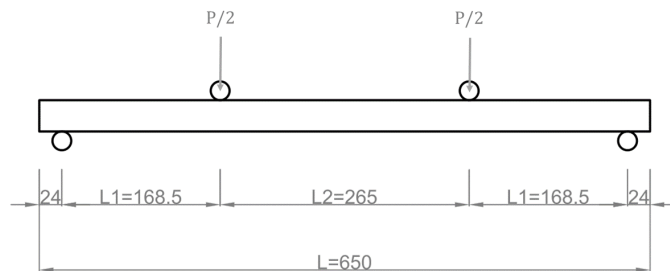


Figure 4.28: Four points bending test schematic drawing (unit in mm).

4.4.2 Bending test process

Settings with different analysis types and imperfections are listed in Table.4.3. The transverse printed direction is chosen because it is the direction that matches the printing direction of this tube.

Table 4.3: Four points bending test simulation setting list.

Bending test simulation setting list (Printed in Transverse direction)	Analysis type	Geometrical imperfection	Material imperfection
Setting 1 (S1)	MNA	No	No: Isotropic
Setting 2 (S2)	GMNA	No	No: Isotropic
Setting 3 (S3)	GMNIA (Material imperfection only)	No	Yes: Orthotropic
Setting 4 (S4)	GMNIA (Geometrical imperfection only)	Yes: Surface roughness	No: Isotropic
Setting 5 (S5)	GMNIA (Material imperfection + Geometrical imperfection)	Yes: Surface roughness	Yes: Orthotropic

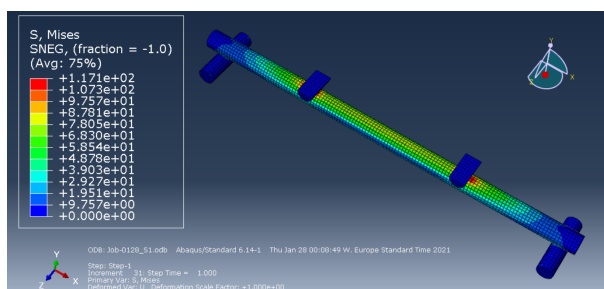
4.4.3 Bending test results

Bending test simulation result figures:

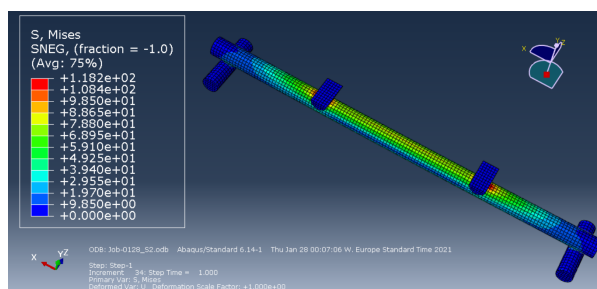
From the simulation, the the Von Mises stress distributions, deformed shapes, and center deflection for each settings are displayed in Fig.4.29, Fig.4.30, and Fig.4.31.

The results show that:

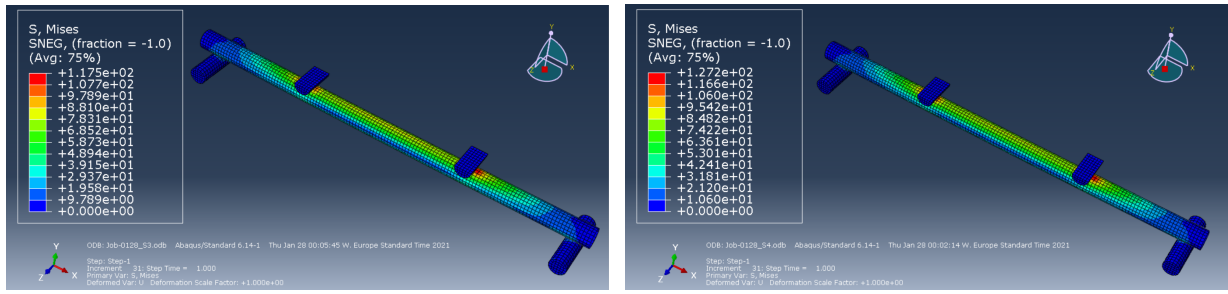
- For all settings, the highest value of Von Mises stress appears at the area where loads are applied (shown in Fig.4.30).
- Stress levels shown in all settings are lower than the yield stress of the tube material (322.5 MPa). Therefore, the elastic assumption of applying $P/2=1500\text{N}$ is valid.
- From Setting 1 to Setting 2, while geometrical nonlinearity is included in the simulation, the deflection at the middle increase.
- The inclusion of orthotropic material behavior (from Setting 2 to Setting 3 as well as Setting 4 to Setting 5) caused less deformation. It is reasonable since a higher young's modulus in longitudinal direction is considered.
- It has been observed that when more deflections occur in the tube, higher Von Mises stress also took place.



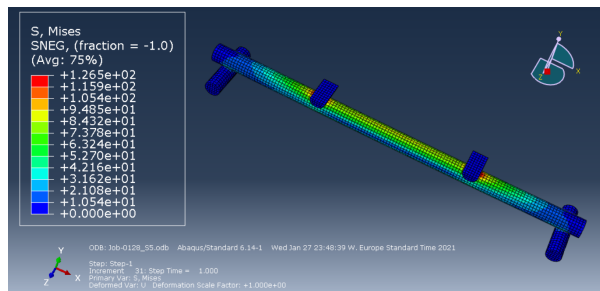
(a) Setting 1 (Maximum Von Mises stress: 117.1 MPa; Center deflection: 1.996mm).



(b) Setting 2 (Maximum Von Mises stress: 118.2 MPa; Center deflection: 2.022mm).

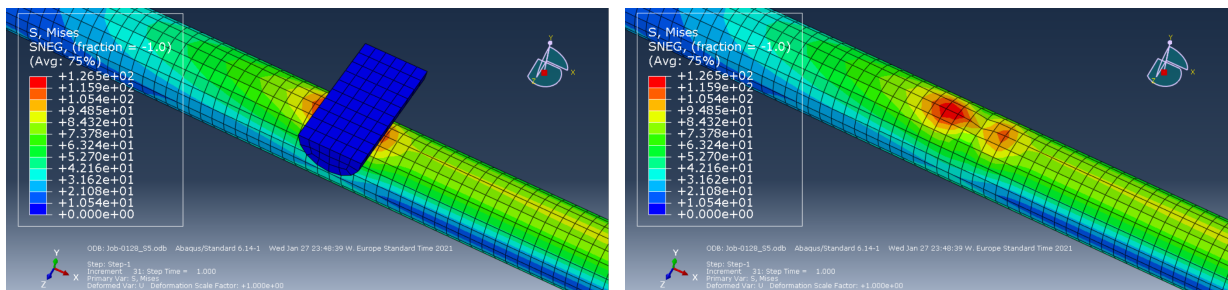


(c) Setting 3 (Maximum Von Mises stress: 117.5 MPa; Center deflection: 2.020mm). (d) Setting 4 (Maximum Von Mises stress: 127.2 MPa; Center deflection: 2.156mm).



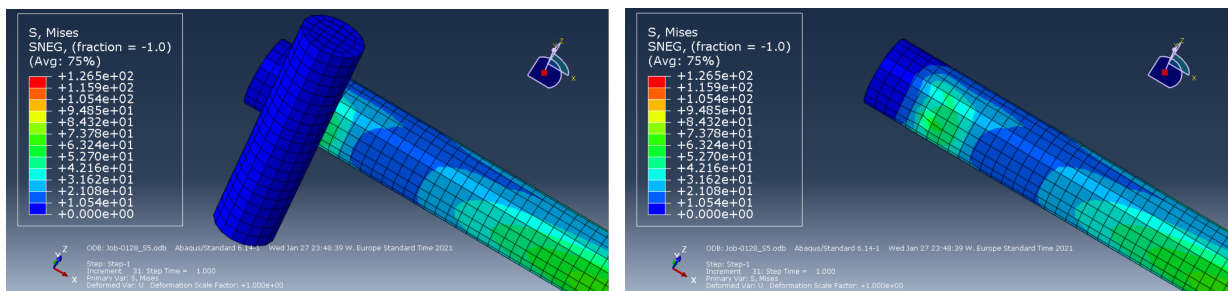
(e) Setting 5 (Maximum Von Mises stress: 126.5 MPa; Center deflection: 2.154mm).

Figure 4.29: The Von Mises stress distributions and deformed shape figures of Setting 1 to Setting 5.



(a) Before load bearings are removed. (b) After load bearings are removed.

Figure 4.30: Von Mises stress distribution at load bearing areas in Setting 5.



(a) Before supports are removed. (b) After supports are removed.

Figure 4.31: Von Mises stress distribution at support areas in Setting 5.

4.4.4 Bending test analysis

In this section, all the simulation results (center deflections at the bottom of the tube) were compared with the lab test (see Table.4.4). Higher deflection represents lower bending stiffness of the tube. Extra value from hand-calculation of the deflection at tube center has been made, which has a deflection of $2.445mm$. The lab test has a center deflection of $2.589mm$.

Several discussions are addressed below:

- In general, the result errors from (Setting 1 to Setting 5) has decrease from -22.9% to -16.8% when compared to lab test.
- The orthotropic behavior has minor impact on the deflection. In setting 2 to setting 3, the deflection reduce 0.1% (from $2.022mm$ to $2.020mm$) and in setting 4 to setting 5, the deflection reduce 0.09% (from $2.156mm$ to $2.154mm$).
- Setting 5 is expected to be the most “well concerned” in regards to the condition considered and should have the closest value compared to the lab test. However, it still has -16.8% difference compared to the lab test. The reasons for this error will be discussed in section.4.4.5.

Table 4.4: The Bending test simulation analysis.

Bending test simulation setting	Result: Tube center deflection	Percentage error (compared to lab exp.)
Lab test	2.589 mm	-
Hand calculation ($t=3.2mm$)	2.445 mm	-5.6%
Setting 1 (S1)	1.996 mm	-22.9%
Setting 2 (S2)	2.022 mm	-21.9%
Setting 3 (S3)	2.020 mm	-22.0%
Setting 4 (S4)	2.156 mm	-16.7%
Setting 5 (S5)	2.154 mm	-16.8%

4.4.5 Bending test conclusions

This section answers the questions from the beginning of this compression test simulation section and gives conclusions and recommendations.

The aims in the beginning of this chapter are:

- See how the orthotropic behavior will influence the simulation.
- Check whether the analysis type, which includes the most factors in the analysis (in this section: Setting 5), acquires the closest value to the lab test.
- Investigate the validity of using derived effective thickness ($t_{eff}=3.01mm$) for incorporating surface roughness.

Findings of the aims, conclusions, and recommendations are listed below:

1. The orthotropic behavior has a minor impact in this bending simulation. In setting 2 to setting 3, the deflection reduce 0.1% (from $2.022mm$ to $2.020mm$) and in setting 4 to setting 5, the deflection reduce 0.09% (from $2.156mm$ to $2.154mm$). However, it shows that the WAAM tube, which considered the orthotropicity, has higher bending stiffness (lower deflection).

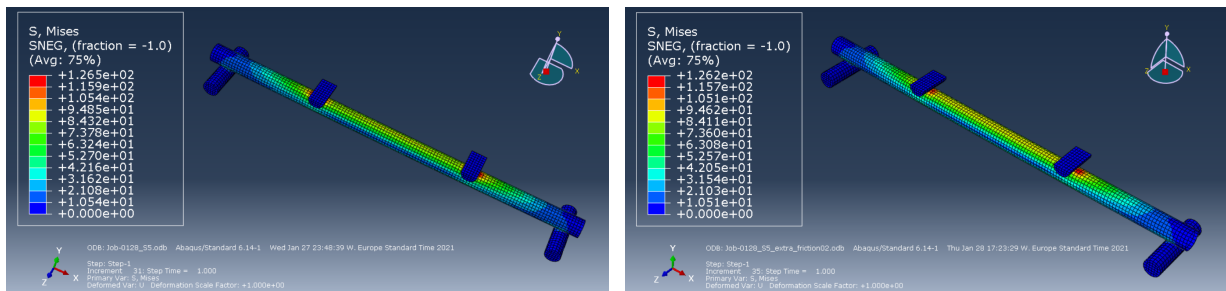
2. The simulation shows reasonable results. The deflection, in general, is getting closer to the lab test when more factors of the imperfections are considered. However, the results are unable to show precise value (when compared to lab test). It seems that a “shift” for all the data exists.

Possible reasons for the shift are discussed below:

- The friction between the tubes: Friction between the tube and bearing did influence the simulation result. Dong et al. [57] studied how friction influence four-points bending test and concludes that: The friction imposes the lateral force acting on the tube. Therefore, the larger the friction exists in between the tubes and the supports, the less deflection will be measured in the experiment.

To examine the influence of the friction, an additional simulation (Setting 5-additional), which lowers the friction coefficient to $\mu=0.2$ in Setting 5, has been carried out to compare with the original friction coefficient of $\mu=0.5$. The results (can be seen in Fig.4.32) shows larger friction indeed has lower deflection, as Dong said. The effect of lower friction leads to the deflection increase 7.3% (from 2.154mm to 2.311mm). At the same time, the error between the simulation and the lab test reduce from -16.8% to -10.7%.

To conclude, the exact friction between the WAAM tube and bearings, the WAAM tube and supports, have to be tested in the lab first as the input for FEA to obtain more precise results.



(a) Setting 5 ($\mu=0.5$; Maximum Von Mises stress: 126.5 MPa; Center deflection: 2.154mm).
 (b) Setting 5-additional ($\mu=0.2$; Maximum Von Mises stress: 126.2 MPa; Center deflection: 2.311mm).

Figure 4.32: Comparison of Setting 5 (friction coefficient $\mu=0.5$) and Setting 5 - additional (friction coefficient $\mu=0.2$).

- Assumed properties of experimental equipment and test setup errors:
 - Some of the properties and dimensions used in the FEA are based on the assumptions. i.e., the material properties and dimensions of the load bearings and supports.
 - The load bearings and supports used in the experiment are in squared shape instead of rounded, which might lead to more force concentrations at the contact faces between the tube and the supports, Thus lead to higher deflections.
 - The setup in the lab test might have small errors in regard to specimens' positioning (few mm errors). However, in the simulation, the placing of the objects are instead very precise.
- Van Bolderen has performed only three test samples. Therefore, the lab test results might cause some concerns.

3. Although a result value shift problem exists in the simulation owing to the data lack of friction coefficient between the bearings, the whole setup still shows the limited error to 16.8% in Setting 5. The simulated results are getting closer to the experimental value when effective thickness are included. This shows the concept of using derived effective thickness works. Therefore, the effective thickness ($t_{ef}=3.01mm$) is still considered suitable and will be used in the further analysis in Ch.5.

4.5 Simulation of Buckling test

In the buckling test simulation, the aims is to:

- Find out the influence of orthotropic material behavior.
- Finding the suitable failure mode from LBA modes.

- Check whether the analysis type, which includes the most factors in the analysis (in this section: Setting 7), acquires the closest value to the lab test.
- Investigate how the lack of straightness influences the strength of the structure.

The overview of buckling test simulation can be seen in Fig.4.33. The settings is presented in Section.4.5.1. The simulation process is shown in Section.4.5.2. This step listed out all the Settings with their analysis types, including the considered factors. In Section.4.5.3 and Section.4.5.4, the buckling load in the simulation will be compared with the lab test results . In Section.4.5.5, conclusions and recommendations will be given.

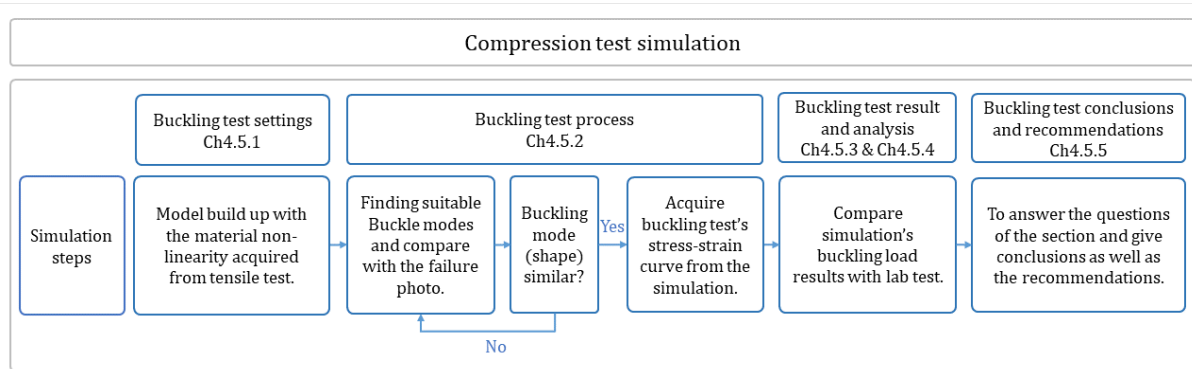
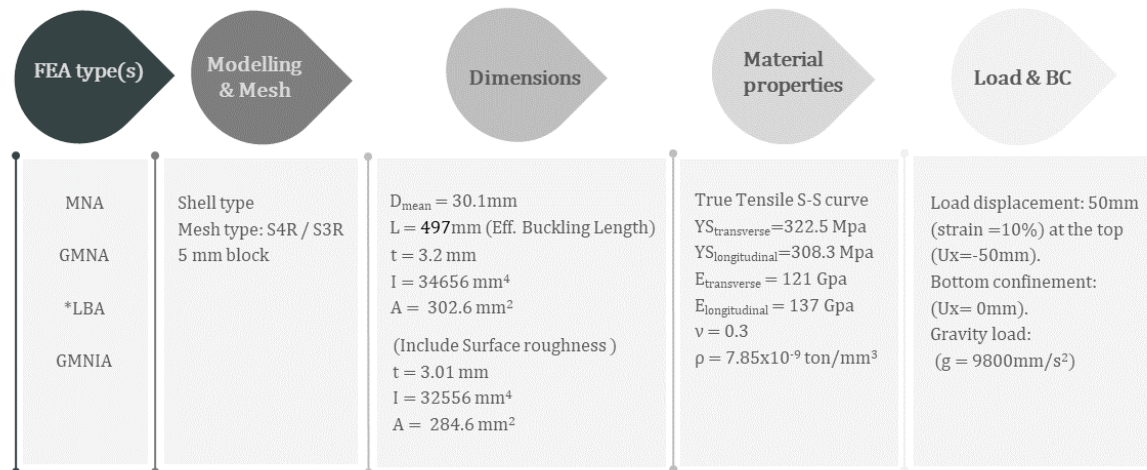


Figure 4.33: The overview of Buckling test simulation methodology.

4.5.1 Buckling test settings

The overview of the buckling test setting is shown in Fig. 4.34.



*LBA is performed for finding buckling modes.

Figure 4.34: Buckling test settings.

- FEA type(s):

The process incorporates three analysis type. MNA, GMNA, and GMNIA. MNA is first presented to get the primary setting and result from the material non-linearity. Then, GMNA was chosen to include the geometrical non-linearity. Last, GMNIA. For material imperfection, orthotropic behavior is considered. For geometrical imperfections, surface roughness and lack of straightness were chosen. The possible deformed shapes (Lack of straightness) were found from the LBA (Linear elastic bifurcation analysis or Linear buckling analysis), and it is incorporated in the model with the scale factor of 0.62. The value comes from the buckling lab test literature review in Section.

3.5. The average lack of straightness measured ($e_0 = L/791$) times the effective length ($L_{eff} = 497mm$) acquires the value of 0.62.

- Modelling & Mesh:

The model is a shell type structure built with $3mm$ blocks with meshes type S4R (4-node general-purpose shell, reduced integration with hourglass control, finite membrane strains) and S3R (3-node triangular general-purpose shell, finite membrane strains).

The modeling of this tube uses the effective length tube of $497mm$ (including two bolts' thickness) instead of the tube length of $690mm$ (shown in Fig.4.35). The bolts with a thickness of $20mm$ and radial thickness of $15mm$ at two tube ends are also considered. Ball bearings at two sides of the tube are modeled in ABAQUS by linking the movement of the tube end with the center point (shown in Fig.4.36 (a)), which is considered as the center of the ball bearing.

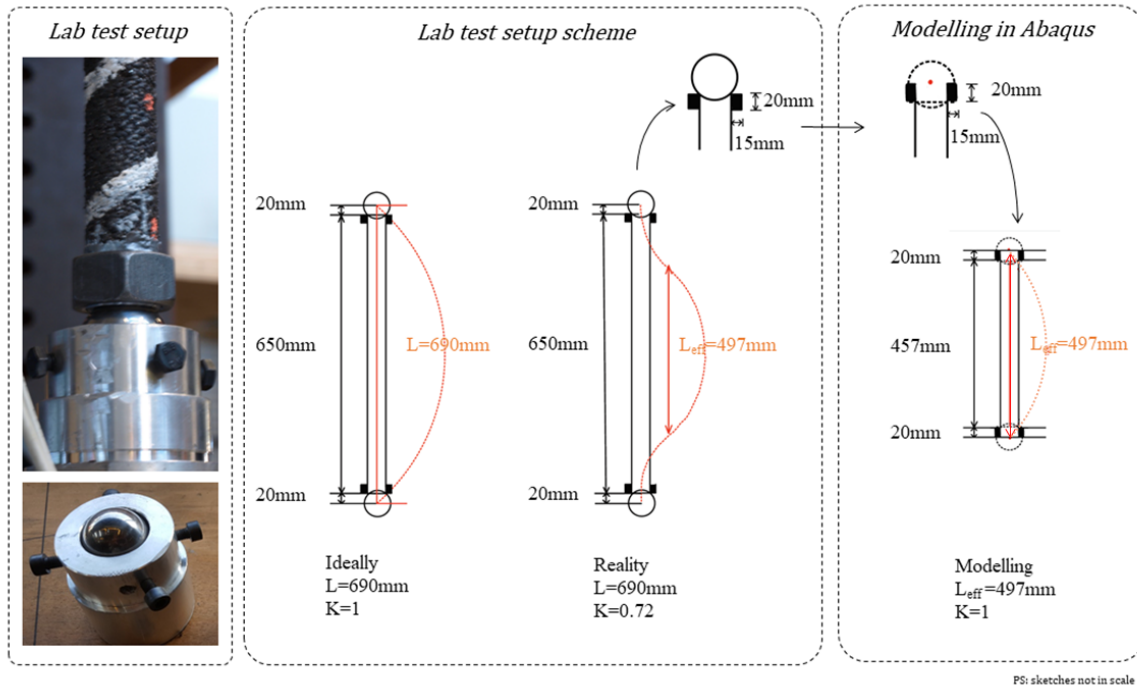


Figure 4.35: Buckling test modelling.

- Dimensions:

Three specimens in the buckling test have the nominal diameter and wall thickness of $30.1mm$ and $3.2mm$. The average effective length ($L_{eff}=497mm$) is taken as the tube length. The effective thickness derived from the lab test is $3.01mm$. (see Section 3.4.2 for the derivation.)

- Material properties:

The true stress-strain curve in the transverse direction is considered as the main direction due to the printing direction of the tube. The longitudinal directions were used in building up the orthotropic material in the linear part. The Yield stress (YS) in the transverse direction is $322.5 MPa$ and in the longitudinal direction is $308.3 MPa$. Young's modulus (E) in the transverse direction is $121 GPa$ and in the longitudinal direction is $137 GPa$. Poisson's ratio (ν) is 0.3 . The density (ρ) of the material is $\rho=7.85 \cdot 10^{-9} ton/mm^3$.

- Load & BC:

The sample in ABAQUS is compressed for $50mm$ (10% of the total length; total effective length = $497mm$). In the setting, the load-displacement at the sample top is set to $50mm$ ($U_x=-50mm$), and the displacement at the sample bottom is $0mm$ ($U_x=0mm$). Both are applied to two ball

bearings' geometrical center (Fig.4.36 (b)(c)) to simulate the rotation of the ball. Gravity load with the acceleration of $9800\text{mm}/\text{s}^2$ is also added to the system.

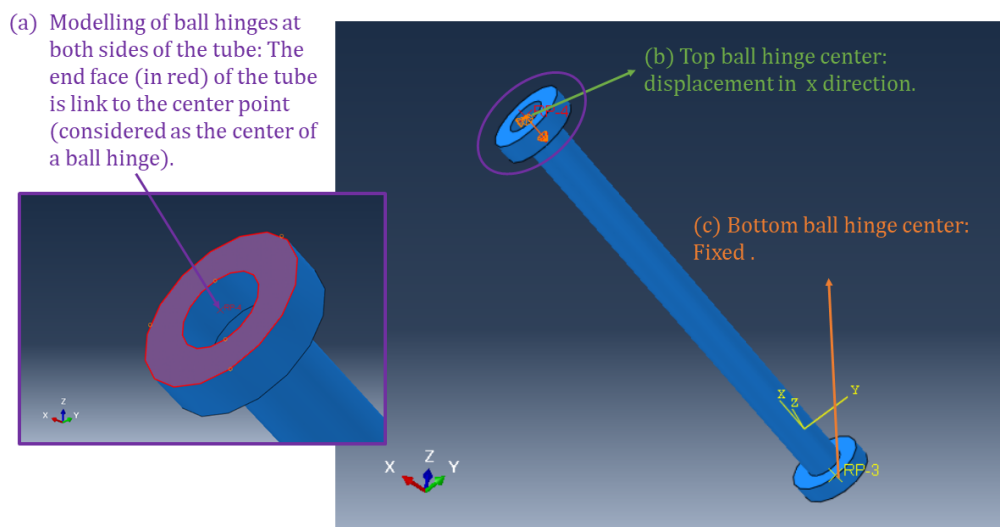


Figure 4.36: Buckling test boundary conditions.

4.5.2 Buckling test process

Settings with different analysis types and imperfections are listed in Fig.4.5. The transverse printed direction is chosen because it is the direction that matches the printing direction of this tube.

Table 4.5: The Buckling test simulation setting list.

Buckling test simulation setting lists	Analysis type	Geometrical imperfection	Material imperfection
Setting 1 (S1)	MNA	No	No: Isotropic
Setting 2 (S2)	GMNA	No	No: Isotropic
Setting 3 (S3)	GMNIA (Material imperfection only)	No	Yes: Orthotropic
Setting 4 (S4)	GMNIA (Geometrical imperfection: Surface roughness)	Yes: Surface roughness	No: Isotropic
Setting 5 (S5)	GMNIA (Material imperfection + Geometrical imperfection: Surface roughness)	Yes: Surface roughness	Yes: Orthotropic
Setting 6 (S6)	GMNIA (Geometrical imperfection: Surface roughness & Lack of straightness)	Yes: Surface roughness +Lack of straightness	No: Isotropic
Setting 7 (S7)	GMNIA (Material imperfection + Geometrical imperfection: Surface roughness & Lack of straightness)	Yes: Surface roughness +Lack of straightness	Yes: Orthotropic

In between the simulation process, the LBA was performed to find the more realistic failure (shapes) modes for the compression test.

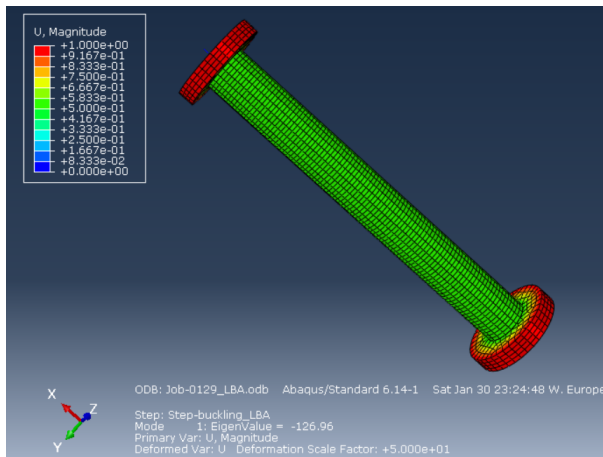
The LBA was performed to find possible failure modes for buckling simulation. In setting 1 to 4, which

doesn't considered about the global geometric imperfection (Lack of straightness), the deformed shapes are unrealistic (see Fig.4.39 (a) to (d)) when compared to the buckling lab test failure (see Fig.4.38), which shows only one curvature and has the largest deflection at the middle.

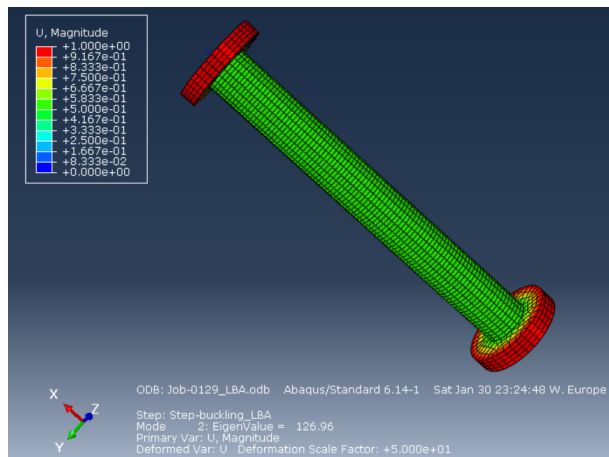
The top 8 possible LBA modes are shown in 4.37. Deformed scale factors are all set to 50 to clearly show deformation shapes. Mode 2 is identical with mode 1, but with a shift in angle. However, the linear buckle load in mode 1 shows a minus value, making the top 2 modes invalid.

Mode 4 is also identical to mode 3 as well. Since the deformed shape coincides with the lab test deformed shape, mode 3 and mode 4 are used as the geometrical imperfection (Lack of straightness) in the lab test buckling simulation. As for mode 5, 6, 7, and 8, high linear buckle load, as well as different buckle shape, make these modes the least possible choices.

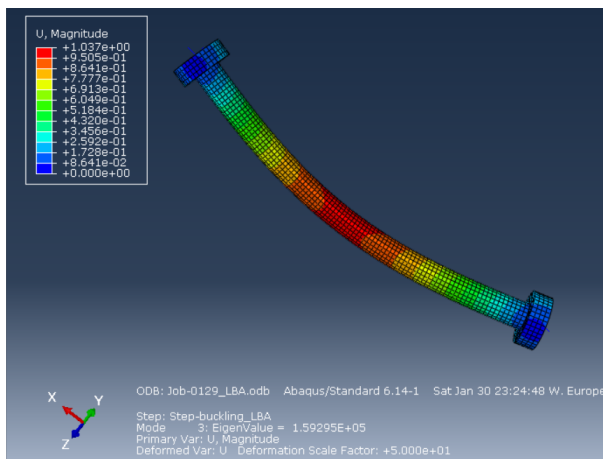
Simulation results in Setting 6 and 7 (shown in Fig.4.39 (f) and (g)) incorporate the geometrical imperfection (lack of straightness) from the LBA's third mode (mode 3).



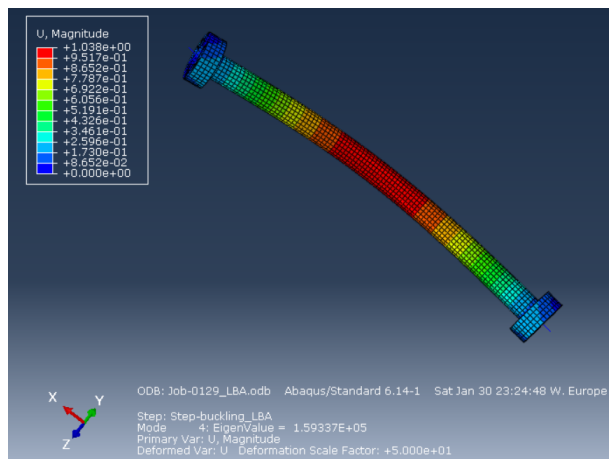
(a) LBA mode 1. (Linear buckling load = -127.0 KN)



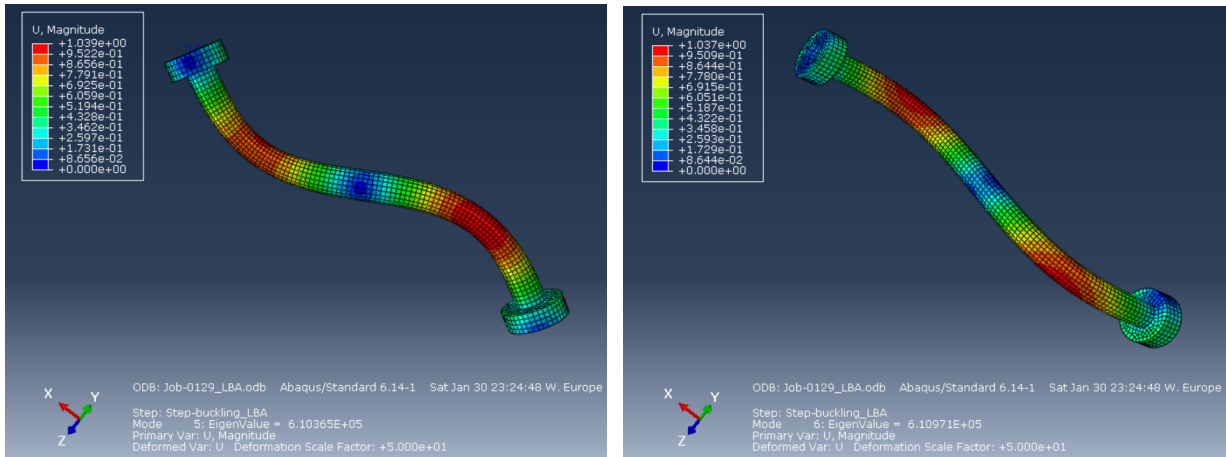
(b) LBA mode 2. (Linear buckling load = 127.0 KN)



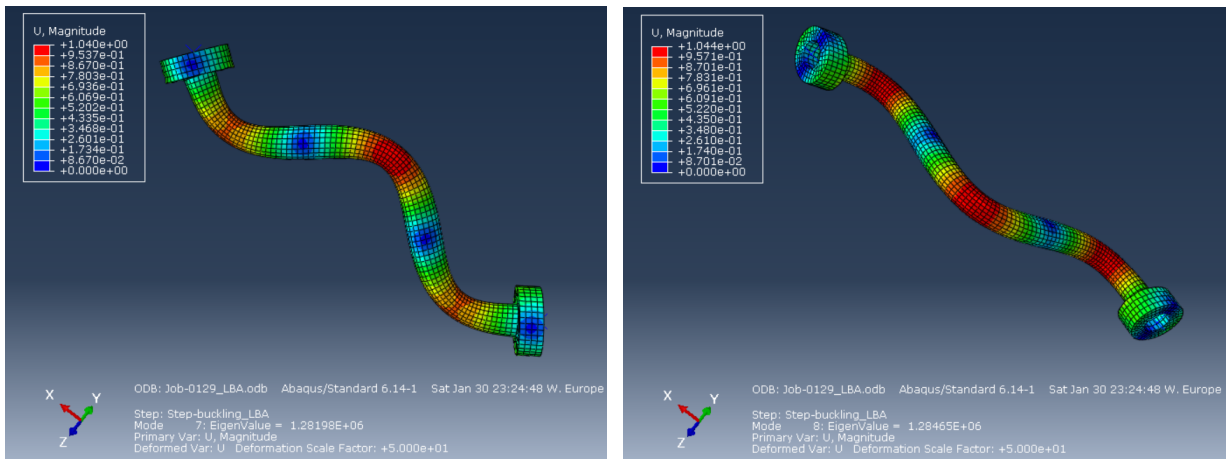
(c) LBA mode 3. (Linear buckling load = 159.3 KN)



(d) LBA mode 4. (Linear buckling load = 159.3 KN)



(e) LBA mode 5. (Linear buckling load = 610.4 KN) (f) LBA mode 6. (Linear buckling load = 611.0 KN)



(g) LBA mode 7. (Linear buckling load = 1282.0 KN) (h) LBA mode 8. (Linear buckling load = 1284.7 KN)

Figure 4.37: Possible buckling failure modes found in LBA ((a) to (h): mode 1 to mode 8).



Figure 4.38: The specimen shape after buckling lab test.

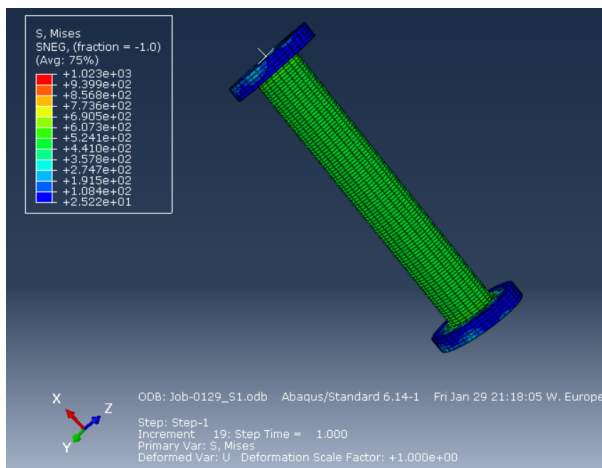
4.5.3 Buckling test results

Buckling test simulation result figures:

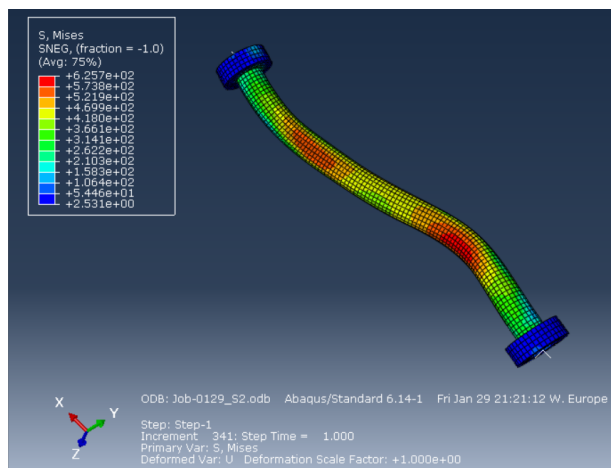
Buckling simulation result figures in ABAQUS are shown in Fig.4.39. Deformation scale factor is 1. The compression test has a load displacement setting of 50mm (strain = 10%).

Observations of deformed shapes are listed:

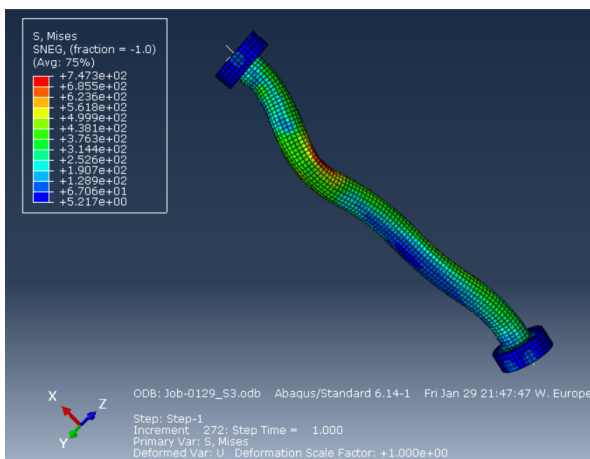
- With only material non-linearity included (GMNA), Setting 1 deformed only in the axial direction (the length is getting shorter), which is very unrealistic.
- With geometrical non-linearity considered, Setting 2 to Setting 7 show signs of geometrical deformation. However, the settings without the inclusion of lack of straightness shows arbitrary deformed shapes, and are less likely to happen. i.e. Setting 2 (Fig.4.39 (b)) deforms like mode 5 (same as mode 6) (Fig.4.37 (e) and (f)), which has higher linear buckling load than mode 2 and mode 3; Setting 4 (Fig.4.39 (d)) deforms like mode 7 (same as mode 8) (Fig.4.37 (g) and (h)), which has way higher linear buckling load among all the modes.
- The inclusion of lack of straightness found from LBA (mode 3) makes the deform shapes of Setting 6 and Setting 7 look realistic. Also, the linear buckling load of this mode is the lowest.



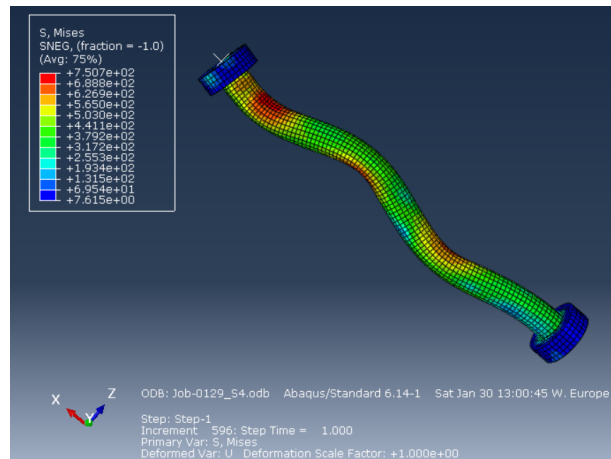
(a) Setting 1.



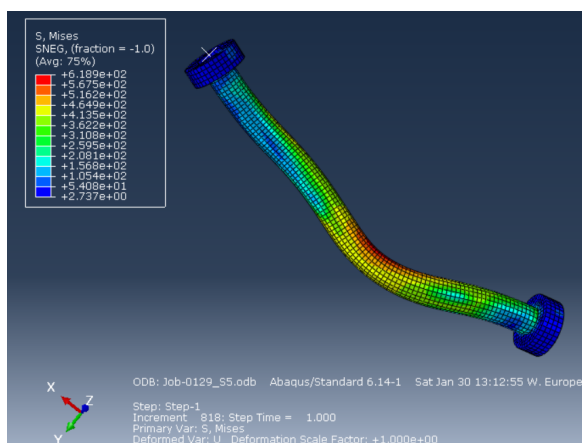
(b) Setting 2.



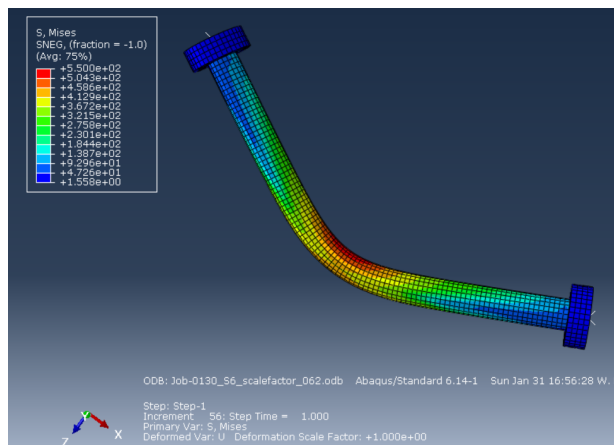
(c) Setting 3.



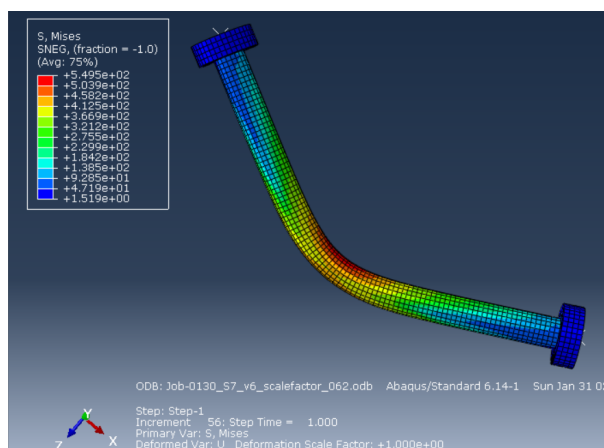
(d) Setting 4.



(e) Setting 5.



(f) Setting 6.



(g) Setting 7.

Figure 4.39: Buckling test deflection result figures of Setting 1 to Setting 7.

Buckling test simulation stress-strain curves:

The result (output) of the buckling simulations is the buckling stress-strain curves. To plot the uniaxial stress-strain curve, the reaction force in the axial direction was gathered from the ball hinge center at one side of the tube and correlate with the strain. All curves are shown in Fig.4.40.

Several findings from buckling stress-strain curve results are addressed below:

For Yield stress and Buckling stress:

- In general, the yield stress does not affect much by the increasing complexity of the analysis factors until the lack of straightness is included.
- The inclusion of lack of straightness influence the slender structure's stability. Buckling occurred before the yield stress was reached. The scale factor for lack of straightness is 0.62 (see Section.4.5.2). The buckling stresses for Setting 6 and Setting 7 are $249.7N/mm^2$ and $249.8N/mm^2$. The buckle loads for Setting 6 and Setting 7 are both 71.1kN.
- The influence of the material imperfection (Orthotropicity) is minimal. From Setting 2 to Setting 3, the inclusion of material imperfection makes the yield strength increase from 323.6 MPa to 326.1 MPa, which is 0.77% higher; From Setting 4 to Setting 5, the yield strength decrease from 326.3MPa to 321.9 MPa, which is 1.37% drop; From Setting 6 to Setting 7, the inclusion of material imperfection makes the buckling strength increase from 249.7 MPa to 249.8 MPa, which is 0.04% higher.

For Ultimate stress:

- Arbitrary deformations lead to the uncertain ultimate stress points after yield stress or buckling stress points have been reached. The ultimate stresses are unrealistic to obtain in the lab test with slender columns. Presenting of these value are for comparison purposes.

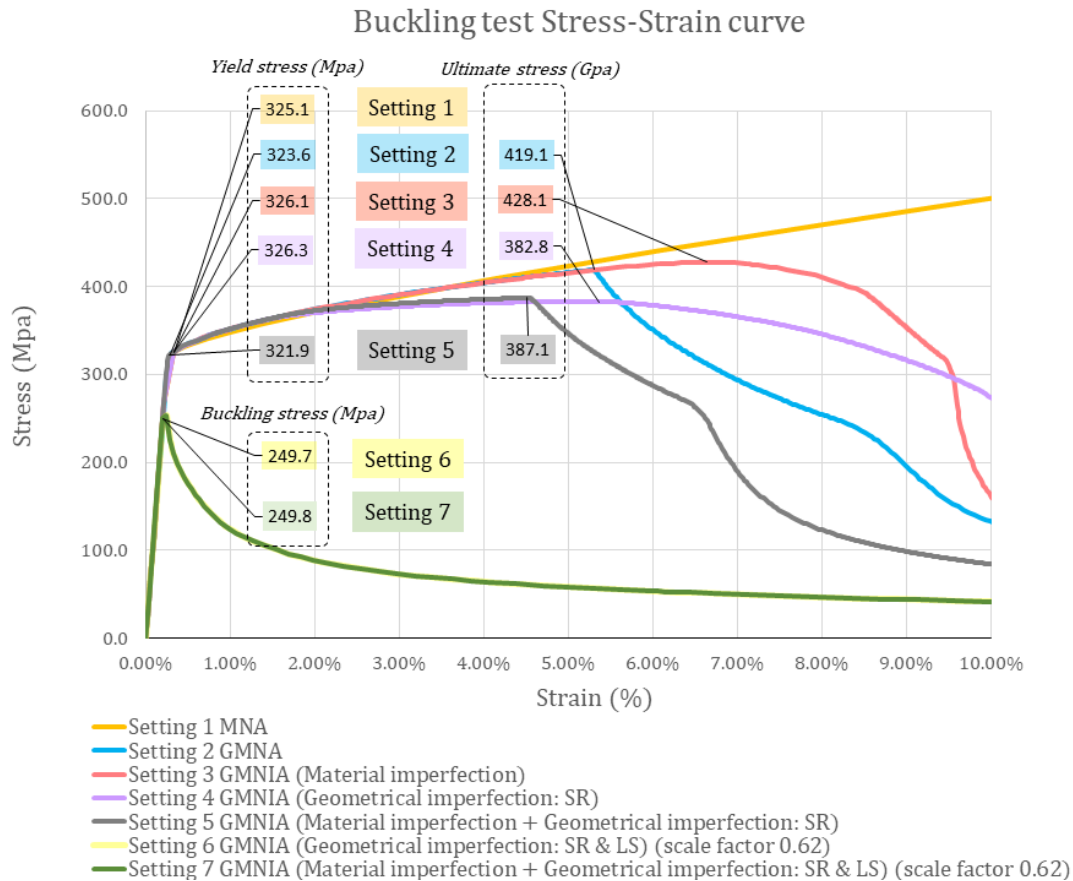


Figure 4.40: Buckling test results

4.5.4 Buckling test analysis

In this section, ultimate failure loads and buckling loads from the numerical simulation are compared to the buckling lab test in Table.4.6. Ultimate failure loads or buckling loads are acquired from each setting's stress times the cross-sectional area. The lab test result has an average buckling load of 52.7KN.

Several discussions are addressed below:

- Settings without the lack of straightness (Setting 1 to Setting 5) have failures after the yield stress reached, which lead to unrealistic high failure loads. When compared to the lab test, the errors are between 70% to 90%.
- Settings which include the lack of straightness (Setting 6 and Setting 7) reduced buckling load differences to around 35% when compared to the lab test.

Table 4.6: Buckling test analysis.

Buckling test simulation settings	Result: Yield stress or buckling stress (Mpa)	Cross-sectional area (mm ²)	Result: Ultimate failure load (KN)	Result: Buckling load (F _{buc}) (KN)	Failure load percentage error (compare to lab exp)
Lab test	-	-	-	52.7	-
Setting 1 (S1)	325.1	302.6	98.4	-	86.7%
Setting 2 (S2)	323.6	302.6	97.9	-	85.8%
Setting 3 (S3)	326.1	302.6	98.7	-	87.2%
Setting 4 (S4)	326.3	284.6	92.9	-	76.2%
Setting 5 (S5)	321.9	284.6	91.6	-	73.8%
Setting 6 (S6)	249.7	284.6	-	71.1	34.8%
Setting 7 (S7)	249.8	284.6	-	71.1	34.9%

The influence of scale factors (for lack of straightness) on the buckle loads has been observed in the analysis. Larger scale factors lead to lower buckling loads. Extra simulations with different scale factors in Setting 7 have been performed to understand their relations. The result is shown in Fig.4.41, and the scale factor analysis is shown in Table.4.7.

Several discussions are addressed below:

- Buckling loads are very sensitive to geometrical imperfections. It can be inferred in Fig.4.41 that a slightly increase (0.1% to 0.2%) of lack of straightness can lead to several percentage error drop of buckling load while comparing with lab test.
- Fig.4.41 shows that the buckling load decrease while the lack of straightness (scale factor) increase.
- From the buckling lab test value (buckling load = 52.7KN), the scale factor in the numerical simulation should be between 3 to 4 (Table.4.7). The 3 to 4 mm deviates from the center of the tube result in the lack of straightness of $e = 3L/497$ to $4L/497$. The values are between 4.77 times to 6.37 times larger than the average lack of straightness measured in the lab test ($e = L/791$).

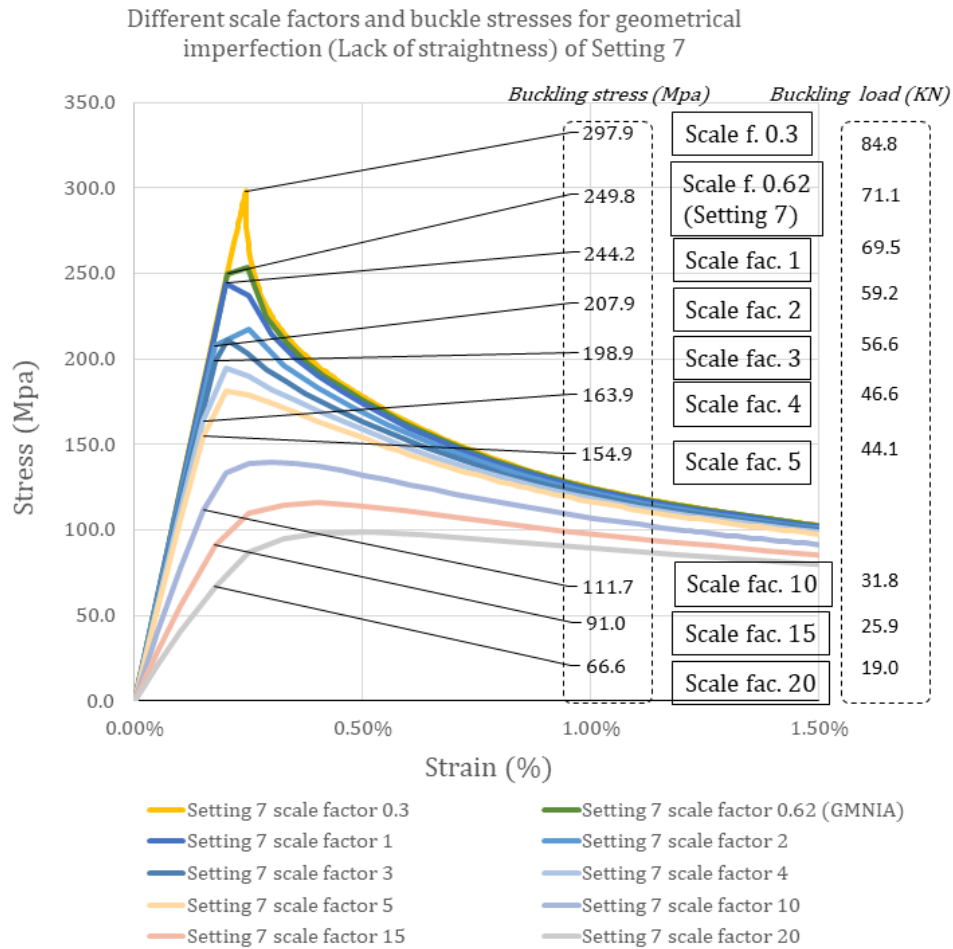


Figure 4.41: Different scale factors and buckling stresses for geometrical imperfection (Lack of straightness) of Setting 7.

Table 4.7: Scale factor analysis.

Different scale factors of Setting 7	Lack of straightness (%)	Result: Yield stress or buckling stress (Mpa)	Cross-sectional area (mm ²)	Result: Buckling load (F_{buc}) (kN)	Failure load percentage error (compare to lab exp)
Lab test		-	-	52.7	-
Scale factor 0.3	0.06%	297.9	284.6	84.8	60.9%
Scale factor 0.62 (Setting 7)	0.12%	249.8	284.6	71.1	34.9%
Scale factor 1	0.20%	244.2	284.6	69.5	31.9%
Scale factor 2	0.40%	207.9	284.6	59.2	12.3%
Scale factor 3	0.60%	198.9	284.6	56.6	7.4%
Scale factor 4	0.80%	163.9	284.6	46.6	-11.5%
Scale factor 5	1.00%	154.9	284.6	44.1	-16.3%
Scale factor 10	2.00%	111.7	284.6	31.8	-39.7%
Scale factor 15	3.00%	91.0	284.6	25.9	-50.9%
Scale factor 20	4.00%	66.6	284.6	19.0	-64.0%

4.5.5 Buckling test conclusions

This section answers the questions from the beginning of this compression test simulation section and gives conclusions and recommendations.

The aims in the beginning of this chapter are:

- Find out the influence of orthotropic material behavior.
- Finding the suitable failure mode from LBA modes.
- Check whether the analysis type, which includes the most factors in the analysis (in this section: Setting 7), acquires the closest value to the lab test.
- Investigate how the lack of straightness influences the strength of the structure.

Findings of the aims, conclusions, and recommendations are listed below:

1. Orthotropic behavior has a minor influence on the strength of buckling stress. From Setting 4 to Setting 5, the buckling stress decreases 1.36% from 326.3MPa to 321.9MPa; From Setting 6 to Setting 7, the buckling stress increases only 0.04% from 249.7MPa to 249.8MPa.
2. Failure mode 3 from LBA has been found. It is suitable because it matches the lab deflection shape, which is a bow-like shape, with the lab experiment. Also, it is the mode with the lowest linear buckling load.
3. Results from settings show closer value when more geometrical imperfections are included. The implementation of effective thickness for surface roughness (Setting 4 and Setting 5) reduce around 10% to 15% of the error compared to the lab test (57.2KN), and the inclusion of effective thickness with lack of straightness (Setting 6 and Setting 7) reduce roughly 40% of the error and results in the final error of around 35%.
4. The lack of straightness drastically influences the buckling load of the slender structure. Buckling loads are very sensitive to geometrical imperfections. Few fractions of percentage increase (0.2% to 0.4%) of lack of straightness can lead to several percentage error drop (19.6%) of buckling load compared to the lab test result.
5. High buckling load error (around 35%) between the numerical simulation (Setting 7) appears to happen.

The measured lack of straightness ($e = L/791$; scale factor = 0.62) in the simulation shows the column's buckling load is 71.1KN, whereas the lab test has the buckling load of 52.7KN.

The higher buckling load appears in the simulation could come from:

- The measured lack of straightness is too less. Scale factor analysis was performed and showed the scale factors in the numerical simulation, with all the defined parameters, are between 3 to 4 ($e = 3L/497$ to $4L/497$ or can be written as $e = L/166$ to $L/124$). The simulation results are between 4.77 times to 6.37 times larger than the average lack of straightness measured in the lab test ($e = L/791$). For comparison, the experimental result from Langhi shows the lack of straightness is around $L/1000$, and the maximum value at around $L/300$ [53]. It has to be noticed that the lack of straightness provided by Langhi is the deviation along the printed tube from the center axis. Langhi's result indicates that the lack of straightness measured by Van Bolderen is more reasonable than the simulation results.
- The effective thickness derived from the lab test might be thicker. The derivation of the effective thickness is based on the average value measured from three lab tests. The actual effective thickness could be larger and lead to a slightly larger buckling load.
- The simplification of the geometrical imperfections included in the model. Only global geometrical imperfections (surface roughness and lack of straightness) are included in the simulation, and the local geometrical imperfections were left out due to the lack of data. Therefore, the simulation underestimates the imperfections in the model and leads to a higher buckling load.

4.6 Conclusions

The aim of this chapter is to verify the parameters and assumptions in the analysis and collect them for the use in the WAAM connection design and analysis chapter (Ch.5).

This section provides the answers to the research questions of this chapter:

- 1) Do simulation results show the numerical simulation reliable?
- 2) How can the precision of simulations be improved? What parameters are lacking for performing the simulations?
- 3) What imperfections are included? And how can the imperfections be used to design the joint further and predict its strength?

The above questions are answered by each of the lab test's numerical simulations.

Tensile test simulation

The input data from the lab test is the material non-linearity.

The simulation result is reliable since the output results of the tensile test simulations (tensile stress-strain curves) are close to the lab results (engineering stress-strain curve).

In the comparison, all setting's maximum errors have been presented. Young's modulus in transverse and longitudinal printed direction are 0.36% and 0.29%; The maximum error of yield stress in transverse and longitudinal printed direction are 0.46% and 0.33%; The maximum error of ultimate stress in transverse and longitudinal printed direction are 0.46% and 0.33%.). Therefore, proving that the material non-linearity data has been used correctly in the FEA software.

Also, there are no geometrical imperfections from WAAM because the samples are milled or conditions that will make the specimen unstable i.e.buckling effect. Therefore, the precision is relatively high for this simulation.

The orthotropic behavior has barely any influence in the tensile test simulation. The yield stress increase 0.03% from Setting 3 (321.5MPa) to Setting 5 (321.6MPa), and decrease 0.03% from Setting 4 (307.4MPa) to Setting 6 (307.3MPa). The ultimate stress increase 0.02% from Setting 3 (565.4MPa) to Setting 5 (565.5MPa), and the same in Setting 4 and Setting 6 (542.2MPa). The young's modulus is the same from Setting 3 to Setting 5 and Setting 4 to Setting 6.

Compression test simulation

Successful compression test simulation should show a close stress-strain curve to the tensile test stress-strain curve before the yield point [53], and the numerical result reflects the success. When compare the numerical result (Setting 5) to the transverse tensile stress-strain curve (322.5 MPa; 121GPa) until the yield point, the yield stress in the simulation only has 1.8% error, and young's modulus only has 0.41% errors. Therefore, the FEA's compression stress-strain curve is considered reliable.

Laghi's research conclusion, instead of Van Bolderen's lab test results, has been used to evaluate the validity of the simulation because the data from Van Bolderen's thesis contains strain measuring errors that lead to the lower young's modulus result of the tested sample.

The reason of the low young's modulus comes from the incorrect strain measured from the experiment. The strain was measured directly from the displacement of the machine instead of the sample. Therefore, the displacement of the dentation on the bearing plate is also counted as a part of the strain. A larger value of strain thus leads to a lower young's modulus of the material. To acquire a more precise strain value, the use of strain gauges is recommended.

The orthotropic behavior does not show a noticeable difference. For the yield stress, Setting 4 and Setting 5 possess the same value, and for Setting 2 to Setting 3, the value drop 0.78% (from 323.7MPa to 321.2MPa). As for the young's modulus, Setting 4 to Setting 5 have the same value and the value from Setting 2 to Setting 3 increases 0.08% (121.0GPa to 121.1GPa).

The inclusion of geometrical imperfection found from the LBA, which is assumed to have a scale factor of 0.2, shows that the inclusion yields a more realistic result. Since the value after the yield point is not

the focus in this simulation, no other scale factors for the imperfection have been tried. The relations between the buckling loads and the scale factors will be discussed in the buckling test simulation (in Section.4.5), which has a more slender sample and prone to geometrical imperfections.

Bending test simulation

The simulated deflections at the center of the tube have around 17% errors compared to the lab test. Except for the unknown properties of experimental equipment and minor measuring or positioning errors in the lab experiment, the unknown friction coefficient has been identified as the most critical problem.

The effect of lower friction leads to the increase of deflection. In bending simulation (Setting 5), the reduce of friction coefficient from $\mu=0.5$ to $\mu=0.2$ makes the deflection at the tube center increases 7.3% (from 2.154mm to 2.311mm). At the same time, the error between the simulation and the lab test reduces from 17% to 10.7%. Therefore, for future testing, the friction between the WAAM tube and bearings, the WAAM tube and supports, have to be tested in the lab first to obtain more precise results.

Although a result value shift problem exists in the simulation owing to the data lack of friction coefficient between the bearings, the whole setup still shows the limited error to around 17%. This shows the concept of using derived effective thickness works. Therefore, the effective thickness ($t_{eff}=3.01mm$) is still considered suitable and will be used in the further analysis in Ch.5.

Buckling test simulation

The buckling simulation result, which includes all the imperfection factors (Setting 7), shows that the buckling load is very sensitive to the lack of straightness. Few fractions of percentage increase (0.2% to 0.4%) of lack of straightness lead to several percentage errors' drop (19.6%) of buckling load compared to the lab test result. Also, the simulated buckling load (71.1KN) has a 35% error compared to the average buckling load of the lab test (52.7KN). The higher buckling load appears in the simulation could come from:

- The measured lack of straightness is too less. The hand measuring of the lack of straightness in the lab experiment might contain a few mm of errors.
- The real effective thickness could be thicker than the derived value from the lab test.
- The simplification of the geometrical imperfections included in the model. Local geometrical imperfections are not included and the analysis of using 3D scanning as the tube's FEA model might help to get a more precise result.

The use of hollow WAAM printed tubes for resisting compression loads should be taken extra attention because of its sensitivity to minimal geometrical imperfections.

For the orthotropicity of the material, it has a minor influence on the strength of buckling stress. From Setting 4 to Setting 5, the buckling stress decreases 1.36% from 326.3MPa to 321.9MPa; From Setting 6 to Setting 7, the buckling stress increases only 0.04% from 249.7MPa to 249.8MPa.

Chapter 5

Strength prediction of proposed WAAM joints

This chapter aims to use the advantage of WAAM to design joints for grid shell structures, which are challenging to produce traditionally, and provide their strength prediction regarding the joint stiffness and the moment capacity. The examined material data and defined imperfections from the components' lab test simulations (in Ch4) are used. Also, the design and the joint setup are planned in a way that the examination of the joint's strength is reasonable and straightforward for future lab experiments (future work).

Research questions in this chapter are:

- 1) How do simulations of four lab experiments help with the strength prediction of the joint?
- 2) How does the designed joint performs in regards to the stiffness and the moment capacity?
- 3) How can the joint be improved?

5.1 Joint design

With more drastically designed structures have been invented to realize the architectural representation, complex joints in the structure have lead to complicated production scenario and higher needs for skilled labor. The WAAM process has the potential to make the production of joint more precise and versatile in shape with its automatic capability and production nature, and it all has to start with a joint design that brings up the WAAM's advantage.

Five aims for designing the gridshell joint are:

1. Moment resistant: designed from the joints that has good moment-resisting capability.
2. Flexibility: Flexible enough to provide various angles for connecting members.
3. Methodology wise: Designed a simple and reasonable joint for the future lab experiment to examine the joint's strength.
4. Apply the advantage of WAAM.
5. Manufacturable.

Five actions for developing WAAM gridshell joint have been made to fulfill five above mentioned aims in Fig.5.1. Details of the aims and actions are addressed in the following subsections.

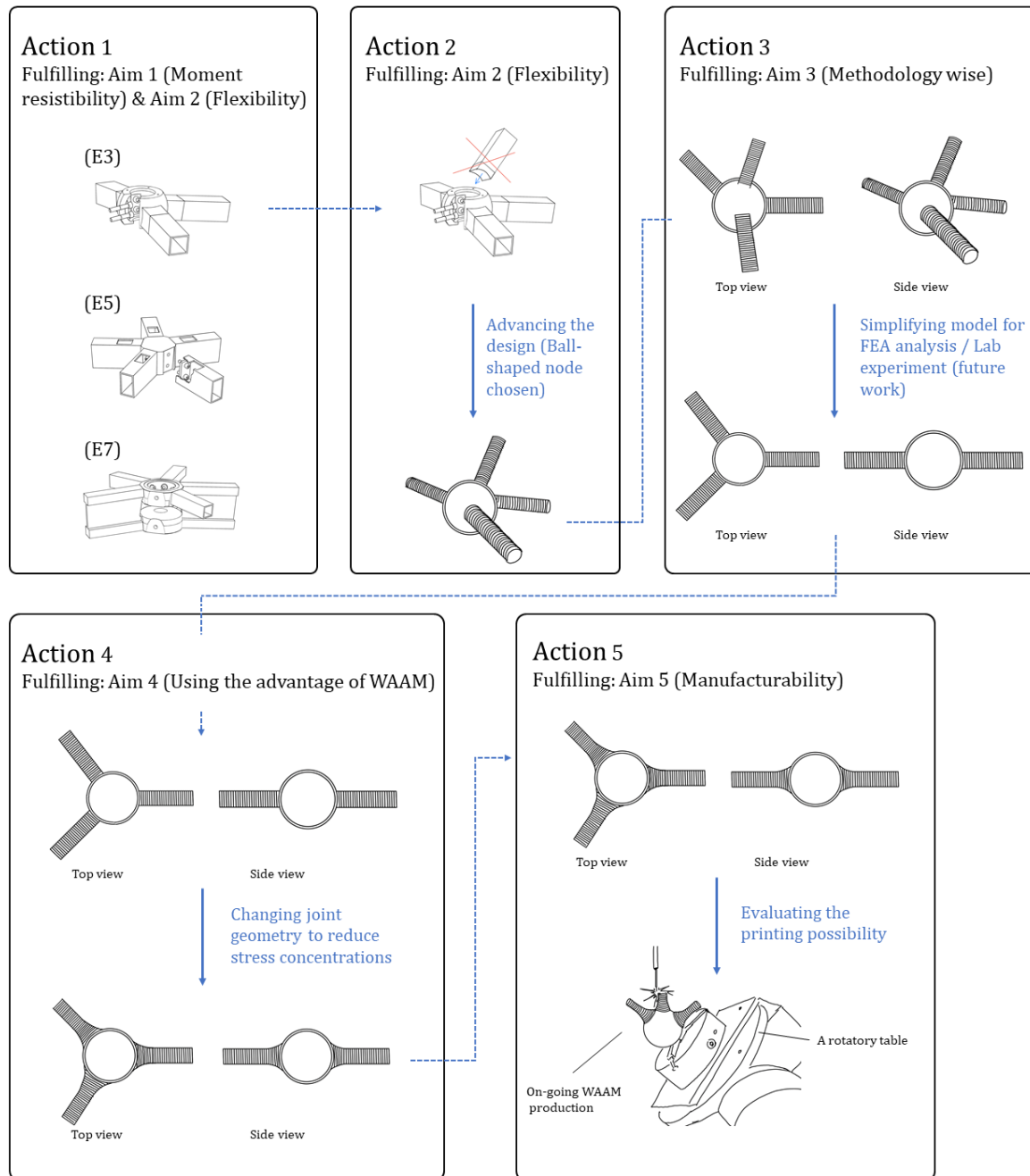


Figure 5.1: The joint design overview.

Action 1: Joint requirements and design criteria in respect to moment resistance and the flexibility of connecting

The first action (see Fig.5.1, Action 1) selects several model types, which fulfill aim 1 and aim2, as the sample for developing a proposed joint.

Three types of joints (E3, E5, E7/8) were picked as the initial design samples due to their high moment resistance and flexibility.

From the studies of joint types in Section.2.3.1, it shows that end-face joints are more flexible in fitting different types of gridshell structures. Also, the moment resistance is generally higher. Flexible in this way means the horizontal angle, vertical angle, and twist angle can be maneuver easily to suit the need for multiple angle requirements.

From the Table.2.5 in Section.2.3.1, the comparison shows that end-joint types: E3, E5, E7/8 has better flexibility (at least two out of three "+" for accommodating local geometry). Also, the performance regarding the transferring of normal force and bending moment is high (at least two out of three "+" for transferring internal forces). Moreover, the applicable structural types for these joints require no structural and geometrical optimization.

The sufficient bending moment comes from the sufficient thickness (adequate lever arm) of the node (jointing part). It can be comprehended from the difference between E7/8 and E6; the double disk design enlarges the level arm at the node to resist bending moment.

The higher flexibility of joints come from the adjusting ability of the member connecting face at the node (the slicing off the node to reach the desired angle, this happens in joint E5 and E7/8). This makes the production of unique nodes complicated and costly. However, the joint E3 creates an efficient and brilliant idea by using a hollow sphere as a node to accommodate members coming from all different angles. Therefore, it becomes the design sample of the proposed joint.

Action 2: Advancement of the chosen joint

Action 2 settles down the joint's basic design shape from the selected joint E3 and improves its flexibility.

The characteristics of the E3 are:

- It equipped a sphere shape node with openings at the top and the bottom.
- The diameter (height) of the node is large enough to give a sufficient level arm for resisting bending moment.

However, the sphere node of the end-joint E3 can't satisfy the need of the members connecting from the top or bottom part (see Fig.5.1, Action 2). To enhance the flexibility (aim 2) of the proposed joint, the open sphere node is replaced by a casted hollow ball node. WAAM printed members will then be welded to the hollow ball node to create a welded joint. This idea comes from the literature review of a TU Delft glass swing research and can be seen in Section.2.1.5 (Fig.2.12).

Action 3: Methodology wise

The flexural performance will be analyzed for the proposed joint (the analysis is presented in Section.5.2). For the thesis research purpose, the joint is simplified (the experimental planning and design ideas of the joint are developed from the review of moment-resistant joint research in Section.2.3.3). Connected funnel-shaped members, which are WAAM printed to the ball node, are decreased to three legs. Also, all members are horizontally laid (see Fig.5.1, Action 3). The reason for using three legs is that the dimensions of the existing casted hollow ball node provided in the literature review have a diameter of around 100mm, which can only fit three printed legs. It is possible to have a larger casted hollow ball node to fit more printed legs in different angles. However, the settings with three legs printed horizontally have been decided in this research.

The sample dimensions in the lab test were taken as the design reference of the WAAM printed legs, which have cross-sectional areas that are similar to the WAAM lab test' samples (a nominal thickness of 3.2mm and a circular diameter of 30.1mm (middle to the middle surface)).

Action 4: The joint modification by considering the advantage of WAAM process

The joint type from Action 3 can be further improved by increasing the cross-sectional area of the connected members. The diameter of the modified member increases gradually while the distance to the node is getting closer (dimensions and design details are presented in Section.5.2). The improvement is made from the observation of the joint failure experiment in Section.2.3.3 as a method to shift the stress concentration away from the ball node and prevent rupture failure at the welds. Also, smoother printing geometry can probably avoid and reduce the fatigue of the joint.

Action 5: Production possibility and strategies

The manufacture of this funnel shape WAAM part printed on the casted ball node is possible with the help of a rotatory table (the possible production methodology can be seen in Section.2.1.5). This makes

each member's printing (the layering of the welds) be consistently vertical during the whole printing process.

The production of stiffeners in the WAAM printed funnel shape parts can be incorporated in the joint's printing path, and the nature of the WAAM process enables the realization of the above-mentioned characteristics.

5.2 Joint strength prediction

The moment-rotation curve is presented in this section to give the stiffness and the moment capacity of the joint for joint strength classification capacity at its setup conditions.

5.2.1 Analysis idea and setting list

Three joint types have been planned for strength prediction (Fig.5.2). Joint 1 is the original joint that has hollow funnel-shaped WAAM printed parts with no stiffeners. Joint 2 has stiffeners printed in funnel-shaped parts. Joint 3 has no stiffeners but prints with the same amount of materials as Joint 2. The funnel shape's area is 11425.0 mm^2 , and the stiffener's area is 3089.1 mm^2 . By moving the material from the stiffener to build up Joint 3, the effective thickness increased from 3.01 mm to 3.82 mm .

The stiffeners in Joint 2 and the increased printed thickness in Joint 3 were added to increase flexural stiffness and moment capacity with the same amount of materials. The comparisons will be provided in the conclusions.

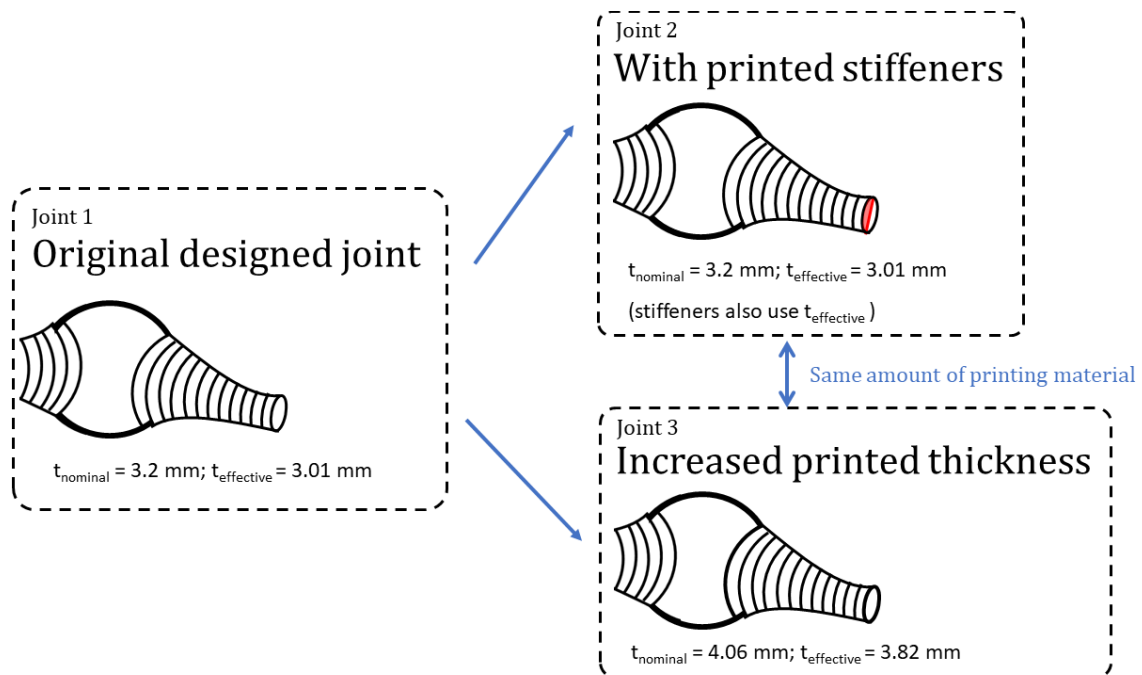


Figure 5.2: The joint analysis list.

The position and the production ideas of the stiffeners are shown in Fig.5.3. The stiffeners' production incorporates the funnel-shaped members' printing. Compared to the joint production without stiffeners, the joint with stiffeners have extra paths (in red) that create the stiffeners layer by layer.

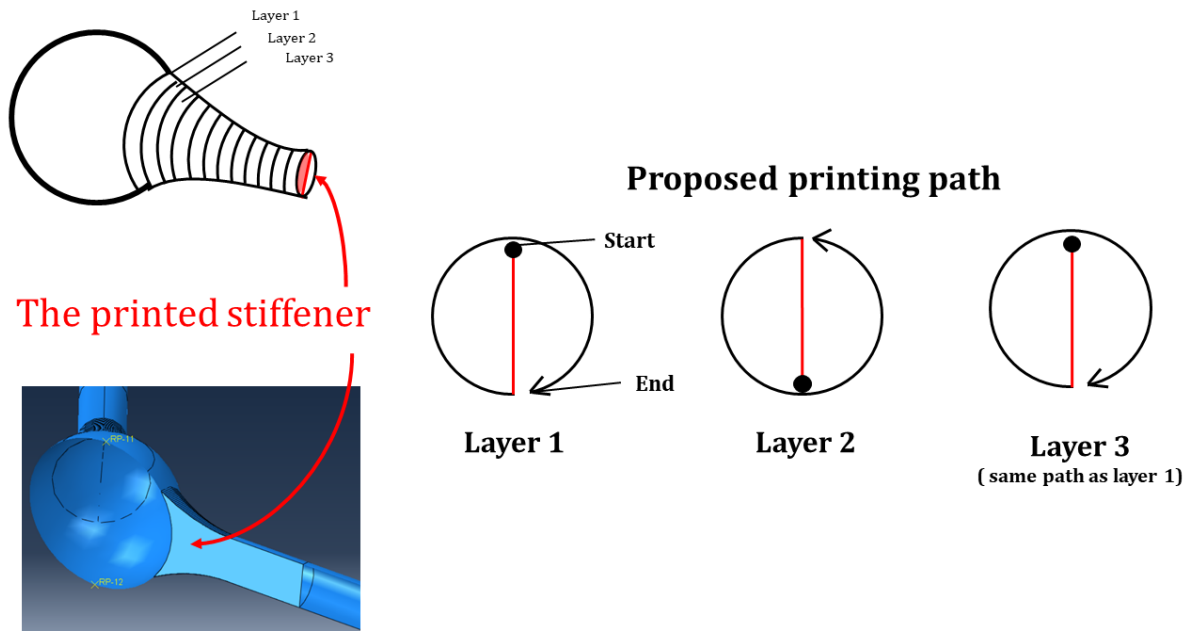


Figure 5.3: The position of the stiffener and the production ideas.

5.2.2 Settings

The overview of the Joint strength setting is shown in Fig.5.4.

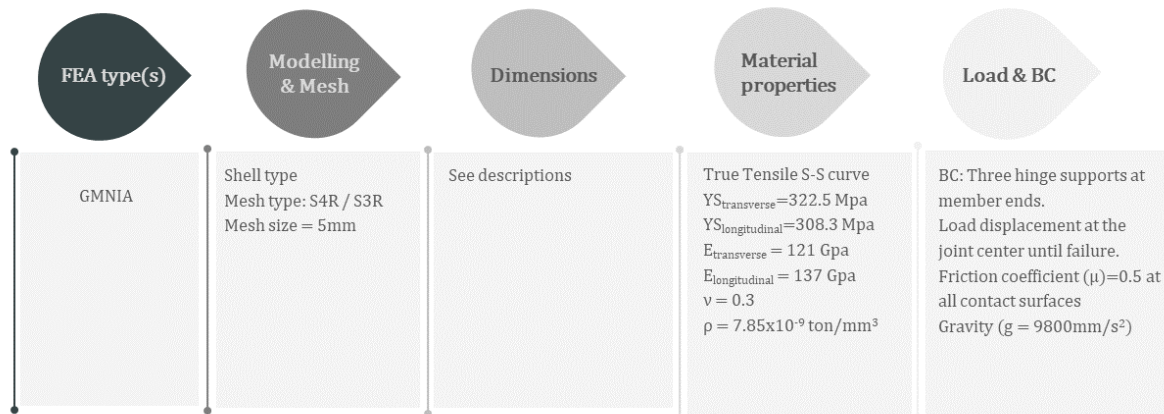


Figure 5.4: The joint test settings.

- FEA type(s):

The analysis type conducted here is the geometrically and materially non-linear analysis with imperfections (GMNIA). Imperfections taken into consideration are orthotropy and surface roughness. Lack of straightness is not considered because the instability of the structure is not sensitive to the buckling effect. The parameters used are from the bending test, which has ruled out the effect of lack of straightness from the average measured data from four different sides.

- Modelling & Mesh:

The model of the tube is a shell type structure. Three WAAM printed parts on the node are meshed with 5mm in length. Cold-form tubes, which are welded to the WAAM parts as the joint extension, are shell-type structure with 5mm mesh in length. As for bearings and supports, those

are built with solid type with 5mm mesh in length. Two mesh types are generated in the model, one is S4R (4-node general-purpose shell, reduced integration with hourglass control, finite membrane strains), and the other is S3R (3-node triangular general-purpose shell, finite membrane strains).

- Dimensions:

The WAAM printed specimens' dimensions in the lab test were taken as the reference for building up the model.

The model consists of five types of parts (Fig.5.5):

- The first is the casted hollow ball node at the center, with outer diameter of 100mm and 10mm of thickness.
- The second is the three funnel shape WAAM printed legs, which have a middle-to-middle surface diameter of 60mm at the near end of the node and a diameter of 30mm at the far end of the node. The nominal thickness is 3.2mm, and the effective thickness for incorporating surface roughness is 3.01mm.

The total length of the WAAM leg is 100mm, the 50mm at the far end is straight, the other 50mm at the near end has a curvature of $y = 15/(50)^2 \cdot x^2$ (x from 0 to 50mm) for the funnel shape.

- The third one is three cold-formed tube legs welded to the far end of the WAAM printed leg. The tube has a middle-to-middle surface diameter of 30mm, thickness of 5mm, and 600mm of length. Supports are located at 60mm before the tube's end.
- The fourth is three supports in half solid cylinder shape, 50mm in length and 26mm of diameter.
- The last is the WAAM printed stiffeners incorporate to the printing path of WAAM printed funnel leg parts.

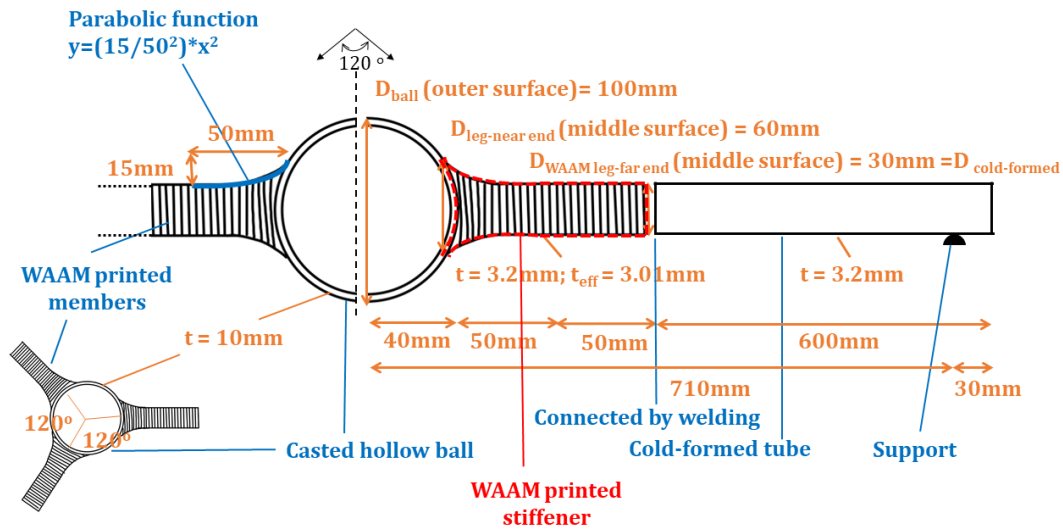


Figure 5.5: The joint's dimensions.

- Material properties:

The material of the casted hollow ball node and bearings are assumed to be bi-linear stress-strain curve material with the yield stress of 355 MPa, Young's modulus of 210 GPa, and Poisson's ratio (ν) of 0.3.

The funnel shape WAAM printed legs uses the stress-strain curve from the tensile stress-strain curve. The stress-strain curve of the longitudinal direction is also used for building up the orthotropic properties. The Yield stress (YS) in the transverse direction is 322.5 MPa and in the longitudinal direction is 308.3 MPa. Young's modulus (E) in the transverse direction is 121 GPa

and in the longitudinal direction is 137 GPa. Poisson's ratio (ν) is 0.3. The density (ρ) of the material is $\rho=7.85 \cdot 10^{-9} \text{ton/mm}^3$.

The material of the cold-formed tubes is assumed to be a bi-linear stress-strain curve with the yield stress of 460 MPa, Young's modulus of 210 GPa, and Poisson's ratio (ν) of 0.3. The high yield stress is chosen to prevent the plasticity that occurred during the test and cause excessive deformation.

- Load & BC:

The overview of the joint's boundary conditions and Load settings can be seen in Fig.5.6.

Three supports has the bottom fixed (shown in Fig.5.6 (a)), and for three tubes' ends (shown in Fig.5.6 (b)), two sides are confined to prevent rolling (in local coordinates, except for $U_x=0$, all others ($U_y, U_z, UR_x, UR_y, UR_z$) $\neq 0$).

As for the ball node, the load-displacement of 300mm is applied at the top to simulate the pressing of the bearings (shown in Fig.5.6 (c)).

The sliding friction coefficient of dry steels is around 0.42 to 0.62 [56]. Hence, the friction coefficient assumption of $\mu=0.5$ is used.

The Gravity, with the value $g = 9800 \text{mm/s}^2$, is included in the simulation.

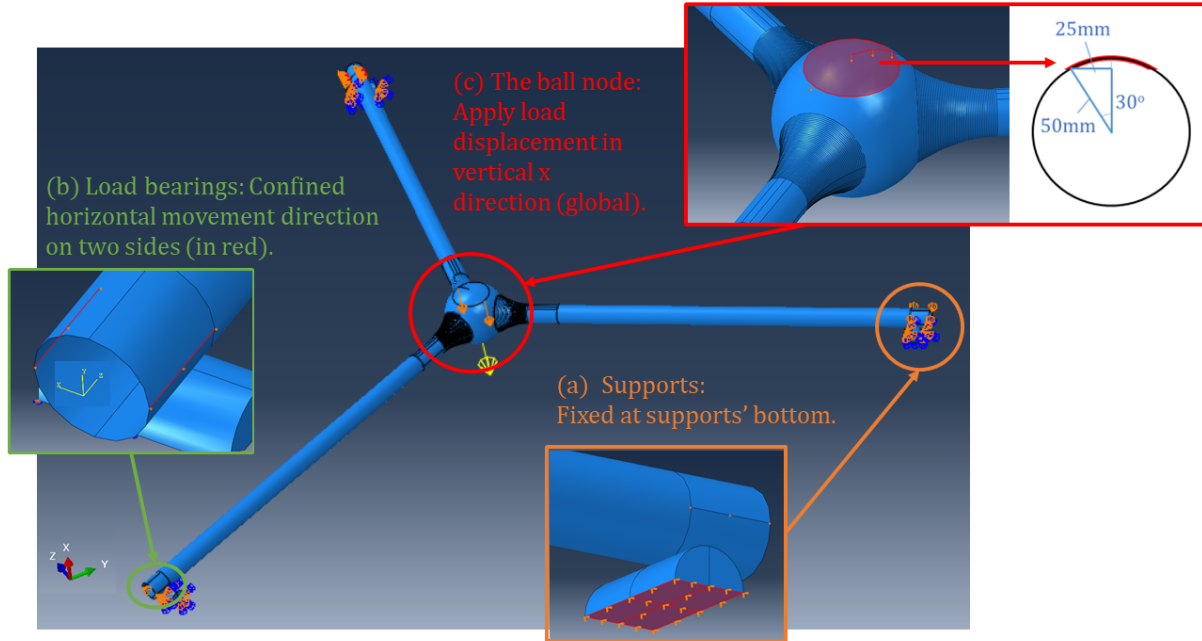


Figure 5.6: Loads and boundary conditions of the joint.

5.2.3 The setup for acquiring moment rotation curve

The setup of the moment-rotation curves are provided to show how the moment-rotation curve be acquired at the node center.

The load-displacement (d) from the experiment is applied onto the joint and cause a rotation φ (Fig.5.7). The moment (M) at the node is computed by the reaction force (F) times the lever arm between the node center to the support, which is 710mm.

Therefore, the functions for acquiring M and φ at the node center are:

$$M = L \cdot F = 710 \cdot F(Nmm) \quad (5.1)$$

$$\varphi = \tan^{-1}\left(\frac{d}{710}\right)(rad) \tag{5.2}$$

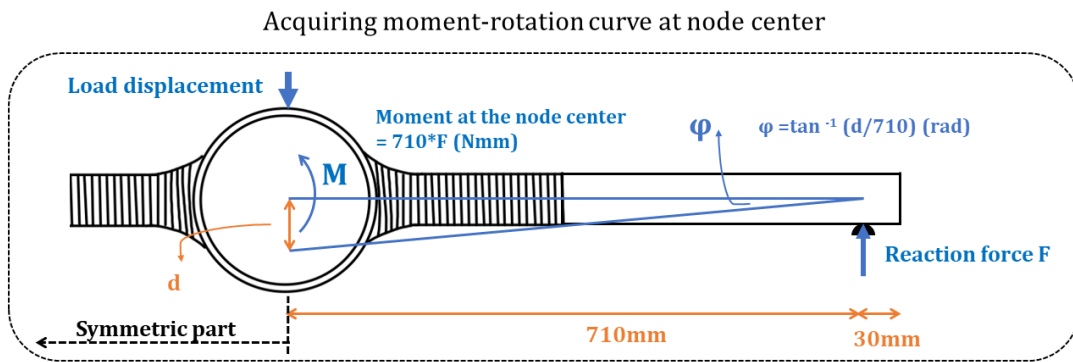


Figure 5.7: The setup for acquiring moment rotation curve at the node center.

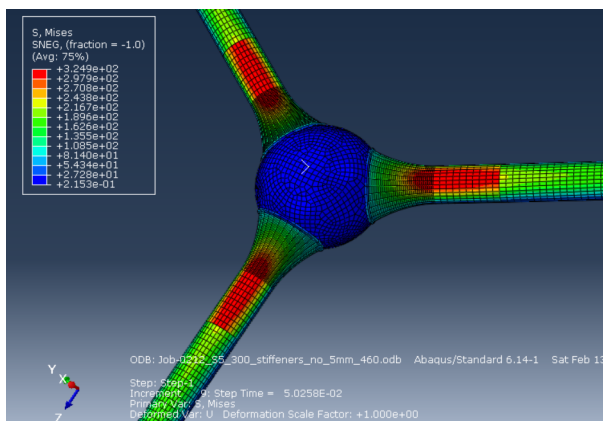
5.2.4 Result and strength prediction

The moment-rotation curves are presented to estimate the stiffness and moment capacity of the joint. Joints are built with orthotropic material and utilized the effective thickness. Three types of joints are presented.

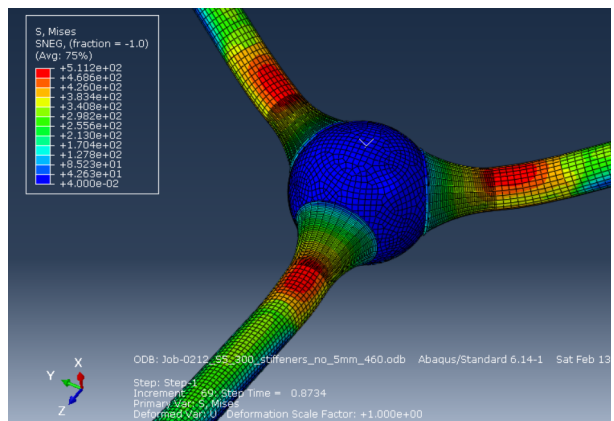
Joint simulations' result figures:

Joint 1:

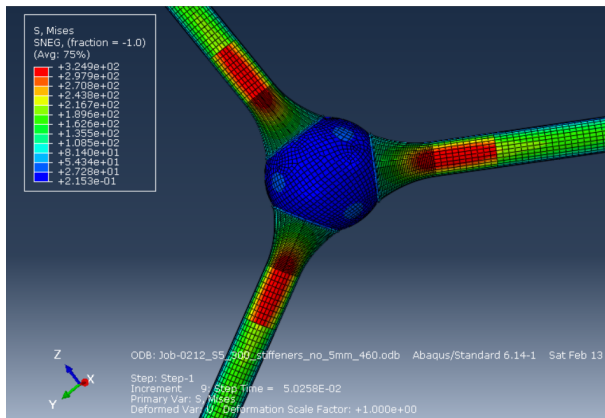
The result figures of the joint without stiffeners are shown in Fig.5.8. While yielding, the stress concentrates at the end of the WAAM printed part at both sides of the joint. When ultimate stress is reached, the stress concentrates on the WAAM funnel part, where the parabolic line connects to the straight line. The ultimate stress figures show the point before the structure fallen out of the support at phi=0.36 (see Fig.5.11).



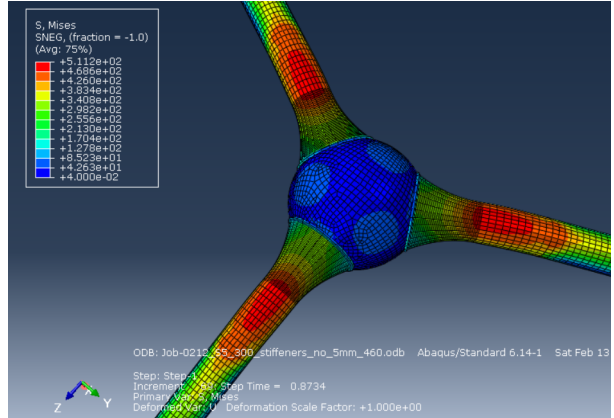
(a) Yield stress reached - Top view.



(b) Ultimate stress reached - Top view.



(c) Yield stress reached - Bottom view.

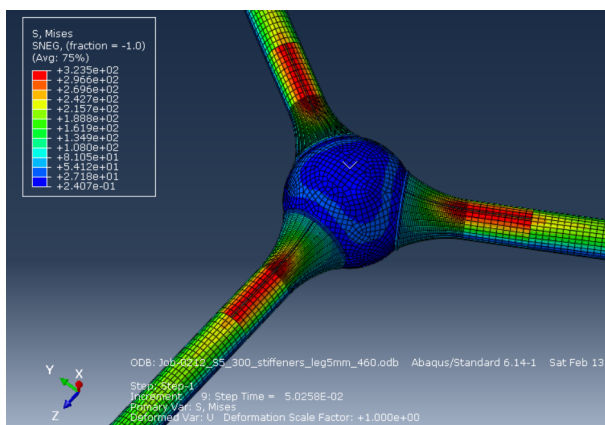


(d) Ultimate stress reached - Bottom view.

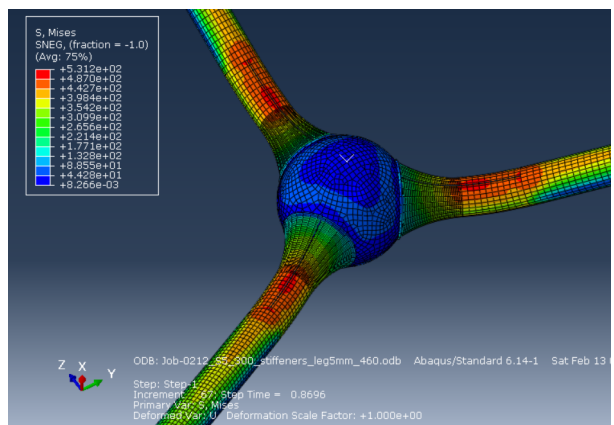
Figure 5.8: Result figures of the joint without printed stiffeners.

Joint 2:

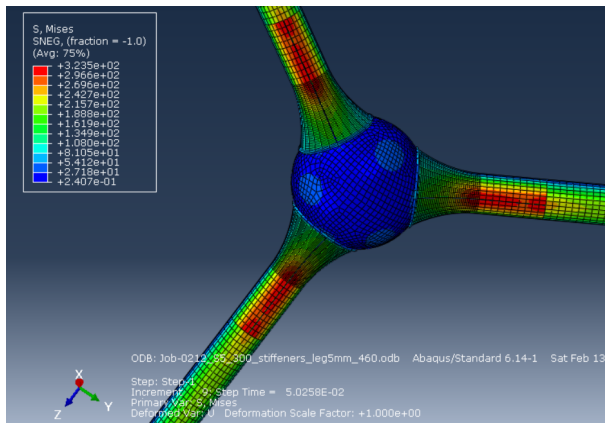
The result figures of the joint with stiffeners are shown in Fig.5.9. While yielding, the stress concentrates at the end of the WAAM printed part at both sides of the joint, as the joint without stiffeners. When ultimate stress is reached, the stress concentrates in the WAAM funnel part also occurred where the parabolic line connects to the straight line when compared to the joint without stiffness. The difference is that the stress concentration is lower because the stiffeners spread the stress more evenly to the adjacent area. The ultimate stress figures show the point before the structure fallen out of the support at $\phi=0.36$ (see Fig.5.11).



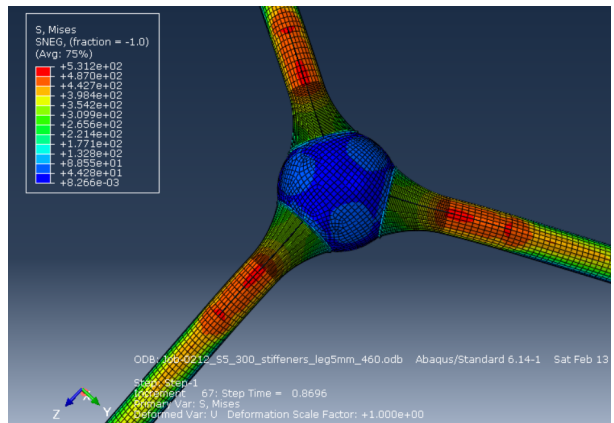
(a) Yield stress reached - Top view.



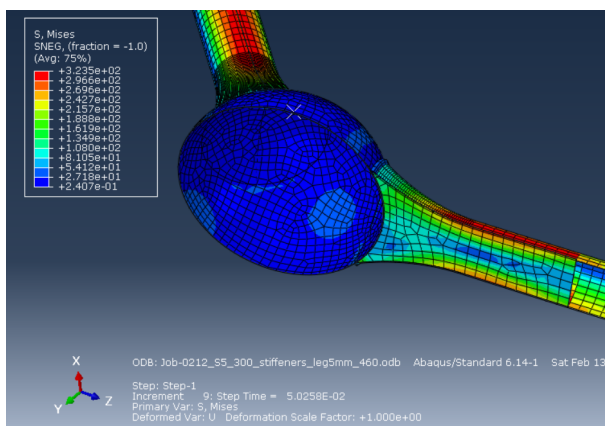
(b) Ultimate stress reached - Top view.



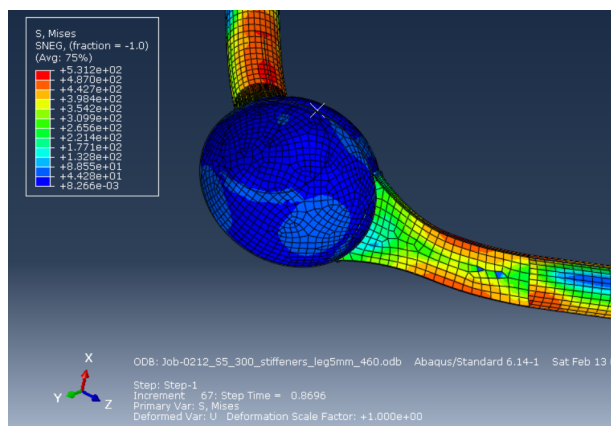
(c) Yield stress reached - Bottom view.



(d) Ultimate stress reached - Bottom view.



(e) Yield stress reached - Stiffener.

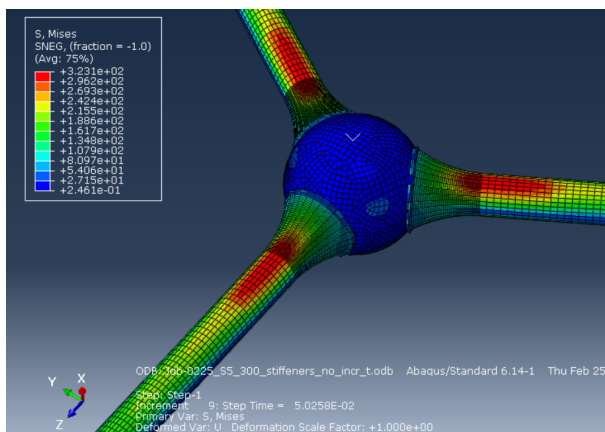


(f) Ultimate stress reached - Stiffener.

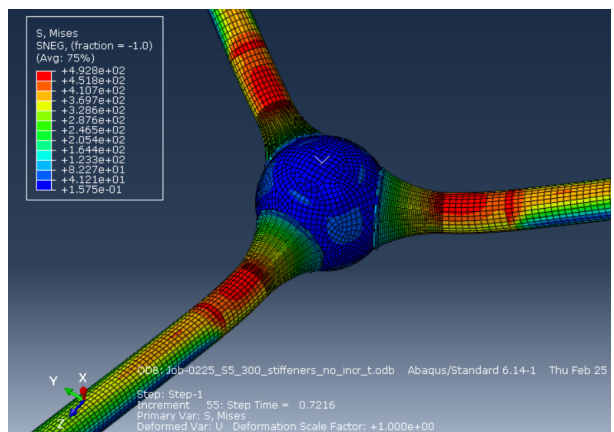
Figure 5.9: Result figures of the joint with printed stiffeners.

Joint 3:

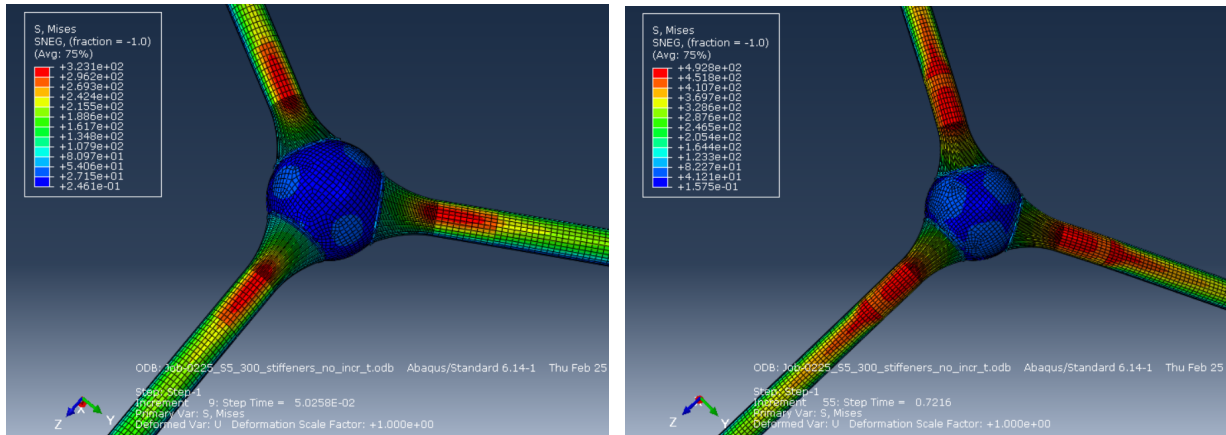
The result figures of the joint without stiffeners but with increased thickness are shown in Fig.5.10. The results figures are similar to the Joint 1. While yielding, the stress concentrates at the end of the WAAM printed part at both sides of the joint. When ultimate stress is reached, the stress concentrates on the WAAM funnel part, where the curved line connects to the straight line. The ultimate stress figures show the point which converged at $\phi=0.36$ (see Fig.5.11).



(a) Yield stress reached - Top view.



(b) Ultimate stress reached - Top view.



(c) Yield stress reached - Bottom view.

(d) Ultimate stress reached - Bottom view.

Figure 5.10: Result figures of the joint without printed stiffeners.

Moment - φ curve

Moment - φ curves are shown in Fig.5.11. Joint 1, which has no stiffeners, obtains the stiffness $k = 38163907 \text{ Nmm/rad}$ (38.16 KNm/rad), and moment capacity of 1445254.7 Nmm (1.45 KNm). Joint 2, which has printed stiffeners, acquires the stiffness $k = 42666059 \text{ Nmm/rad}$ (42.67 KNm/rad), and moment capacity of 1810507.1 Nmm (1.81 KNm). Joint 3, which has increased printed thickness but no stiffeners, obtains the stiffness $k = 43652472 \text{ Nmm/rad}$ (43.65 KNm/rad), and moment capacity of 1840419.4 Nmm (1.84 KNm).

With same amount of printed material, Joint 3 behaves better than Joint 2. When both compared to Joint 1, Joint 2 increased 11.8% of the flexural stiffness (from 38.16 KNm/rad to 42.67 KNm/rad) and increase 24.8% of the moment capacity (from 1.45 KNm to 1.81 KNm); Joint 3 increased 14.4% of the flexural stiffness (from 38.16 KNm/rad to 43.65 KNm/rad) and increase 26.9% of the moment capacity (from 1.45 KNm to 1.84 KNm).

The endpoint for calculating the moment rotational curve was decided because Joint 3 (in yellow) converged numerically the earliest among three joints at the φ of 0.29, and unify the moment capacity at the same φ is more convenient for comparisons. The calculation of Joint 1 and Joint 2 terminates because the end of the cold-formed tubes has fallen off the supports (see Fig.5.12) at φ equals to 0.35, which is a considerably large deformation.

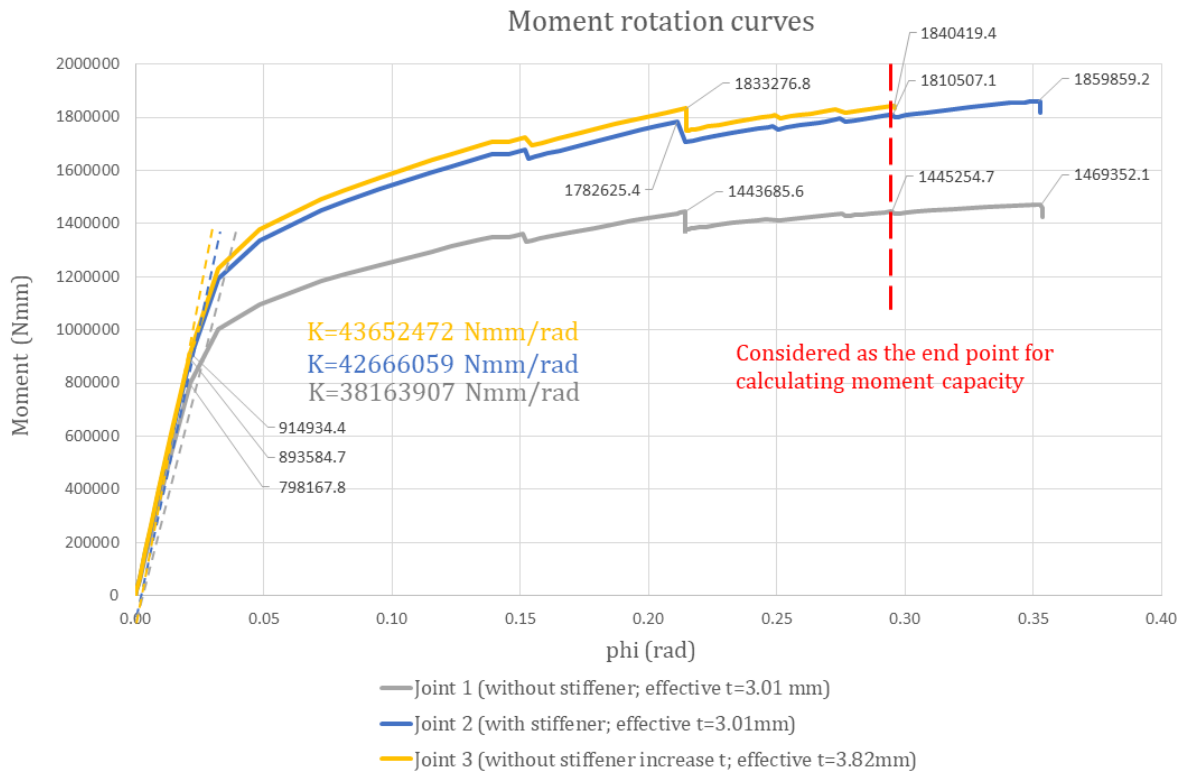


Figure 5.11: Moment-rotation curves.

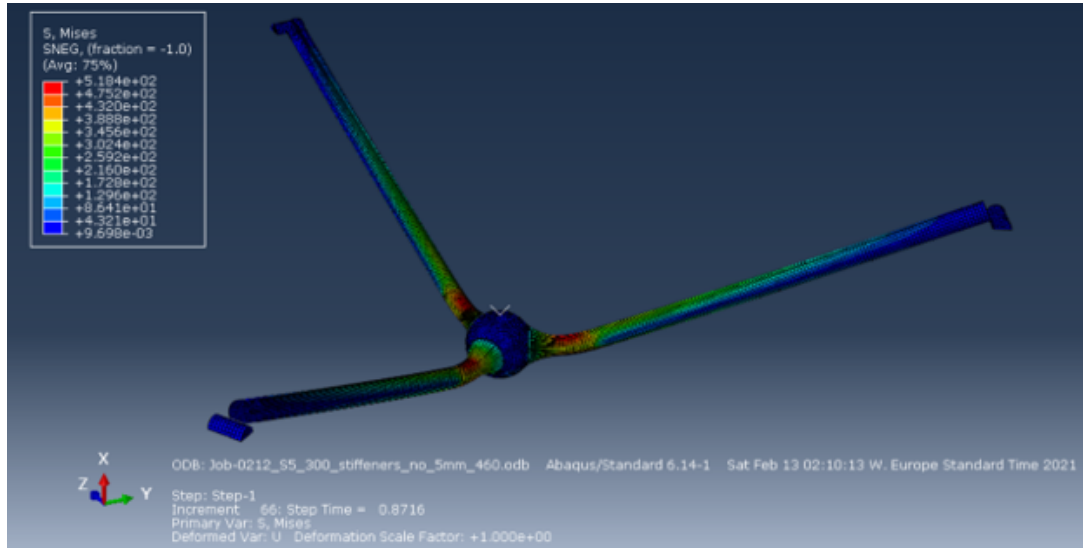
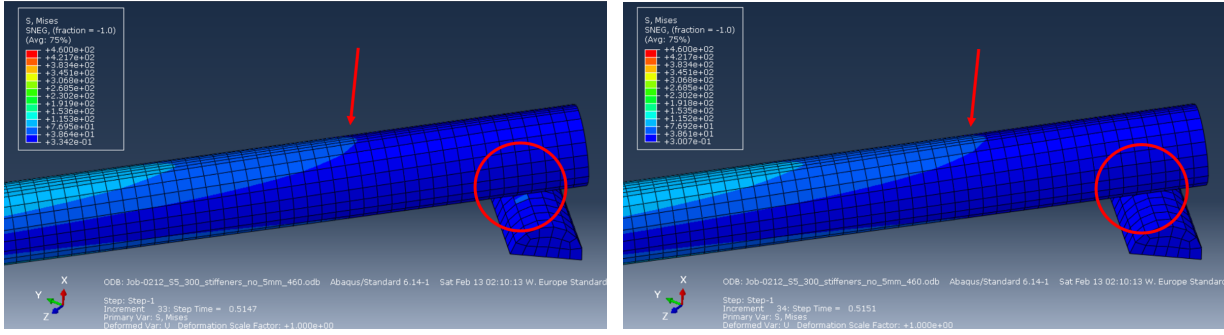


Figure 5.12: The termination of the FEA for joint 1 due to the structure disattachment from the supports at $\phi=0.36$.

Several sharp moment drops have been observed in the Fig.5.11. The reason is owing to the slip between the end of a cold-formed tube and the support (see Fig.5.13.) In Fig.5.13 (a), the sliding force is still lower than the friction. High force concentration at the contact surface due to friction can be seen in the red circle. Then, the tube slid in the next moment (shown in Fig.5.13 (b)), which caused the force redistribution. Larger stress occurred and spread slightly towards the tube end (see the red error). Also, the friction at the contact area (shown in the red circle) has dropped from 38.6 MPa (blue) to 0.33 MPa (in dark blue) and starts to accumulate for the next slide.



(a) The force distribution before the slip.

(b) The force distribution after the slip.

Figure 5.13: The slip of the tube on a support and caused force redistribution.

Joint strength classification

Joints are classified as rigid, semi-rigid, and pinned with the determination coefficient α and β (can be seen in Section.2.3.2). The result shows joint 1 (the original design without stiffeners) has $\alpha= 2.37$ and $\beta= 1.52$, joint 2 (the one with stiffeners) has $\alpha= 2.65$ and $\beta= 1.90$, joint 3 (the one which has increased thickness) has $\alpha= 2.71$ and $\beta= 1.94$. Three joints falls into the categories of semi-rigid joint.

Table 5.1: Joint classification.

Joint strength analysis setting list	Stiffness k (Nmm/rad)	EI (cold-form tube)	Lo	Alpha $\alpha = \frac{k}{EI/L_0}$	Mju (joint)	Meu (cold-form tube)	Beta $\beta = \frac{M_{j,u}}{M_{e,u}}$
Without stiffeners	38163907	210000	710	2.37	1445254.7	950904.2	1.52
With stiffeners	42666059	210000	710	2.65	1810507.1	950904.2	1.90
Without stiffeners (increase t)	43652472	210000	710	2.71	1840419.4	950904.2	1.94

5.3 Conclusions

This chapter first designed WAAM printed joints with an experimental-based setup. Second, the material data and imperfection parameters are from the components' lab test simulations in Ch4. Last, three types of joints with their joint stiffness and the moment capacity are provided.

Research questions in this chapter are:

- 1) How do simulations of four lab experiments help with the strength prediction of the joint?
- 2) How does the designed joint performs in regards to the stiffness and the moment capacity?
- 3) How can the joint be improved?

This section provides the answers to the research questions of this chapter:

1. The joints are built with parameters (material non-linearity, anisotropy, surface roughness) from the WAAM components that are examined before being used in the strength analysis. All are covered in the simulation of four lab tests. Material non-linearity data have been tested in the tensile test simulation and the compression test simulation. The effective thickness has been derived from the bending test and discussed in the bending simulation.

2. With the same amount of printed material, Joint 3 behaves better than Joint 2. When both compared to Joint 1, Joint 2, which has printed stiffeners, increased 11.8% of the flexural stiffness and increase

24.8% of the moment capacity; Joint 3, which has thicker printed thickness, increased 14.4% of the flexural stiffness and increase 26.9% of the moment capacity.

Joints are classified as rigid, semi-rigid, and pinned with the determination coefficient α and β . The result shows joint 1 (the original design without stiffeners) has $\alpha= 2.37$ and $\beta= 1.52$, joint 2 (the one with stiffeners) has $\alpha= 2.65$ and $\beta= 1.90$, joint 3 (the one which has increased thickness) has $\alpha= 2.71$ and $\beta= 1.94$. Three joints falls into the categories of semi-rigid joint.

3. Except for printing the stiffeners in the same process as the WAAM funnel part, more improvements can be made to make the joint rigid:

- Increase WAAM printed legs' thickness even more. (p.s: Single bead layers can print the wall thickness from 2.5 mm to around 10mm [37].)
- Increase the dimensions of the WAAM printed legs i.e. larger diameter.

4. Influence of the friction coefficient:

The friction coefficient is assumed to be $\mu=0.5$. If the real friction coefficient is lower, the simulated stiffness would be lower. Otherwise, if the real friction coefficient is higher, the simulated stiffness would be higher.

5. Benefits of the printed funnel-shaped members:

- The stress concentration has shifted to the ball node, which reduces the chance of rupture at the connection between the ball node and members.
- Control of the failure point with varying printing parameters. When buildings are subjected to unexpected high load at the node but still fixable, building parts can be easily replaced with newly printed joints.
- The smoother printing geometry can probably avoid and reduce the fatigue of the joint.

Chapter 6

Conclusions and recommendations

6.1 Answer to the research question

Anticipating the potential of using mechanical data from WAAM's lab tests, which are examined in the numerical simulations, to predict the strength of a designed WAAM joint, this study is focused on the following main research questions:

How can the strength analysis of designed WAAM joints be carried out using WAAM components' lab test data to provide a reliable strength prediction?

Based on the results of this work, the main research question can now be answered. It seems that there is potential to provide reliable strength prediction of the designed WAAM joints with the use of EN 1993-1-6: Eurocode 3 to simulate WAAM lab components with shell elements for two reasons. First, the simulation results yield not only reasonable limited error but show closer values to the lab test results with the shell analysis process in EC3. Second, the parameters (material non-linearity, anisotropy, surface roughness) from the WAAM components are examined before being used in the strength analysis of designed WAAM joints, therefore, make them more reliable to use.

Although the lack of several parameters undermines the precision of the simulations, it can be improved with more tests performed and data provided.

The elaborations of parameters examinations in numerical simulations, the use of the examined parameters in the strength analysis, and the lack of lab test data are provided in the following conclusions and recommendations.

6.2 Conclusions

Conclusions are arranged in two parts. One is the conclusion of the reliability from the components' lab test simulations. The other is the strength prediction of designed joints that can be further used for designing and compare with the lab experiment of joints.

6.2.1 Reliability of the simulation - Interpretations of lab test simulation results

Mechanical data have been extracted from the lab test results, and the imperfections of WAAM components have been defined and included in the simulation step by step for validation. The material non-linearity has been tested in the tensile and the compression test simulation. The use of effective thickness for surface roughness has been evaluated in the bending test. The lack of straightness has been discussed in the buckling test. The orthotropic material behavior is built in the elastic range with the young's modulus from two printed directions.

Tensile test simulation

- The material non-linear data (yield strength, ultimate strength, and young's modulus) of both transverse and longitudinal printed directions in the tensile test simulation are valid since it has less than 0.5% of error compared to the lab test (engineering stress-strain curve).
- The orthotropic behavior in the tensile test has barely any difference in the simulation. The errors of yield stresses, ultimate stresses, and young's modulus, in both transverse and longitudinal printed directions, are all within 0.03%.

Compression test simulation

- The compression test simulations successfully use the material non-linearity data for simulating the milled WAAM sample because the results are correct and close to the tensile test before the yield point. The yield stress in the simulation has only 1.8% of error, and young's modulus has only 0.41% of errors.
- The inclusion of the possible geometrical imperfections shape found from LBA to the numerical model reduces the percentage errors of failure load from +52.27% to +13.75%.
- The WAAM components' imperfections considered in the compression test are the orthotropic behavior. The results indicate a minimal influence of orthotropic to the model, young's modulus is the same, and the value of yield stress shows a maximum drop of 0.78% (from Setting 2 to Setting 3).

Bending test simulation

- Numerical simulations of the bending test examined the use of effective thickness (3.01mm) assume for surface roughness and shows a limited error (16.8%) in combination with all the simplified and assumed parameters, including:
 - An assumed Friction coefficient. The friction coefficient used in the simulation is $\mu=0.5$. A lower friction coefficient, for example, $\mu=0.2$, can make the deflection at the tube center increases 7.3% (from 2.154mm to 2.311mm) and decrease the error between the simulation and the lab test reduces from 17% to 10.7%.
 - Assumed material properties and dimensions of the bending test supports and bearings.
- With the inclusion of the effective thickness, the simulated center tube deflections decreased from 2.154mm (Setting 5) to 2.022mm (Setting 3), which reduce the error from -22% to -16.8% when compared to the lab test result (2.589mm).
- The modeled orthotropic behavior again has a negligible effect. The deflection reduced around 0.1% both include or exclude the involvement of surface roughness.

Buckling test simulation

- When compared to the buckling load of the lab test, the implementation of effective thickness for surface roughness to the numerical model reduces around 10% to 15% of the error, and the inclusion of both effective thickness and lack of straightness reduce roughly 40% of the error to 35%.
- Numerical simulations of the buckling test studied the influence of lack of straightness and found the measured average lack of straightness ($e = L/791$) is too low to obtain the measured buckling load of the lab test (52.7KN). The simulated buckling load is 71.1KN and has a 35% error compared to the average buckling load of the lab test. The reasons for the higher buckling load that appears in the simulation could come from:
 - The measured lack of straightness is too less. The hand measuring of the lack of straightness in the lab experiment might contain a few mm of errors.
 - The real effective thickness could be thicker than the derived value from the lab test.

- The simplification of the geometrical imperfections included in the model. Local geometrical imperfections are not included and the analysis of using 3D scanning as the tube’s FEA model might help to get a more precise result.
- The buckling simulation result shows that the buckling load is very sensitive to the lack of straightness. Few fractions of percentage increase (0.2% to 0.4%) of lack of straightness lead to tens of percentage error drop (19.6%) of buckling load while compared to the lab results.
- For the material’s orthotropic behavior, it has a minor influence on the strength of buckling stress. In the buckling simulation, the maximum difference is that the buckling stress decreases 1.36% from 326.3MPa to 321.9MPa.

6.2.2 Strength prediction of joints

Examined parameters used for building the strength prediction models are the material non-linearity data and the effective thickness.

Three joints have been designed and analyzed:

- Joint 1, which has no stiffeners, obtains the stiffness $k = 38.16 \text{ KNm/rad}$ and moment capacity of 1.45 KNm .
- Joint 2, which has printed stiffeners, acquires the stiffness $k = 42.67 \text{ KNm/rad}$ and moment capacity of 1.81 KNm .
- Joint 3, which has no stiffeners but increased printed thickness that uses the same amount of printing material as Joint 2, obtains the stiffness $k = 43.65 \text{ KNm/rad}$ and moment capacity of 1.84 KNm .
- With the same amount of printed material, Joint 3 behaves better than Joint 2. Joint 3 is 2.3% larger in flexural stiffness and 1.66% larger in the moment capacity.
- Three joints fall into the categories of the semi-rigid joint by the joint classification. Besides adding stiffeners in the joint, other improvements can further increase the joint rigidity, such as:
 - Increase WAAM printed legs’ thickness even more. (p.s: Single bead layers can print the wall thickness from 2.5 mm to around 10 mm [37].)
 - Increase the dimensions of the WAAM printed legs, i.e., larger diameter.

6.3 Recommendations

For the researchers

1. Unknown parameters are assumed in the analysis for building up materials’ orthotropic behavior. The measuring of the Poisson’s ratio (ν) can help to define the Shear modulus (G).
2. It is recommended to use a strain gauge on the specimen in the compression lab test measurements to attain higher precision.
3. The friction coefficient should be measured in the lab test and provided as the numerical simulation inputs to obtain a more precise results.
4. Buckling loads are very sensitive to geometrical imperfections, global imperfections (lack of straightness and surface roughness) are considered. However, for study local geometrical imperfections, it would be recommended to use 3D scanned models as the geometry to perform more detailed analysis.

For the designers:

5. From the simulation of tensile test, compression test, bending test, and buckling test, the orthotropic material behavior, which is built in the elastic range with the young’s modulus from two printed directions, shows minor influence on strength. Therefore, under this setting, isotropic material setting could be used for acquiring first-hand strength data for the preliminary design of the strength for hollow circular components in the elastic range.

6.4 Future outline and research

1. Further lab testing of the designed joint.

The joint's strength prediction setup based on the lab test scenario that could be easily used for future lab testing.

If the designed joint's lab test shows close results to the prediction, it can prove that the strength's simulation successfully uses mechanical properties provided by WAAM components' lab tests, and the imperfections defined.

2. Investigation of more complex geometries with different combinations of materials.

The geometry of the WAAM printed objects are still limited to a simple geometry with monotonic material. More complex structures with different combinations of materials could be investigated, e.g., complex-shaped WAAM hollow tubes with cement infill.

3. Consideration of using bolted connections for better circulation design principles.

Using bolted connection to connect joints to members can help to achieve the material bank goal. Building parts can be removed and reuse in new buildings easier with printed joints.

4. Reducing structure weight and material usage by incorporating the parametric design.

The parametric design could be applied to reduce the excessive material usage and reduce the structure's weight. For instance, according to different forces on each of the joint's printed legs, the design of different dimensions and stiffeners can be applied to the joint production process.

Bibliography

- [1] G. S. Van Bolderen, “Exploration of stability of 3D-printed steel members: A study to buckling behaviour of wire and arc additively manufactured stainless steel tubular columns,” Ph.D. dissertation, Delft University of Technology, 2017.
- [2] U. Nations, “The sustainable development goals report 2019,” *New York*, 2019.
- [3] I. UNEP, “2019 global status report for building and construction: Towards a zero-emission, efficient and resilient buildings and construction sector,” 2019.
- [4] O. P. Gibbons, “How to calculate embodied carbon,” Sep 2020. [Online]. Available: <https://www.istructe.org/resources/guidance/how-to-calculate-embodied-carbon/>
- [5] A. Agkathidis and A. Brown, “Tree-structure canopy: a case study in design and fabrication of complex steel structures using digital tools,” *International Journal of Architectural Computing*, vol. 11, no. 1, pp. 87–104, 2013.
- [6] S. Johari and K. N. Jha, “Challenges of attracting construction workers to skill development and training programmes,” *Engineering, Construction and Architectural Management*, 2019.
- [7] E. M. Network, “Determining labour shortages and the need for labour migration from third countries in the eu: synthesis report for the emn focussed study 2015,” 2015.
- [8] S. Kim, S. Chang, and D. Castro-Lacouture, “Dynamic modeling for analyzing impacts of skilled labor shortage on construction project management,” *Journal of Management in Engineering*, vol. 36, no. 1, p. 04019035, 2020.
- [9] R. Kühne, M. Feldmann, S. Citarelli, U. Reisgen, R. Sharma, and L. Oster, “3D printing in steel construction with the automated Wire Arc Additive Manufacturing,” *Ce/Papers*, vol. 3, no. 3-4, pp. 577–583, 2019.
- [10] R. Kühne, M. Feldmann, S. Citarelli, U. Reisgen, R. Sharma, and L. Oster, “3d printing in steel construction with the automated wire arc additive manufacturing,” *ce/papers*, vol. 3, no. 3-4, pp. 577–583, 2019.
- [11] J. L. Z. Li, M. R. Alkahari, N. A. B. Rosli, R. Hasan, M. N. Sudin, and F. R. Ramli, “Review of wire arc additive manufacturing for 3d metal printing,” *International Journal of Automation Technology*, vol. 13, no. 3, pp. 346–353, 2019.
- [12] N. Raju, G. Balaganesan, and G. S. Kumar, “Energy consumption of welding-based additively manufactured materials,” in *Advances in Additive Manufacturing and Joining*. Springer, 2020, pp. 137–148.
- [13] E. Durmisevic, “Buildings as material banks,” *ISSN 2232-965X*, p. 140, 2015.
- [14] L. Bragança, “Sbe19 brussels-bamb-circpath: Building as material banks: a pathway for a circular future,” 2019.
- [15] J. Müller, M. Grabowski, C. Müller, J. Hensel, J. Unglaub, K. Thiele, H. Kloft, and K. Dilger, “Design and parameter identification of wire and arc additively manufactured (waam) steel bars for use in construction,” *Metals*, vol. 9, no. 7, p. 725, 2019.
- [16] F. Montevicchi, G. Venturini, A. Scippa, and G. Campatelli, “Finite element modelling of wire-arc-additive-manufacturing process,” *Procedia Cirp*, vol. 55, pp. 109–114, 2016.

- [17] J. Ding, P. Colegrove, J. Mehnen, S. Williams, F. Wang, and P. S. Almeida, "A computationally efficient finite element model of wire and arc additive manufacture," *The International Journal of Advanced Manufacturing Technology*, vol. 70, no. 1-4, pp. 227–236, 2014.
- [18] D. Camilleri, T. Comlekci, and T. F. Gray, "Computational prediction of out-of-plane welding distortion and experimental investigation," *The Journal of Strain Analysis for Engineering Design*, vol. 40, no. 2, pp. 161–176, 2005.
- [19] J. Goldak, A. Chakravarti, and M. Bibby, "A new finite element model for welding heat sources," *Metallurgical transactions B*, vol. 15, no. 2, pp. 299–305, 1984.
- [20] S. N. Ahmad, Y. H. Manurung, M. F. Mat, Z. Minggu, A. Jaffar, S. Pruller, and M. Leitner, "Fem simulation procedure for distortion and residual stress analysis of wire arc additive manufacturing," in *IOP Conference Series: Materials Science and Engineering*, vol. 834, no. 1. IOP Publishing, 2020, p. 012083.
- [21] L. Gardner, P. Kyvelou, G. Herbert, and C. Buchanan, "Testing and initial verification of the world's first metal 3d printed bridge," *Journal of Constructional Steel Research*, vol. 172, p. 106233, 2020.
- [22] A. Paolini, S. Kollmannsberger, and E. Rank, "Additive manufacturing in construction: A review on processes, applications, and digital planning methods," *Additive Manufacturing*, vol. 30, p. 100894, 2019.
- [23] *Eurocode 3: design of steel structures : part 1-6 : strength and stability of shell structures*. London: BSI, 2010, incorporating corrigendum April 2009. [Online]. Available: <https://cds.cern.ch/record/2154845>
- [24] B. Ralph, "Method of making decorative articles," Apr. 14 1925, uS Patent 1,533,300.
- [25] C. A. de Saracibar, A. Lundbäck, M. Chiumenti, M. Cervera, C. A. de Saracibar, A. Lundbäck, and M. Chiumenti, "Shaped metal deposition processes," *Encyclopedia of thermal stresses*, pp. 4346–4355, 2014.
- [26] A. H. Snijder, L. P. L. van der Linden, C. Goulas, C. Louter, and R. Nijse, "The glass swing: a vector active structure made of glass struts and 3D-printed steel nodes," *Glass Structures and Engineering*, vol. 5, no. 1, pp. 99–116, 2020. [Online]. Available: <https://doi.org/10.1007/s40940-019-00110-9>
- [27] D. Marini, D. Cunningham, and J. R. Corney, "Near net shape manufacturing of metal: a review of approaches and their evolutions," *Proceedings of the institution of mechanical engineers, Part B: journal of engineering manufacture*, vol. 232, no. 4, pp. 650–669, 2018.
- [28] D. Ding, Z. Pan, D. Cuiuri, and H. Li, "Wire-feed additive manufacturing of metal components : technologies , developments and future interests," no. May, 2015.
- [29] A. C. F. on Additive Manufacturing Technologies and A. C. F. on Additive Manufacturing Technologies. Subcommittee F42. 91 on Terminology, *Standard terminology for additive manufacturing technologies*. Astm International, 2012.
- [30] I. Gibson, D. Rosen, and B. Stucker, "Powder bed fusion processes," in *Additive Manufacturing Technologies*. Springer, 2015, pp. 107–145.
- [31] —, "Directed energy deposition processes," in *Additive manufacturing technologies*. Springer, 2015, pp. 245–268.
- [32] M. Molitch-Hou, "Overview of additive manufacturing process," in *Additive Manufacturing*. Elsevier, 2018, pp. 1–38.
- [33] O. Eyercioglu, Y. Atalay, and M. Aladag, "Evaluation of overhang angle in tig welding-based wire arc additive manufacturing process," *International Journal of Research-GRANTHAALAYAH*, vol. 7, no. 10, pp. 247–254, 2019.
- [34] L. Yuan, Z. Pan, D. Ding, Z. Yu, S. V. Duin, H. Li, W. Li, and J. Norrish, "Fabrication of metallic parts with overhanging structures using the robotic wire arc additive manufacturing," *Journal of Manufacturing Processes*, no. March, pp. 0–1, 2020. [Online]. Available: <https://doi.org/10.1016/j.jmapro.2020.03.018>

- [35] V. Laghi, M. Palermo, G. Gasparini, and T. Trombetti, “Computational design and manufacturing of a half-scaled 3d-printed stainless steel diagrid column,” *Additive Manufacturing*, vol. 36, p. 101505, 2020.
- [36] B. Wu, Z. Pan, D. Ding, D. Cuiuri, H. Li, J. Xu, and J. Norrish, “A review of the wire arc additive manufacturing of metals: properties, defects and quality improvement,” *Journal of Manufacturing Processes*, vol. 35, no. August, pp. 127–139, 2018. [Online]. Available: <https://doi.org/10.1016/j.jmapro.2018.08.001>
- [37] A. Paskual, P. Álvarez, A. Suárez *et al.*, “Study on arc welding processes for high deposition rate additive manufacturing,” *Procedia Cirp*, vol. 68, pp. 358–362, 2018.
- [38] A. C. Bekker, J. C. Verlinden, G. Galimberti *et al.*, “Challenges in assessing the sustainability of wire+ arc additive manufacturing for large structures,” in *Proceedings of the Solid Freeform Fabrication Symposium—An Additive Manufacturing Conference, Austin, TX, USA, 2016*, pp. 8–10.
- [39] V. Dhinakaran, J. Ajith, A. F. Yasin, T. Jagadeesha, T. Sathish, and B. Stalin, “Wire Arc Additive Manufacturing (WAAM) process of nickel based superalloys – A review,” *Materials Today: Proceedings*, vol. 21, pp. 920–925, 2020. [Online]. Available: <https://doi.org/10.1016/j.matpr.2019.08.159>
- [40] J. Galan Argumedo, “Fatigue behavior and mechanical characterization of austenitic stainless-steel components produced through wire+ arc additive manufacturing,” 2020.
- [41] V. Kain, “Stress corrosion cracking (scc) in stainless steels,” in *Stress Corrosion Cracking*. Elsevier, 2011, pp. 199–244.
- [42] V. Laghi, M. Palermo, L. Tonelli, G. Gasparini, L. Ceschini, and T. Trombetti, “Tensile properties and microstructural features of 304L austenitic stainless steel produced by wire-and-arc additive manufacturing,” *International Journal of Advanced Manufacturing Technology*, vol. 106, no. 9-10, pp. 3693–3705, 2020.
- [43] S. Ren and S. Galjaard, “Topology Optimisation for Steel Structural Design with Additive Manufacturing,” in *Modelling Behaviour*. Springer International Publishing, 2015, pp. 35–44.
- [44] L. Skotny, “Analysis types and their abbreviations,” Dec 2016. [Online]. Available: <https://enterfea.com/analysis-types-and-their-abbreviations/>
- [45] A. Mediaworks, “Złote tarasy, warsaw, poland,” Nov 2017. [Online]. Available: <https://www.oasys-software.com/case-studies/zlote-tarasy-warsaw-poland/>
- [46] S. Stephan, J. Sánchez-Alvarez, and K. Knebel, “Reticulated structures on free-form surfaces,” *Stahlbau*, vol. 73, no. 8, pp. 562–572, 2004.
- [47] F. Fan, H. Ma, Z. Cao, and S. Shen, “A new classification system for the joints used in lattice shells,” *Thin-walled structures*, vol. 49, no. 12, pp. 1544–1553, 2011.
- [48] L. Van der Linden, “Innovative joints for gridshells,” 2015.
- [49] Y. J. Kim, Y. H. Lee, and H. Kim, “Bending Test of Welded Joints for Single-Layer Latticed Domes,” *Steel Structures*, vol. 8, pp. 357–367, 2008.
- [50] K. J. Rasmussen, “Full-range stress–strain curves for stainless steel alloys,” *Journal of constructional steel research*, vol. 59, no. 1, pp. 47–61, 2003.
- [51] I. Faridmehr, M. H. Osman, A. B. Adnan, A. F. Nejad, and R. Hodjati, “Correlation between Engineering Stress-Strain and True Stress-Strain Curve,” vol. 2, no. 1, pp. 53–59, 2014.
- [52] D. Roylance, “Stress-strain curves,” *Massachusetts Institute of Technology study, Cambridge*, 2001.
- [53] V. Laghi, M. Palermo, G. Gasparini, V. A. Girelli, and T. Trombetti, “Experimental results for structural design of Wire-and-Arc Additive Manufactured stainless steel members,” *Journal of Constructional Steel Research*, no. xxx, p. 105858, 2019. [Online]. Available: <https://doi.org/10.1016/j.jcsr.2019.105858>
- [54] L. Börgesson, “Abaqus,” in *Developments in geotechnical engineering*. Elsevier, 1996, vol. 79, pp. 565–570.

-
- [55] Abaqus, “Abaqus user’s manual. version 6.14,” 2014.
- [56] “Friction factors.” [Online]. Available: https://roymech.org/Useful_Tables/Tribology/co_of_fric.html
- [57] X. Dong, H. Zhao, L. Zhang, H. Cheng, and J. Gao, “Geometry effects in four-point bending test for thin sheet studied by finite element simulation,” *materials transactions*, vol. 57, no. 3, pp. 335–343, 2016.

Appendix A

Appendices

A.1 Material properties of INERTFIL 308LSi.

INERTFIL 308LSi



MIG-MAG Wires Stainless and Heat resistant steels

Inertfil 308LSi is a stainless steel solid wire similar to ER 308LSi suitable for welding austenitic stainless steels such as AISI 304 and AISI 304L. Excellent corrosion resistance and good mechanical properties. Si ~ 0,85% content improves weldability and bead appearance.

Classification	
AWS	A5.9: ER 308L Si
EN	12072: G 19 9 L Si

Approvals	Grades
TÜV	

see Appendix, Classification Society Approvals, for details pag. 521

Analysis of all-weld metal (Typical values in %)

C	Mn	Si	P	S	Cr	Ni	Mo	Nb	Cu	N	Ferrite
0.02	1.80	0.85	≤ 0.025	≤ 0.020	20	10	0.20	-	-	-	5-10

All-weld metal Mechanical Properties

Heat Treatment	Yield Strength N/mm ²	Tensile Strength N/mm ²	Elongation A5 (%)	Impact Energy ISO - V (J) 20°C	Hardness
As Welded	≥ 350	≥ 520	≥ 35	≥ 47	-

Gas test: Acc. To EN 439: M13(Cargal1)

Shielding Gas: Acc. To EN 439: M13(Cargal1)

Materials

1.4541 (X6CrNiTi18-10); 1.4301 (X4CrNi18-10); 1.4311 (X2CrNi18-10)
AISI 304 - 304L - 302

Storage

Keep dry and avoid condensation

Current condition and welding position

DC+

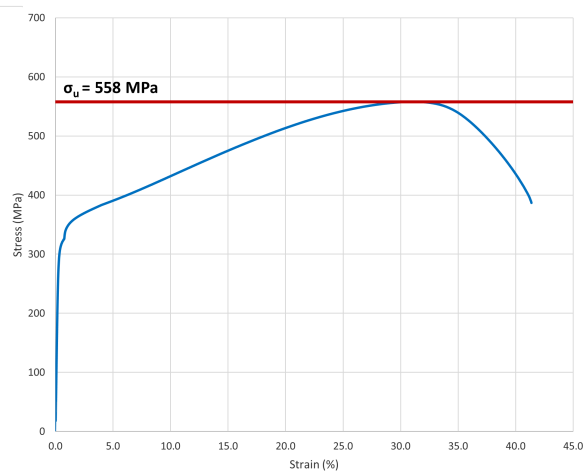
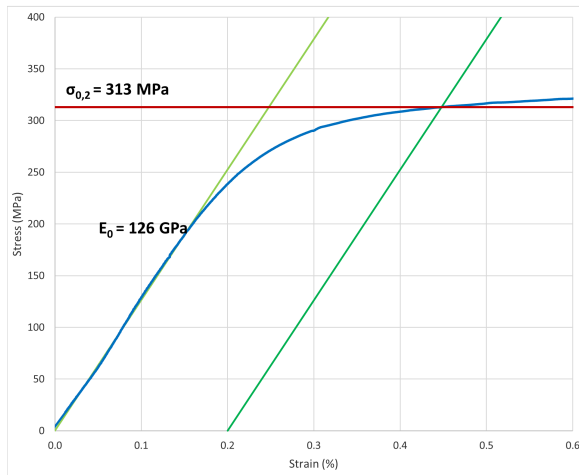


Packaging data: BS300 Kg. 15

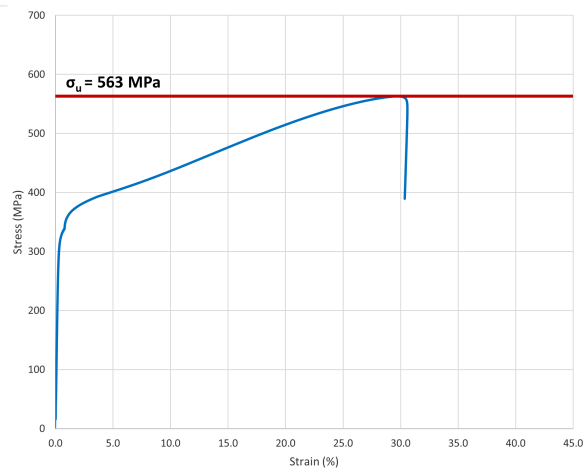
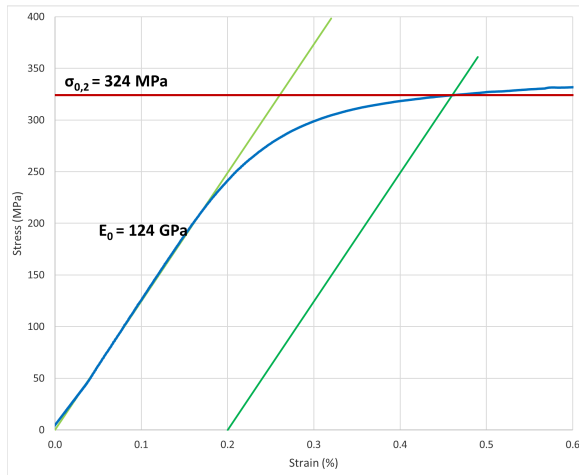
Diameters	0,6	0,8	1,0	1,2	1,6

A.2 Tensile test results in transverse printed direction.

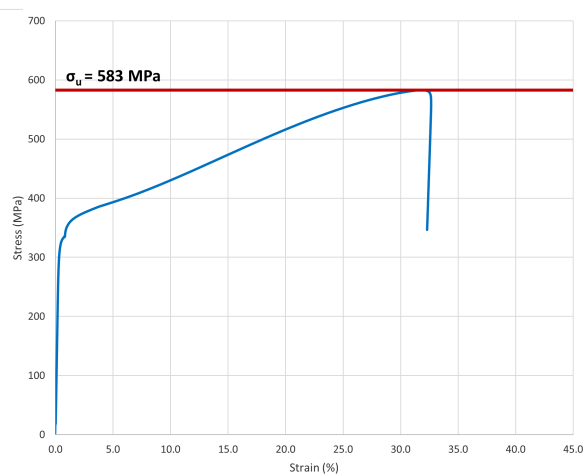
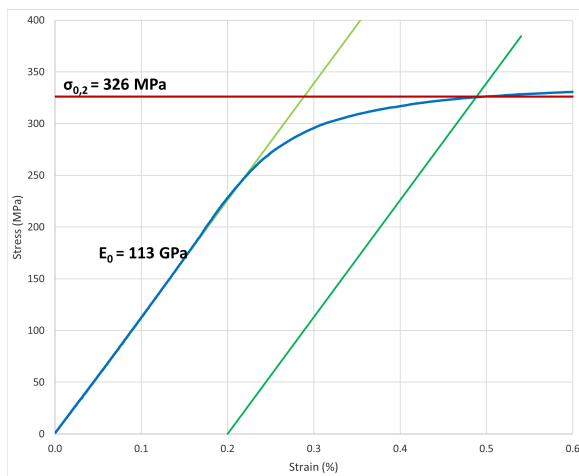
Continuous - Print Direction (Transverse) – Specimen 01



Continuous - Print Direction (Transverse) – Specimen 02

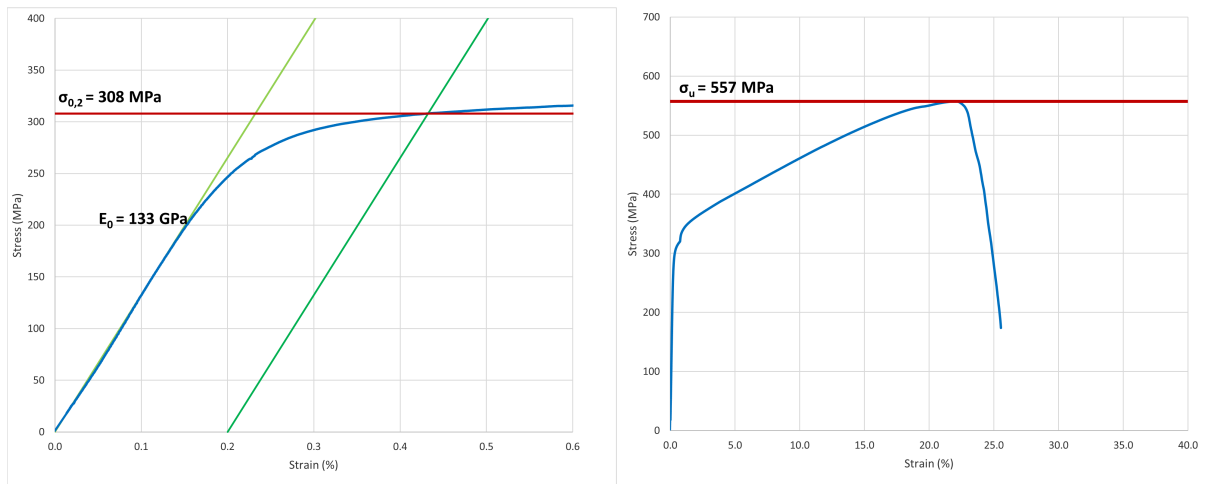


Continuous - Print Direction (Transverse) – Specimen 03

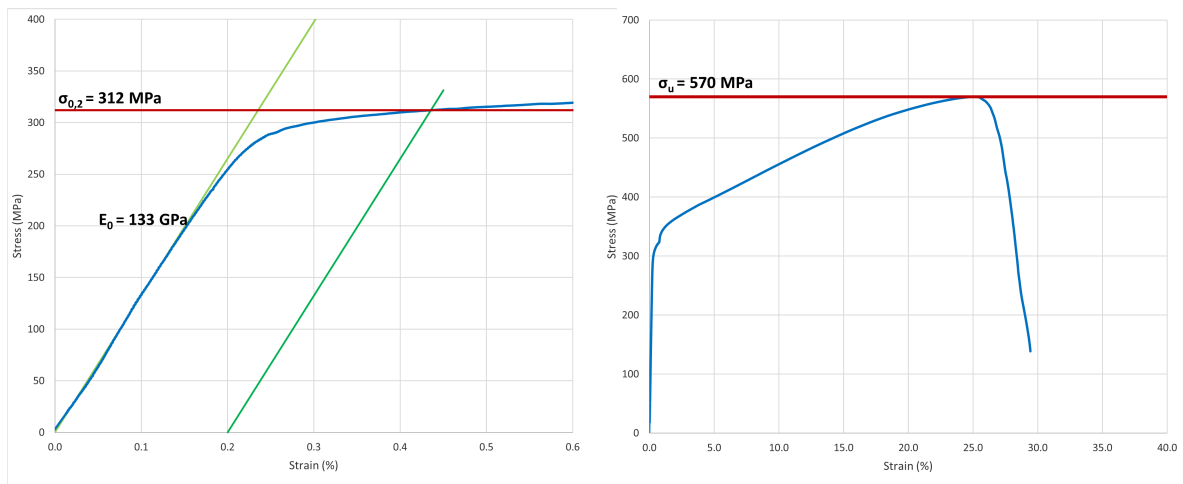


A.3 Tensile test results in longitudinal printed direction.

Continuous - Print Direction (Longitudinal) – Specimen 01



Continuous - Print Direction (Longitudinal) – Specimen 02



Continuous - Print Direction (Longitudinal) – Specimen 03

